CURVATURE EFFECTS ON THE STABILITY OF THREE-DIMENSIONAL LAMINAR BOUNDARY LAYERS

by

Fayette Smith Collier, Jr.

Dissertation submitted to the Faculty of the
Virginia Polytechnic Institute and State University
in partial fulfillment of the requirements for the degree of

DOCTOR OF PHILOSOPHY

in

Aerospace Engineering

APPROVED:

J. A. Schetz, Chairman

S. A. Ragab

A. K. Jakubowski

W. L. Neu

R. D. Wagner

May, 1988

Blacksburg, Virginia

CURVATURE EFFECTS ON THE STABILITY OF THREE-DIMENSIONAL LAMINAR BOUNDARY LAYERS

by

Fayette Smith Collier, Jr.

Committee Chairman: Joseph A. Schetz

Aerospace and Ocean Engineering

(ABSTRACT)

The linear stability equations which govern the growth of small periodic disturbances for compressible, three-dimensional laminar boundary layer flow are derived in an orthogonal curvilinear coordinate system. The parallel flow assumption is utilized in the derivation. The system of equations is solved using a finite difference scheme similar to that in a current state-of-the-art stability analysis code, COSAL. The LR method and the inverse Rayleigh iteration procedure are used to calculate the eigenvalues.

The stability of the three-dimensional compressible laminar boundary layer including the effects of streamline and surface curvature for flows past swept wings where crossflow type disturbances dominate is calculated. A parametric study is performed varying Reynolds number and sweep angle on an airfoil with a concave cutout in the leading edge region of the lower surface. It is known that convex curvature has a stabilizing effect on the laminar boundary layer. Conversely, concave curvature has a destabilizing effect. The magnitude of these effects for swept wing flows is determined. Non-stationary as well as stationary disturbances are calculated, and the most amplified frequencies are identified.

N-factor correlations at the measured location of transition are made utilizing flight test data. Results indicate that amplification rates and hence, N-factors, for swept wing flows over convex surfaces are *reduced* by about 30 to 50 percent when curvature effects are included in the linear stability analysis. In addition, comparisons are made with some experimental results on a swept concave-convex surface. Calculated velocity vector plots show good agreement with observed disturbances in the laminar boundary layer over the concave surface. The results of the calculations show that concave curvature *destabilizes* "crossflow" type disturbances with a 30 percent *increase* in amplification rate.

ACKNOWLEDGEMENTS

The author would like to sincerely thank Dr. Joe Schetz for his unending support, guidance and patience throughout the pursuit of advanced studies at Virginia Tech as well as throughout the duration of this work. Likewise, thanks and appreciation are extended to faculty and staff members of the AOE department who in one way or another assisted in the achievement of this goal. Special thanks to Drs. Jakubowski and Neu of the AOE Department and Dr. Ragab of the ESM Department for serving on the committee and providing many useful comments and suggestions.

In addition, sincere thanks goes to , Head of the Laminar Flow Control Project Office of NASA Langley Research Center, who served on the committee, and his capable staff for their support, comments, and encouragement during this work. Thanks also to of High Technology Corporation who provided much technical guidance during the course of this work.

Finally, thanks and appreciation are extended to my family and friends; and especially to my wife,

TABLE OF CONTENTS

LIST OF TABLES

LIST OF FIGURES

LIST OF FIGURES-Continued

LIST OF FIGURES-Continued

LIST OF SYMBOLS

A	disturbance amplitude
a	radius of curvature of wing surface
C	streamwise chord length of wing
C_p	constant pressure specific heat and pressure coefficient, $(p - p_\infty)/q_\infty$
C_q	suction coefficient, $(\rho W)_w / (\rho U)_e$
e_{ij}	rate of strain tensor components
f	disturbance frequency, Hertz
G_L	Görtler number, $R_L (\lvert\bar{\kappa}\rvert)^{1/2}$
$g_{1,2}$	metric coefficients for the x, y, z system of axes
$h_{1,2}$	metric coefficients for the ξ, η, z system of axes
H	static enthalpy
k	laminar thermal conductivity
L	characteristic length, $(\nu_e S/U_e)^{1/2}$
L/D	lift to drag ratio
M	Mach number
N	$\ln(A/A_0)$
p	static pressure
Pr	Prandtl number, $\mu C_p/k$
q_i	component of heat flux vector, q
r	radial coordinate in the cylindrical polar system r, θ, ζ
R	reference Reynolds number, $U_e \delta^* / \nu_e$
R_C	freestream Reynolds number, $U_\infty C / \nu_\infty$
R_{cf}	crossflow Reynolds number, $\chi_{max} \Delta_{0.01} / \nu_e$
R_L	Reynolds number based on L, $U_e L / \nu_e$
$\bar{R}$	gas constant
$\Re$	real component

S	surface distance along streamline path
s, c, w	velocity components inside the boundary layer in the ξ, η, z directions
t	time
T	temperature
T/C	normalized airfoil coordinate
U	total flow velocity, $(u^2 + v^2)^{1/2}$
u, v, w	velocity components inside the boundary layer in the x, y, z directions
X/C	normalized streamwise direction
x, y, z	set of fixed reference axes

Greek

α, β	real disturbance wave number in the ξ and η directions, respectively
$\delta_{0.995}$	streamwise boundary layer thickness
δ^*	displacement thickness in the x direction
ϵ	angle between x and ξ coordinate directions
η	coordinate direction in the wave aligned ξ, η, z system
θ	azimuthal coordinate in the cylindrical polar system r, θ, ς
Λ	infinite wing leading edge sweep angle
λ	second laminar coefficient of viscosity
λ_w	wavelength of the disturbance
μ	first laminar coefficient of viscosity
ν	laminar kinematic viscosity
γ	ratio of specific heats
ξ	coordinate direction in the wave aligned ξ, η, z system
ϕ	angle between the wavenumber vector and ξ direction
ψ	angle between the external streamline direction and the x direction
ω	complex disturbance frequency
ρ	density

ς axial component in the cylindrical polar coordinate system r, θ, ς

κ bulk viscosity coefficient where $\kappa = \lambda + 2\mu/3$

$\bar{\kappa}$ local surface curvature along inviscid streamline path normalized with L

σ spatial amplification rate

τ_i stress tensor component

φ disturbance orientation angle with respect to streamline direction

χ_{max} maximum mean crossflow velocity

$\Delta_{0.01}$ distance normal to surface at $\chi = 0.01\chi_{max}$

Subscripts

0 initial

e at the edge of the boundary layer

i imaginary part of a complex number

n normal to airfoil leading edge

r real part of a complex number

tr transition

w at the wall

∞ in the undisturbed freestream

Superscripts

($\bar{}$) mean (time averaged) quantity

($\tilde{}$) fluctuating quantity

($\hat{}$) disturbance amplitude function

( )′ differentiated with respect to *z*

Chapter 1

INTRODUCTION

The interest in the possible application of laminar flow control (LFC) techniques to commercial transports has dramatically increased in the past ten years in both the United States and abroad. Referring to Table 1, which compares an advanced turbulent commercial aircraft to an aircraft with LFC incorporated in the design, a yearly savings of 4 million dollars in fuel costs for that particular mission could be realized (see Ref. 1) . The LFC systems costs could be recovered in the first six months of operation. It must be noted that these savings are based on fuel costs of $1.50 per gallon, but with the dubious forecast of decreasing worldwide petroleum supplies these kinds of fuel costs will most certainly return. More recently, studies are being conducted to determine the feasibility of a new supersonic transport effort in the U. S. . As seen in Figure 1, a possible 20 % increase in L/D at transition Reynolds numbers on the order of 100 million is possible if laminar flow can be achieved on part of the highly swept lifting surfaces.

To predict potential savings in fuel costs or improvements in aerodynamic efficiency as a function of total laminarized surface area, one must be able to accurately predict the location of transition on complex three-dimensional geometries. Pressure gradient, surface curvature, wall temperature, mass transfer and unit Reynolds number are known to influence the stability of the boundary layer. To further complicate matters, there exist many environmental disturbances any one of which can cause immediate transition to turbulent flow if "supercritical" in nature (see Table 2). For example, insect strikes near the leading edge can trip the boundary layer causing premature transition. Under such conditions, stability theory is not applicable (Ref. 2). Assuming one can avoid the problems associated with the list from Table 2, stability theory can be a useful tool to predict the onset of transition.

However, it is considered to be only about 20 % accurate. The major goal of this work is to extend the current linear stability theory to include the effects of surface curvature and streamline curvature for compressible flows past swept wings. It is hoped that the extended theory will better correlate swept wing transition data.

In the following sections, a brief historical perspective is given concerning the advancement of the science of laminar flow control. Tied closely to the problems associated with the achievement of laminar flow in flight and in wind tunnel investigations is the development of boundary layer stability theory and transition prediction techniques. An understanding of the former is required to properly utilize the latter.

1.1 Historical Review of Laminar Flow Investigations

Historically speaking, the idea of applying laminar flow control techniques to aircraft to achieve better aerodynamic efficiency is not a new one. On the subject, including both flight and ground tests, there exists an extensive survey and bibliography of the efforts conducted up to about 1978 (Ref. 3) . Also, there exists an annotated bibliography which emphasizes the aerodynamics, systems, and structures studies stimulated by NASA's Aircraft Energy Efficiency Laminar Flow Control Program covering the years between 1976 to 1982 (Ref. 4). A more recent treatment which reviews historical and present day efforts aimed at achieving laminar flow is given by Wagner, et. al. (Ref. 5).

When designing an airfoil for laminar flow applications on swept wings, the engineer must be concerned about the growth of various disturbances in the boundary layer which can be responsible for transition from laminar to turbulent flow. There are four types of primary interest which must be considered:

1. streamwise instability (T-S)
2. attachment line contamination
3. crossflow instability
4. centrifugal instability (Görtler)

Although the thrust of this work will involve investigating curvature effects on the centrifugal and crossflow instabilities, a brief description of the streamwise instability and attachment line contamination is given . The possible interaction of the primary instabilities and the problem of secondary instabilities will not be addressed.

The stability of laminar flow and the process of laminar to turbulent transition was first investigated in the classical dye experiments performed by Reynolds (Ref. 6). Reynolds, and a little later, Lord Rayleigh, put forth the basis of present day stability theory in efforts aimed at determining whether the disturbances in a particular flow (inviscid) amplify or decay with time (see Refs. 7-8). Some fifty years later, in the late 20's and early 30's, the work of Tollmien (Refs. 9-10) and Schlichting (Refs. 11-12) resulted in a firm understanding of the viscous boundary layer stability theory. The theory was given credibility when the results of the classical experiments of Schubauer and Skramstead (Ref. 13) verified most of the predictions of the two-dimensional theory. Excellent reviews of this type of instability are given by Mack (Ref. 14) and Schlichting (Ref. 15). The difference in the viscous instability for flows past swept wings is the influence of crossflow velocity profile due to the wing sweep. Although it will not be addressed here, it is not known what effect, if any, surface and streamline curvature will have on the streamwise instability for flows past swept wings.

The problem of attachment line contamination concerns the spanwise propagation of turbulence along the leading edge of a swept wing. Such disturbances may originate from the fuselage or large roughness elements on the leading edge and may cause turbulent flow over the whole wing surface, dashing the hope of achieving any laminar flow. This type of instability was first observed by Gray in the transition flight experiments of the AW52 (see Ref. 16). He noticed that above certain flight speeds, transition moved quickly to the leading edge. The

phenomena seemed to be a function of leading edge radius as well as sweep. Immediately following the flight test, wind tunnel investigations were conducted which confirmed Gray's observations (Ref.17 and 18). However, the significance of the problem was not realized until it was "rediscovered" by the Northrop Boundary Layer Group during the X-21 flight test program (Ref. 19). The X-21 was designed to achieve full chord laminar flow at cruise conditions utilizing boundary layer suction through slots. However, in the early tests, transition occurred right at the leading edge. A similar flight test on the Lancaster bomber in Great Britain was plagued by the same problem (Ref. 20). A series of wind tunnel investigations (Refs. 21-24) were started to examine in detail the transition mechanism . The results showed that to avoid leading edge contamination one must keep the momentum thickness Reynolds number at the attachment line below 100. It was shown that reducing the sweep, the leading edge radius, and the unit Reynolds numbers have favorable effects on the problem. This is a design criteria which is still utilized by the aircraft industry today. It was also shown that leading edge devices such as the Gaster bump and suction along the attachment line could be utilized to control the problem. See Refs. 25-26 for an excellent treatment of this subject.

The crossflow instability for flows past swept wings is known to occur in regions of large streamwise pressure gradient (positive or negative). In the leading edge region where both the surface curvature and the pressure gradient are large, the streamlines are deflected due to spanwise pressure gradients. The slower moving fluid near the wall is deflected even more resulting in the development of a crossflow velocity profile in the boundary layer that is perpendicular to the streamline direction. As seen in Figure 2, the crossflow profile is inflectional in nature and is known to be dynamically unstable. At some point in the flow as the Reynolds number is increased, the highly unstable profiles cause the generation of crossflow

vortices. These disturbances are co-rotating and are aligned with their axes skewed approximately 4-6 degrees with the streamline (Ref. 27).

In flight, the existence of this instability was first observed by Gray (Ref. 16). It was noted that transition occurred at flight Reynolds numbers lower than those for unswept wings. Using a flow visualization technique, streamwise striations with fixed spacing were observed in the leading edge region of the wing prior to transition. Wind tunnel tests conducted immediately after the flight tests confirmed the observations made in flight (Ref. 17). Owen and Randall (and independently, H.B. Squire) correctly identified the disturbances as crossflow vortices by properly considering the influence of the crossflow boundary layer profiles in the analysis (see Ref. 27).

The crossflow instability for the flow past swept wings is fundamentally the same as that for the flow past a rotating disk. The rotating disk flow is easier to analyze and provides much information about the crossflow instability. The linear stability equations which describe the stability of the boundary layer for this class of problems was first derived by Stuart (see Ref. 28). Later, it was shown that the streamline curvature and Coriolis terms included in the analysis stabilized the boundary layer significantly (Ref. 29). This idea was extended to the flow past a swept cylinder. There again, the influence of the streamline and surface curvature terms were shown to be very stabilizing for flows over convex surfaces (Ref. 30). In all previous studies with curvature included in the analysis, the incompressible flow equations were derived. As mentioned earlier, a major objective of this work is to extend the incompressible analysis of Ref. 30 to the compressible equations of motion for the flow past swept wings.

The situation in two dimensions for flows past concave surfaces where centrifugal effects are important has been studied extensively starting with the the works of Taylor (Ref. 31) and Görtler (Ref. 32 and 33). Here, it was shown that pairs of counter-rotating vortices formed in the boundary layer for flows past

concave walls exceeding a certain Reynolds number. In the concave region such as that found on the lower surface of supercritical airfoils, it is not known whether the Taylor-Görtler (TG) type disturbances are important at the sweep angles of interest or what effect, if any, concave curvature has on the crossflow instability. Recently, Hall (Ref. 34) studied the problem of the Taylor-Görtler vortex structure in three-dimensional boundary layers using asymptotic theory. He showed that the Görtler vortex structure cannot be sustained in a three dimensional boundary layer with large enough crossflow Reynolds number.

Up to this point in time, there have been no experimental studies for conditions such as those that may occur in flight to determine the state of the boundary layer in the concave region of supercritical airfoil for non-zero sweep angles. One experiment has been conducted by Kohama (Ref. 35) in which the laminar boundary layer on a concave-convex surface was studied using flow visualization and hot-wire anemometer techniques. However, the pressure distribution through the concave region was modified by tailoring the test section walls. The result was a nearly constant pressure distribution in the concave region which, in effect, delayed transition to a location aft of the concave region. At a sweep angle of 47 degrees, Kohama observed that it was the Görtler vortex type disturbance formed in the concave region which caused the onset of transition. One of the objectives of this study is to analyze the stability of the boundary layer for this type of flow utilizing the incompressible stability theory as given in Refs. 30 and 36.

1.2 Transition Prediction Utilizing the e^N Method

The current state-of-the-art method for predicting the onset of transition for laminar boundary layers is the e^N method first proposed independently by Smith and Gamberoni (Ref. 37) and Van Ingen (Ref. 38) . Simply put, this semi-empirical method involves computing the stability of the boundary layer in terms of the disturbance amplification rate which is then integrated to yield the N-factor.

The key to the method is the hope that at the transition location the N-factor will be a single universal value. A simplified schematic of the processes associated with transition for low background disturbance environment is given in Figure 3. The e^N method of transition prediction seems to work well because of the fact that the linear region in the breakdown process occurs over a relatively long distance compared to the nonlinear region (see Ref. 2). For two-dimensional boundary layers where Tollmien-Schlichting disturbances dominate the transition process, Smith showed the calculated N-factor to be near 9 at the measured transition location for low speed test conditions.

However, the situation is a bit clouded for flows of a three-dimensional nature such as those past swept wings where crossflow disturbances are present and are strongly amplified. Previous studies have shown that for flows where transition is caused by the growth of crossflow disturbances the calculated N-factor at transition varies in a range of about 7-11 (Ref. 2). Some analysis of recent flight transition data on swept wings have produced N-factors as high as 20 (Ref. 39). Up to this point in time, the linear stability theory utilized in the correlations of swept wing data neglected the effects of surface and streamline curvature (Refs. 40 -45). Also, it is commonly thought that only stationary crossflow disturbances need to be calculated and included in the transition prediction process. However, it was shown by Malik and Poll (Ref. 30) that stability calculations including the surface and streamline curvature terms in the equations resulted in significant stabilization of the boundary layer for the flow past a swept cylinder. In addition, it was shown that travelling crossflow type disturbances were most amplified.

From an engineering point of view, the results from Ref. 30 have important implications if one must design a suction system for a hybrid laminar flow wing or estimate the fuel consumption of a new design utilizing LFC . Because of the conservative results from the current analysis tool (curvature neglected), one might design for too much suction or too much fuel resulting in higher costs and

more weight. Therefore, it is important to fully understand the magnitude of the curvature effects on laminar boundary layer stability.

1.3 Objectives of the Present Study

The linear stability equations which govern the growth of small periodic disturbances for compressible, three-dimensional laminar boundary layer flow are to be derived in an orthogonal curvilinear coordinate system. The parallel flow assumption is to be utilized in the derivation. The system of equations is to be solved using a finite difference scheme similar to that in a current state-of-the-art stability analysis code, COSAL, which utilizes fully pivoted LU factorization. The inverse Rayleigh iteration procedure is to be used to calculate the eigenvalue.

The stability of the three-dimensional compressible laminar boundary layer including the effects of streamline and surface curvature for flows past swept wings where crossflow type disturbances dominate is to be calculated. A parametric study is then to be performed varying Reynolds number and sweep angle on an airfoil with a concave cutout in the leading edge region of the lower surface. It is known that convex curvature has a stabilizing effect on the stability of the laminar boundary layer. Conversely, concave curvature has a destabilizing effect. The magnitude of these effects for swept wing flows is to be determined. Nonstationary as well as stationary disturbances are to be calculated and the most amplified frequencies are identified. Lastly, N-factor correlations at the measured location of transition are to be made utilizing flight test data.

Chapter 2

ANALYSIS

2.1 Governing Equations for Compressible Flow

The conservation equations for a viscous, heat conducting, perfect gas written in vector notation as the continuity and momentum equations, respectively, can be written as;

$$\frac{\partial \rho}{\partial t} + \nabla \cdot (\rho \mathbf{V}) = 0 \tag{2.1a}$$

$$\rho \left[\frac{\partial \mathbf{V}}{\partial t} + (\mathbf{V} \cdot \nabla)\mathbf{V} \right] = -\nabla p + \mathbf{F} + (\nabla \cdot \tau) \tag{2.1b}$$

and the energy equation in terms of the temperature can be written in vector form as;

$$\rho C_p \left[\frac{\partial T}{\partial t} + (\mathbf{V} \cdot \nabla)T \right] - \left[\frac{\partial p}{\partial t} + (\mathbf{V} \cdot \nabla)p \right] = -\nabla \cdot \mathbf{q} + \tau : (\nabla \mathbf{V}) + W \tag{2.1c}$$

The state equation is written as

$$p = \rho \bar{R} T \tag{2.1d}$$

Here, the usual notation is used; $\mathbf{V}$, is the velocity vector; $\mathbf{q}$, the heat-flux vector; $\mathbf{F}$, the body force per unit volume; W, the heat generation per unit volume; τ, the viscous stress tensor; and ρ, p, T, t the density, the pressure, the temperature, and the time, respectively. C_p is the specific heat at constant pressure and is assumed to be constant and $\bar{R}$ is the gas constant.

It is proposed to follow the method employed by Ref. 30 to analyze the three-dimensional flow past a curved surface. Two orthogonal curvilinear coordinates systems, one fixed (x, y, and z) relative to the body and the other (ξ, η, and z)

free to rotate relative to x, y, and z are utilized and are shown in Figure 4. The angle between x and ξ is defined as ϵ. In the reference system, x and y lie in the plane of the body and z is normal to the surface. The corresponding velocity components are u, v and w. Elements of length for curved surfaces in this system are given by $g_1 dx$, $g_2 dy$, and $g_3 dz$. Therefore, the differential arclength, $d\ell$ is,

$$d\ell^2 = {g_1}^2 (dx)^2 + {g_2}^2 (dy)^2 + {g_3}^2 (dz)^2$$

Likewise, in the ξ, η and z system, ξ and η lie in the plane of the surface and z is normal to the surface. The differential arclength is given by

$$d\ell^2 = {h_1}^2 (d\xi)^2 + {h_2}^2 (d\eta)^2 + {h_3}^2 (dz)^2$$

The velocity components are s, c and w. This system is used for the stability analysis. Then the continuity equation is

$$\frac{\partial \rho}{\partial t} + \frac{1}{h_1 h_2 h_3}\left[\frac{\partial}{\partial \xi}(h_2 h_3 \rho s) + \frac{\partial}{\partial \eta}(h_1 h_3 \rho c) + \frac{\partial}{\partial z}(h_1 h_2 \rho w)\right] = 0$$

The components of the momentum equation in the ξ, η and z directions is

$$\xi: \quad \frac{\partial s}{\partial t} + \frac{s}{h_1}\frac{\partial s}{\partial \xi} + \frac{c}{h_2}\frac{\partial s}{\partial \eta} + \frac{w}{h_3}\frac{\partial s}{\partial z} + \frac{sc}{h_1 h_2}\frac{\partial h_1}{\partial \eta} + \frac{sw}{h_1 h_3}\frac{\partial h_1}{\partial z} - \frac{c^2}{h_1 h_2}\frac{\partial h_2}{\partial \xi} - \frac{w^2}{h_1 h_3}\frac{\partial h_3}{\partial \xi} = -\frac{1}{\rho}\frac{1}{h_1}\frac{\partial p}{\partial \xi} + \frac{F_\xi}{\rho} + \frac{1}{\rho}(\nabla \cdot \tau)_\xi$$

$$\eta: \quad \frac{\partial c}{\partial t} + \frac{s}{h_1}\frac{\partial c}{\partial \xi} + \frac{c}{h_2}\frac{\partial c}{\partial \eta} + \frac{w}{h_3}\frac{\partial c}{\partial z} + \frac{cs}{h_1 h_2}\frac{\partial h_2}{\partial \xi} + \frac{cw}{h_1 h_3}\frac{\partial h_2}{\partial z} - \frac{s^2}{h_1 h_2}\frac{\partial h_1}{\partial \eta} - \frac{w^2}{h_2 h_3}\frac{\partial h_3}{\partial \eta} = -\frac{1}{\rho}\frac{1}{h_2}\frac{\partial p}{\partial \eta} + \frac{F_\eta}{\rho} + \frac{1}{\rho}(\nabla \cdot \tau)_\eta$$

$$z: \quad \frac{\partial w}{\partial t} + \frac{s}{h_1}\frac{\partial w}{\partial \xi} + \frac{c}{h_2}\frac{\partial w}{\partial \eta} + \frac{w}{h_3}\frac{\partial w}{\partial z} + \frac{ws}{h_1 h_3}\frac{\partial h_3}{\partial \xi} + \frac{wc}{h_2 h_3}\frac{\partial h_3}{\partial \eta} - \frac{s^2}{h_1 h_3}\frac{\partial h_1}{\partial z} - \frac{c^2}{h_2 h_3}\frac{\partial h_2}{\partial z} = -\frac{1}{\rho}\frac{1}{h_3}\frac{\partial p}{\partial z} + \frac{F_z}{\rho} + \frac{1}{\rho}(\nabla \cdot \tau)_z$$

The components of the divergence of the stress tensor τ are given by

$$(\nabla \cdot \tau)_\xi = \frac{1}{h_1 h_2 h_3}\left[\frac{\partial}{\partial \xi}(h_2 h_3 \tau_{\xi\xi}) + \frac{\partial}{\partial \eta}(h_1 h_3 \tau_{\xi\eta}) + \frac{\partial}{\partial z}(h_1 h_2 \tau_{\xi z})\right]$$

$$+\tau_{\xi\eta}\frac{1}{h_1 h_2}\frac{\partial h_1}{\partial \eta} + \tau_{\xi z}\frac{1}{h_1 h_3}\frac{\partial h_1}{\partial z} - \tau_{\eta\eta}\frac{1}{h_1 h_2}\frac{\partial h_2}{\partial \xi} - \tau_{zz}\frac{1}{h_1 h_3}\frac{\partial h_3}{\partial \xi}$$

$$(\nabla \cdot \tau)_\eta = \frac{1}{h_1 h_2 h_3}\left[\frac{\partial}{\partial \xi}(h_2 h_3 \tau_{\xi\eta}) + \frac{\partial}{\partial \eta}(h_1 h_3 \tau_{\eta\eta}) + \frac{\partial}{\partial z}(h_1 h_2 \tau_{\eta z})\right]$$

$$+\tau_{\xi\eta}\frac{1}{h_1 h_2}\frac{\partial h_2}{\partial \xi} + \tau_{\eta z}\frac{1}{h_2 h_3}\frac{\partial h_2}{\partial z} - \tau_{\xi\xi}\frac{1}{h_1 h_2}\frac{\partial h_1}{\partial \eta} - \tau_{zz}\frac{1}{h_2 h_3}\frac{\partial h_3}{\partial \eta}$$

$$(\nabla \cdot \tau)_z = \frac{1}{h_1 h_2 h_3}\left[\frac{\partial}{\partial \xi}(h_2 h_3 \tau_{z\xi}) + \frac{\partial}{\partial \eta}(h_1 h_3 \tau_{\eta z}) + \frac{\partial}{\partial z}(h_1 h_2 \tau_{zz})\right]$$

$$+\tau_{z\xi}\frac{1}{h_1 h_3}\frac{\partial h_3}{\partial \xi} + \tau_{\eta z}\frac{1}{h_2 h_3}\frac{\partial h_3}{\partial \eta} - \tau_{\xi\xi}\frac{1}{h_1 h_3}\frac{\partial h_1}{\partial z} - \tau_{\eta\eta}\frac{1}{h_2 h_3}\frac{\partial h_2}{\partial z}$$

The relationship between the components of the stress tensor and the rate of strain tensor for a Stokes' fluid is given by

$$\tau_{\xi\xi} = \lambda \nabla \cdot \mathbf{V} + \mu e_{\xi\xi}$$

$$\tau_{\eta\eta} = \lambda \nabla \cdot \mathbf{V} + \mu e_{\eta\eta}$$

$$\tau_{zz} = \lambda \nabla \cdot \mathbf{V} + \mu e_{zz}$$

$$\tau_{\xi\eta} = \tau_{\eta\xi} = \mu e_{\xi\eta}$$

$$\tau_{\xi z} = \tau_{z\xi} = \mu e_{\xi z}$$

$$\tau_{\eta z} = \tau_{z\eta} = \mu e_{\eta z}$$

where the divergence of the velocity vector is given by

$$\nabla \cdot \mathbf{V} = \frac{1}{h_1 h_2 h_3}\left[\frac{\partial}{\partial \xi}(h_2 h_3 s) + \frac{\partial}{\partial \eta}(h_1 h_3 c) + \frac{\partial}{\partial z}(h_1 h_2 w)\right]$$

and the components of the rate of strain tensor are given by

$$e_{\xi\xi} = 2\left(\frac{1}{h_1}\frac{\partial s}{\partial \xi} + \frac{c}{h_1 h_2}\frac{\partial h_1}{\partial \eta} + \frac{w}{h_3 h_1}\frac{\partial h_1}{\partial z}\right)$$

$$e_{\eta\eta} = 2\left(\frac{1}{h_2}\frac{\partial c}{\partial \eta} + \frac{w}{h_2 h_3}\frac{\partial h_2}{\partial z} + \frac{s}{h_1 h_2}\frac{\partial h_2}{\partial \xi}\right)$$

$$e_{zz} = 2\left(\frac{1}{h_3}\frac{\partial w}{\partial z} + \frac{s}{h_1 h_3}\frac{\partial h_3}{\partial \xi} + \frac{c}{h_2 h_3}\frac{\partial h_3}{\partial \eta}\right)$$

$$e_{\xi\eta} = \frac{h_2}{h_1}\frac{\partial}{\partial \xi}\left(\frac{c}{h_2}\right) + \frac{h_1}{h_2}\frac{\partial}{\partial \eta}\left(\frac{s}{h_1}\right)$$

$$e_{\xi z} = \frac{h_1}{h_3}\frac{\partial}{\partial z}\left(\frac{s}{h_1}\right) + \frac{h_3}{h_1}\frac{\partial}{\partial \xi}\left(\frac{w}{h_3}\right)$$

$$e_{\eta z} = \frac{h_3}{h_2}\frac{\partial}{\partial \eta}\left(\frac{w}{h_3}\right) + \frac{h_2}{h_3}\frac{\partial}{\partial z}\left(\frac{c}{h_2}\right)$$

The relationship between the first and second coefficients of viscosity is

$$\lambda = \kappa - \frac{2}{3}\mu$$

where κ is the bulk viscosity coefficient. In general, the convection of a scalar quantity f, such as T or p, can be written as

$$(\mathbf{V} \cdot \nabla) f = s\frac{1}{h_1}\frac{\partial f}{\partial \xi} + c\frac{1}{h_2}\frac{\partial f}{\partial \eta} + w\frac{1}{h_3}\frac{\partial f}{\partial z}$$

The divergence of the heat flux vector $\mathbf{q}$ in the energy equation is

$$\nabla \cdot \mathbf{q} = \frac{1}{h_1 h_2 h_3}\left[\frac{\partial}{\partial \xi}(h_2 h_3 q_\xi) + \frac{\partial}{\partial \eta}(h_1 h_3 q_\eta) + \frac{\partial}{\partial z}(h_1 h_2 q_z)\right]$$

where the components of the heat flux are given by Fourier's heat conduction law, that is,

$$q_\xi = -k\frac{1}{h_1}\frac{\partial T}{\partial \xi}$$

$$q_\eta = -k\frac{1}{h_2}\frac{\partial T}{\partial \eta}$$

$$q_z = -k\frac{1}{h_3}\frac{\partial T}{\partial z}$$

Finally, the rate of dissipation of energy is

$$\begin{aligned}
\tau : (\nabla \mathbf{V}) =& \tau_{\xi\xi}\left[\frac{1}{h_1}\frac{\partial s}{\partial \xi} + \frac{c}{h_1 h_2}\frac{\partial h_1}{\partial \eta} + \frac{w}{h_3 h_1}\frac{\partial h_1}{\partial z}\right] \\
&+\tau_{\eta\eta}\left[\frac{1}{h_2}\frac{\partial c}{\partial \eta} + \frac{w}{h_2 h_3}\frac{\partial h_2}{\partial z} + \frac{s}{h_1 h_2}\frac{\partial h_2}{\partial \xi}\right] \\
&+\tau_{zz}\left[\frac{1}{h_3}\frac{\partial w}{\partial z} + \frac{s}{h_1 h_3}\frac{\partial h_3}{\partial \xi} + \frac{c}{h_2 h_3}\frac{\partial h_3}{\partial \eta}\right] \\
&+\tau_{\xi\eta}\left[\frac{h_2}{h_1}\frac{\partial}{\partial \xi}\left(\frac{c}{h_2}\right) + \frac{h_1}{h_2}\frac{\partial}{\partial \eta}\left(\frac{s}{h_1}\right)\right] \\
&+\tau_{\xi z}\left[\frac{h_1}{h_3}\frac{\partial}{\partial z}\left(\frac{s}{h_1}\right) + \frac{h_3}{h_1}\frac{\partial}{\partial \xi}\left(\frac{w}{h_3}\right)\right] \\
&+\tau_{\eta z}\left[\frac{h_3}{h_2}\frac{\partial}{\partial \eta}\left(\frac{w}{h_3}\right) + \frac{h_2}{h_3}\frac{\partial}{\partial z}\left(\frac{c}{h_2}\right)\right]
\end{aligned}$$

2.2 Non-dimensionalization of the Governing Equations

Neglecting body forces and the work done by the system, the equations written above along with the equation of state results in set of six equations for the six unknowns s, c, w, T, p, and ρ. The laminar coefficient of viscosity, μ, as well as the second viscosity coefficient, λ, and the coefficient of thermal conductivity are

assumed to be functions of temperature only. Sutherlands law is utilized to calculate the laminar viscosity coefficient. For this study, the bulk viscosity coefficient is taken as zero and $\lambda = -2\mu/3$; however, these simplifications are not made in the derivation given below. The equations are made dimensionless by normalizing the velocity components s, c, and w with the edge velocity, U_e; the pressure with $\rho_e {U_e}^2$; the temperature with T_e; and the density with ρ_e. The viscosity coefficients are referred to μ_e. The coordinates ξ, η, and z are normalized with the boundary layer displacement thickness in the x direction, δ^*. The resulting non-dimensional form of the governing equations are

$$\frac{\partial \rho}{\partial t} + \nabla \cdot (\rho \mathbf{V}) = 0 \tag{2.2a}$$

$$\rho \left[\frac{\partial \mathbf{V}}{\partial t} + (\mathbf{V} \cdot \nabla)\mathbf{V} \right] = -\nabla p + \frac{1}{R}(\nabla \cdot \tau) \tag{2.2b}$$

$$\rho \left[\frac{\partial T}{\partial t} + (\mathbf{V} \cdot \nabla)T \right] - (\gamma - 1){M_e}^2 \left[\frac{\partial p}{\partial t} + (\mathbf{V} \cdot \nabla)p \right] = -\frac{1}{R}\nabla \cdot \mathbf{q} + \frac{(\gamma - 1){M_e}^2}{R} \tau : (\nabla \mathbf{V}) \tag{2.2c}$$

$$p = \frac{\rho T}{\gamma {M_e}^2} \tag{2.2d}$$

where γ is the ratio of specific heats, $M_e = U_e/(\gamma \bar{R} T_e)^{\frac{1}{2}}$, the Mach number and $R = \rho_e U_e \delta^* / \mu_e$ the Reynolds number. The terms in the various components such as $\nabla \cdot \mathbf{q}$ and $\tau : (\nabla \mathbf{V})$ of the non-dimensional equations appear exactly the same as before; therefore, they will not be re-written here.

2.3 The Linear, Compressible Equations for Parallel Flow

Consider a flow where the motion may be described by the superposition of a steady mean component and a small fluctuating component. Here, "small" is taken such that the quadratic terms in the fluctuating parts may be neglected in comparison to the linear terms. Let the mean flow be described by velocity components $\bar{s}$, $\bar{c}$, and $\bar{w}$ with pressure and temperature $\bar{p}$ and $\bar{T}$. The corresponding quantities for the small unsteady disturbance are $\tilde{s}$, $\tilde{c}$, $\tilde{w}$, $\tilde{p}$ and $\tilde{T}$. Also, assume that the physical properties, μ, λ, and k have a steady mean component ($\bar{\mu}$, $\bar{\lambda}$, and $\bar{k}$) and a small fluctuating component ($\tilde{\mu}$, $\tilde{\lambda}$, and $\tilde{k}$) both of which are a function of temperature only. Then, the resultant motion may be described by

$$s = \bar{s} + \tilde{s} \qquad c = \bar{c} + \tilde{c} \qquad w = \bar{w} + \tilde{w}$$

$$T = \bar{T} + \tilde{T} \qquad p = \bar{p} + \tilde{p}$$

with physical properties

$$\mu = \bar{\mu} + \tilde{\mu} \qquad \lambda = \bar{\lambda} + \tilde{\lambda} \qquad k = \bar{k} + \tilde{k}$$

where,

$$\tilde{\mu} = \frac{\partial \bar{\mu}}{\partial \bar{T}} \tilde{T} \qquad \tilde{\lambda} = \frac{\partial \bar{\lambda}}{\partial \bar{T}} \tilde{T} \qquad \tilde{k} = \frac{\partial \bar{k}}{\partial \bar{T}} \tilde{T}$$

All quantities have been made non-dimensional in the same way as the quantities in the previous section. Finally, the assumption of quasi-parallel flow is made, so that the mean flow may be described by;

$$\bar{s} = \bar{s}(z) \quad \bar{c} = \bar{c}(z) \qquad \bar{w} = 0$$

and

$$\bar{p} = \bar{p}(\xi, \eta) \quad \text{and} \quad \bar{T} = \bar{T}(z)$$

and that the mean flow, including these assumptions, satisfies the Navier-Stokes (NS) equations derived above.

After substituting the expressions for the resultant motion given above into the NS equations and subtracting out the mean flow, the continuity, momentum, and energy equations are written as;

continuity:

$$\frac{\partial \tilde{\rho}}{\partial t} + \bar{\rho}\left(\frac{1}{h_1}\frac{\partial \tilde{s}}{\partial \xi} + \frac{1}{h_2}\frac{\partial \tilde{c}}{\partial \eta} + \frac{\partial \tilde{w}}{\partial z}\right) + \frac{\bar{s}}{h_1}\frac{\partial \tilde{\rho}}{\partial \xi} + \frac{\bar{c}}{h_2}\frac{\partial \tilde{\rho}}{\partial \eta} + \tilde{w}\frac{\partial \bar{\rho}}{\partial z}$$

$$+(\bar{\rho}\tilde{s} + \tilde{\rho}\bar{s})m_{21} + (\bar{\rho}\tilde{c} + \tilde{\rho}\bar{c})m_{12} + \bar{\rho}\tilde{w}(m_{13} + m_{23}) = 0$$

momentum:

$$\xi: \quad \bar{\rho}\left[\frac{\partial \tilde{s}}{\partial t} + \frac{\bar{s}}{h_1}\frac{\partial \tilde{s}}{\partial \xi} + \frac{\bar{c}}{h_2}\frac{\partial \tilde{s}}{\partial \eta} + \tilde{w}\frac{\partial \bar{s}}{\partial z} + (\bar{s}\tilde{c} + \tilde{s}\bar{c})\,m_{12} + \bar{s}\tilde{w}m_{13} - 2\bar{c}\tilde{c}m_{21}\right]$$

$$+\tilde{\rho}(\bar{s}\bar{c}m_{12} - \bar{c}^2 m_{21}) = -\frac{1}{h_1}\frac{\partial \tilde{p}}{\partial \xi} + \frac{\bar{\mu}}{R}\left\{\frac{\partial^2 \tilde{s}}{\partial z^2}\right.$$

$$+\left(1 + \frac{\bar{\lambda}}{\bar{\mu}}\right)\left(\frac{1}{h_1}\frac{\partial^2 \tilde{w}}{\partial \xi \partial z} + \frac{1}{h_1 h_2}\frac{\partial^2 \tilde{c}}{\partial \xi \partial \eta}\right) + \left(2 + \frac{\bar{\lambda}}{\bar{\mu}}\right)\frac{1}{{h_1}^2}\frac{\partial^2 \tilde{s}}{\partial \xi^2} + \frac{1}{{h_2}^2}\frac{\partial^2 \tilde{s}}{\partial \eta^2}$$

$$\left.+\frac{1}{\bar{\mu}}\frac{\partial \bar{\mu}}{\partial \bar{T}}\left[\left(\frac{\partial \tilde{s}}{\partial z} + \frac{1}{h_1}\frac{\partial \tilde{w}}{\partial \xi}\right)\frac{\partial \bar{T}}{\partial z} + \frac{\partial \bar{s}}{\partial z}\frac{\partial \tilde{T}}{\partial z} + \frac{\partial^2 \bar{s}}{\partial z^2}\tilde{T}\right] + \frac{1}{\bar{\mu}}\frac{\partial^2 \bar{\mu}}{\partial \bar{T}^2}\frac{\partial \bar{T}}{\partial z}\frac{\partial \bar{s}}{\partial z}\tilde{T}\right\}$$

$$\eta: \quad \bar{\rho}\left[\frac{\partial \tilde{c}}{\partial t} + \frac{\bar{s}}{h_1}\frac{\partial \tilde{c}}{\partial \xi} + \frac{\bar{c}}{h_2}\frac{\partial \tilde{c}}{\partial \eta} + \tilde{w}\frac{\partial \bar{c}}{\partial z} + (\bar{c}\tilde{s} + \tilde{c}\bar{s})\,m_{21} + \bar{c}\tilde{w}m_{23} - 2\bar{s}\tilde{s}m_{12}\right]$$

$$+\tilde{\rho}(\bar{c}\bar{s}m_{21} - \bar{s}^2 m_{12}) = -\frac{1}{h_2}\frac{\partial \tilde{p}}{\partial \eta} + \frac{\bar{\mu}}{R}\left\{\frac{\partial^2 \tilde{c}}{\partial z^2}\right.$$

$$+\left(1+\frac{\bar{\lambda}}{\bar{\mu}}\right)\left(\frac{1}{h_2}\frac{\partial^2\tilde{w}}{\partial\eta\partial z}+\frac{1}{h_1 h_2}\frac{\partial^2\tilde{s}}{\partial\xi\partial\eta}\right)+\left(2+\frac{\bar{\lambda}}{\bar{\mu}}\right)\frac{1}{{h_2}^2}\frac{\partial^2\tilde{c}}{\partial\eta^2}+\frac{1}{{h_1}^2}\frac{\partial^2\tilde{c}}{\partial\xi^2}$$

$$+\frac{1}{\bar{\mu}}\frac{\partial\bar{\mu}}{\partial\bar{T}}\left[\left(\frac{\partial\tilde{c}}{\partial z}+\frac{1}{h_2}\frac{\partial\tilde{w}}{\partial\eta}\right)\frac{\partial\bar{T}}{\partial z}+\frac{\partial\bar{c}}{\partial z}\frac{\partial\tilde{T}}{\partial z}+\frac{\partial^2\bar{c}}{\partial z^2}\tilde{T}\right]+\frac{1}{\bar{\mu}}\frac{\partial^2\bar{\mu}}{\partial\bar{T}^2}\frac{\partial\bar{T}}{\partial z}\frac{\partial\bar{c}}{\partial z}\tilde{T}\Bigg\}$$

$$z:\quad \bar{\rho}\left[\frac{\partial\tilde{w}}{\partial t}+\frac{\bar{s}}{h_1}\frac{\partial\tilde{w}}{\partial\xi}+\frac{\bar{c}}{h_2}\frac{\partial\tilde{w}}{\partial\eta}-2\bar{s}\tilde{s}m_{13}-2\bar{c}\tilde{c}m_{23}\right]-\tilde{\rho}(\bar{s}^2m_{13}+\bar{c}^2m_{23})=$$

$$-\frac{\partial\tilde{p}}{\partial z}+\frac{\bar{\mu}}{R}\Bigg\{\left(2+\frac{\bar{\lambda}}{\bar{\mu}}\right)\frac{\partial^2\tilde{w}}{\partial z^2}$$

$$\left(1+\frac{\bar{\lambda}}{\bar{\mu}}\right)\left(\frac{1}{h_1}\frac{\partial^2\tilde{s}}{\partial\xi\partial z}+\frac{1}{h_2}\frac{\partial^2\tilde{c}}{\partial\eta\partial z}\right)+\frac{1}{{h_1}^2}\frac{\partial^2\tilde{w}}{\partial\xi^2}+\frac{1}{{h_2}^2}\frac{\partial^2\tilde{w}}{\partial\eta^2}$$

$$+\frac{1}{\bar{\mu}}\frac{\partial\bar{\mu}}{\partial\bar{T}}\left[\left(2+\frac{\bar{\lambda}}{\bar{\mu}}\right)\frac{\partial\tilde{w}}{\partial z}\frac{\partial\bar{T}}{\partial z}+\frac{1}{h_1}\frac{\partial\tilde{T}}{\partial\xi}\frac{\partial\bar{s}}{\partial z}+\frac{1}{h_2}\frac{\partial\tilde{T}}{\partial\eta}\frac{\partial\bar{c}}{\partial z}+\frac{\bar{\lambda}}{\bar{\mu}}\left(\frac{1}{h_1}\frac{\partial\tilde{s}}{\partial\xi}+\frac{1}{h_2}\frac{\partial\tilde{c}}{\partial\eta}\right)\right]\Bigg\}$$

energy:

$$\bar{\rho}\left[\frac{\partial\tilde{T}}{\partial t}+\frac{\bar{s}}{h_1}\frac{\partial\tilde{T}}{\partial\xi}+\frac{\bar{c}}{h_2}\frac{\partial\tilde{T}}{\partial\eta}+\tilde{w}\frac{\partial\bar{T}}{\partial z}\right]-(\gamma-1){M_e}^2\left[\frac{\partial\tilde{p}}{\partial t}+\frac{\bar{s}}{h_1}\frac{\partial\tilde{p}}{\partial\xi}+\frac{\bar{c}}{h_2}\frac{\partial\tilde{p}}{\partial\eta}\right]=$$

$$+\frac{\bar{\mu}}{Pr\,R}\left[\frac{1}{{h_1}^2}\frac{\partial^2\tilde{T}}{\partial\xi^2}+\frac{1}{{h_2}^2}\frac{\partial^2\tilde{T}}{\partial\eta^2}+\frac{\partial^2\tilde{T}}{\partial z^2}+\frac{1}{\bar{k}}\frac{\partial\bar{k}}{\partial\bar{T}}\left(\frac{\partial^2\bar{T}}{\partial z^2}\tilde{T}+2\frac{\partial\bar{T}}{\partial z}\frac{\partial\tilde{T}}{\partial z}\right)\right.$$

$$\left.+\frac{1}{\bar{k}}\frac{\partial^2\bar{k}}{\partial\bar{T}^2}\left(\frac{\partial\bar{T}}{\partial z}\right)^2\tilde{T}\right]$$

$$+\frac{\bar{\mu}(\gamma-1){M_e}^2}{R}\Bigg\{2\left(\frac{\partial\tilde{c}}{\partial z}+\frac{1}{h_2}\frac{\partial\tilde{w}}{\partial\eta}\right)\frac{\partial\bar{c}}{\partial z}+2\left(\frac{\partial\tilde{s}}{\partial z}+\frac{1}{h_1}\frac{\partial\tilde{w}}{\partial\xi}\right)\frac{\partial\bar{s}}{\partial z}+$$

$$\frac{1}{\bar{\mu}}\frac{\partial\bar{\mu}}{\partial\bar{T}}\left[\left(\frac{\partial\bar{c}}{\partial z}\right)^2+\left(\frac{\partial\bar{s}}{\partial z}\right)^2\right]\tilde{T}\Bigg\}$$

The equation of state has a mean flow component and a fluctuating component given by

$$\bar{\rho} = \frac{1}{\bar{T}} \quad \text{and} \quad \tilde{\rho} = (\gamma M_e{}^2)\frac{\tilde{p}}{\bar{T}} - \frac{\tilde{T}}{\bar{T}^2}$$

which are utilized to eliminate $\bar{\rho}$ and $\tilde{\rho}$ from the set of equations derived above. The in-plane curvature coefficients are given by

$$m_{12} = \frac{\delta^*}{h_1 h_2}\frac{\partial h_1}{\partial \eta} \quad \text{and} \quad m_{21} = \frac{\delta^*}{h_1 h_2}\frac{\partial h_2}{\partial \xi}$$

while the surface curvature coefficients are given by

$$m_{13} = \frac{\delta^*}{h_1}\frac{\partial h_1}{\partial z} \quad \text{and} \quad m_{23} = \frac{\delta^*}{h_2}\frac{\partial h_2}{\partial z}$$

In general, the specific curvature coefficients are a function of the configuration under consideration. They will be derived for swept wing geometries in the following chapter. Finally, it must be noted that terms of order $(1/R^2)$ and smaller have not been written in the above analysis. However, the magnitude of the effect of these terms is determined and will be discussed.

2.4 The Linear Stability Equations for Quasi-Parallel Flow

To complete the derivation of the stability equations it is assumed that the disturbance may be described by a harmonic wave of the form

$$\tilde{s} = \Re[\hat{s}(z)\exp i(\alpha\xi + \beta\eta - \omega t)]$$

$$\tilde{c} = \Re[\hat{c}(z)\exp i(\alpha\xi + \beta\eta - \omega t)]$$

$$\tilde{w} = \Re[\hat{w}(z)\exp i(\alpha\xi + \beta\eta - \omega t)]$$

$$\tilde{p} = \Re[\hat{p}(z)\exp i(\alpha\xi + \beta\eta - \omega t)]$$

$$\tilde{T} = \Re[\hat{T}(z)\exp i(\alpha\xi + \beta\eta - \omega t)]$$

where α and β are dimensionless real wavenumbers in the ξ and η directions and ω is the dimensionless complex frequency defined by;

$$\alpha = \alpha^* \delta^* \quad \text{and} \quad \beta = \beta^* \delta^*$$

$$\text{and} \qquad \omega = \frac{2\pi\delta^*}{U_e}\omega^*$$

For this disturbance, the wavenumber vector is defined such that it makes an angle ϕ with the ξ axis;

$$\tan\phi = \frac{\beta}{\alpha} \tag{2.4a}$$

Substitution of these expressions into the equations derived in the previous section results in the following form for the equations governing the growth (or decay) of small disturbances in the flow;

continuity:

$$(m_{21} + i\alpha_0)\hat{s} + (m_{12} + i\beta_0)\hat{c} + (m_{13} + m_{23} - \frac{1}{\bar{T}}\frac{\partial \bar{T}}{\partial z})\hat{w}$$

$$+\gamma {M_e}^2[(m_{21}\bar{s} + m_{12}\bar{c}) + i(\alpha_0\bar{s} + \beta_0\bar{c} - \omega)]\hat{p}$$

$$-\frac{1}{\bar{T}}[(m_{21}\bar{s} + m_{12}\bar{c}) + i(\alpha_0\bar{s} + \beta_0\bar{c} - \omega)]\hat{T} + \hat{w}' = 0$$

momentum:

$$\xi: \quad \frac{1}{\bar{T}}\left[i(\alpha_0\bar{s} + \beta_0\bar{c} - \omega)\hat{s} + \hat{w}\frac{\partial \bar{s}}{\partial z} + (\bar{s}\hat{c} + \hat{s}\bar{c})m_{12} + \bar{s}\hat{w}m_{13} - 2\bar{c}\hat{c}m_{21}\right]$$

$$+\left[(\gamma {M_e}^2)\frac{\hat{p}}{\bar{T}} - \frac{\hat{T}}{\bar{T}^2}\right](\bar{s}\bar{c}m_{12} - \bar{c}^2 m_{21}) = -i\alpha_0\hat{p}$$

$$+\frac{\bar{\mu}}{R}\left\{\hat{s}'' + \left(1 + \frac{\bar{\lambda}}{\bar{\mu}}\right)(i\alpha_0\hat{w}' - \alpha_0\beta_0\hat{c}) - \left(2 + \frac{\bar{\lambda}}{\bar{\mu}}\right){\alpha_0}^2\hat{s} - {\beta_0}^2\hat{s}\right.$$

$$+\frac{1}{\bar{\mu}}\frac{\partial \bar{\mu}}{\partial \bar{T}}\left[(\hat{s}' + i\alpha_0\hat{w})\frac{\partial \bar{T}}{\partial z} + \frac{\partial \bar{s}}{\partial z}\hat{T}' + \frac{\partial^2 \bar{s}}{\partial z^2}\hat{T}\right] + \frac{1}{\bar{\mu}}\frac{\partial^2 \bar{\mu}}{\partial \bar{T}^2}\frac{\partial \bar{T}}{\partial z}\frac{\partial \bar{s}}{\partial z}\hat{T}\Bigg\}$$

$$\eta: \quad \frac{1}{\bar{T}}\left[i(\alpha_0\bar{s} + \beta_0\bar{c} - \omega)\hat{c} + \hat{w}\frac{\partial \bar{c}}{\partial z} + (\bar{c}\hat{s} + \hat{c}\bar{s})m_{21} + \bar{c}\hat{w}m_{23} - 2\bar{s}\hat{s}m_{12}\right]$$

$$+\left[(\gamma {M_e}^2)\frac{\hat{p}}{\bar{T}} - \frac{\hat{T}}{\bar{T}^2}\right](\bar{c}\bar{s}m_{21} - \bar{s}^2 m_{12}) = -i\beta_0\hat{p}$$

$$+\frac{\bar{\mu}}{R}\Bigg\{\hat{c}'' + \left(1 + \frac{\bar{\lambda}}{\bar{\mu}}\right)(i\beta_0\hat{w}' - \alpha_0\beta_0\hat{s}) - \left(2 + \frac{\bar{\lambda}}{\bar{\mu}}\right){\beta_0}^2\hat{c} - {\alpha_0}^2\hat{c}$$

$$+\frac{1}{\bar{\mu}}\frac{\partial \bar{\mu}}{\partial \bar{T}}\left[(\hat{c}' + i\beta_0\hat{w})\frac{\partial \bar{T}}{\partial z} + \frac{\partial \bar{c}}{\partial z}\hat{T}' + \frac{\partial^2 \bar{c}}{\partial z^2}\hat{T}\right] + \frac{1}{\bar{\mu}}\frac{\partial^2 \bar{\mu}}{\partial \bar{T}^2}\frac{\partial \bar{T}}{\partial z}\frac{\partial \bar{c}}{\partial z}\hat{T}\Bigg\}$$

$$z: \quad \frac{1}{\bar{T}}\left[i(\alpha_0\bar{s} + \beta_0\bar{c} - \omega)\hat{w} - 2\bar{s}\hat{s}m_{13} - 2\bar{c}\hat{c}m_{23}\right]$$

$$-\left[(\gamma {M_e}^2)\frac{\hat{p}}{\bar{T}} - \frac{\hat{T}}{\bar{T}^2}\right](\bar{s}^2 m_{13} + \bar{c}^2 m_{23}) = -\hat{p}' + \frac{\bar{\mu}}{R}\Bigg\{\left(2 + \frac{\bar{\lambda}}{\bar{\mu}}\right)\hat{w}''$$

$$\left(1 + \frac{\bar{\lambda}}{\bar{\mu}}\right)\left(i\alpha_0\hat{s}' + i\beta_0\hat{c}'\right) - \alpha_0^2\hat{w} - \beta_0^2\hat{w}$$

$$+\frac{1}{\bar{\mu}}\frac{\partial \bar{\mu}}{\partial \bar{T}}\left[\left(2 + \frac{\bar{\lambda}}{\bar{\mu}}\right)\frac{\partial \bar{T}}{\partial z}\hat{w}' + i\alpha_0\frac{\partial \bar{s}}{\partial z}\hat{T} + i\beta_0\frac{\partial \bar{c}}{\partial z}\hat{T} + \frac{\bar{\lambda}}{\bar{\mu}}\left(i\alpha_0\hat{s} + i\beta_0\hat{c}\right)\right]\Bigg\}$$

energy:

$$\frac{1}{\bar{T}}\left[i(\alpha_0\bar{s} + \beta_0\bar{c} - \omega)\hat{T} + \hat{w}\frac{\partial \bar{T}}{\partial z}\right] - (\gamma - 1){M_e}^2\left[i(\alpha_0\bar{s} + \beta_0\bar{c} - \omega)\hat{p}\right] =$$

$$+\frac{\bar{\mu}}{Pr\,R}\left[-\alpha_0^2\hat{T} - \beta_0^2\hat{T} + \hat{T}'' + \frac{1}{\bar{k}}\frac{\partial \bar{k}}{\partial \bar{T}}\left(\frac{\partial^2 \bar{T}}{\partial z^2}\hat{T} + 2\frac{\partial \bar{T}}{\partial z}\hat{T}'\right)\right.$$

$$+\frac{1}{\bar{k}}\frac{\partial^2 \bar{k}}{\partial \bar{T}^2}\left(\frac{\partial \bar{T}}{\partial z}\right)^2 \hat{T}\Bigg]$$

$$+\frac{\bar{\mu}(\gamma-1)M_e{}^2}{R}\left\{2\left(\hat{c}'+i\beta_0\hat{w}\right)\frac{\partial \bar{c}}{\partial z}+2\left(\hat{s}'+i\alpha_0\hat{w}\right)\frac{\partial \bar{s}}{\partial z}+\right.$$

$$\left.\frac{1}{\bar{\mu}}\frac{\partial \bar{\mu}}{\partial \bar{T}}\left[\left(\frac{\partial \bar{c}}{\partial z}\right)^2+\left(\frac{\partial \bar{s}}{\partial z}\right)^2\right]\hat{T}\right\}$$

where $\alpha_0 = \alpha/h_1$ and $\beta_0 = \beta/h_2$. The boundary conditions are

$$\hat{s} = \hat{c} = \hat{w} = 0 \quad \text{at} \quad z = 0$$

$$\hat{s} \to 0, \quad \hat{c} \to 0, \quad \hat{w} \to 0 \quad \text{as} \quad z \to \infty$$

The equations derived above for the compressible, parallel flow past a three-dimensional curved body govern the temporal stability of a wave embedded in the boundary layer. The wave aligned coordinate system (ξ, η, z) where the wavenumber vector is tangent to the ξ coordinate (see Ref. 28) is an optimal coordinate system for the study of the stability of the boundary layer over a curved surface. However, since the geometric properties of the wave are not known at the beginning of the computation, the solution process is an iterative one. First, an initial orientation of the wave with respect to the x axis is specified at a given frequency ω_r and then, α and β are found such that the temporal amplification rate ω_i is maximized at any point on the surface for a fixed Reynolds number. Once this initial solution is found at all x, y, and z, the ξ, η coordinate system is rotated such that the ξ coordinate is locally aligned with the wavenumber vector; then a new set of stability characteristics is computed. The process is continued until the angle ϕ, and hence β, becomes zero (see Eq. 2.4a).

Chapter 3

SOLUTION OF THE GOVERNING EQUATIONS

Several methods are available for solving the governing linear stability equations. The method used here is the numerical method utilized by the compressible stability analysis computer code, COSAL (Ref. 42). A brief description is given below.

3.1 Determination of the Matrix Coefficients

The system of governing stability equations can be written as

$$(FD^2 + GD + H)\mathbf{T} = 0 \tag{3.1a}$$

Here, F, G, and H are 5×5 matrices and $D \equiv d(\ )/dz$ and $\mathbf{T}$ is a five element vector defined by

$$\mathbf{T} = \begin{bmatrix} \hat{s} \\ \hat{w} \\ \hat{p} \\ \hat{T} \\ \hat{c} \end{bmatrix}$$

The non-zero elements of the matrices F, G, and H are written as;

$$F_{11} = 1 \qquad F_{22} = 1$$

$$F_{44} = 1 \qquad F_{55} = 1$$

$$G_{11} = \frac{1}{\bar{\mu}} \frac{\partial \bar{\mu}}{\partial \bar{T}} \frac{\partial \bar{T}}{\partial z} \qquad G_{12} = i(1 + \frac{\bar{\lambda}}{\bar{\mu}})\alpha_0$$

$$G_{14} = \frac{1}{\bar{\mu}} \frac{\partial \bar{\mu}}{\partial \bar{T}} \frac{\partial \bar{s}}{\partial z} \qquad G_{21} = i\alpha_0 (1 + \frac{\bar{\lambda}}{\bar{\mu}})/(2 + \frac{\bar{\lambda}}{\bar{\mu}})$$

$$G_{22} = G_{11} \qquad G_{23} = -R/\bar{\mu}(2 + \frac{\bar{\lambda}}{\bar{\mu}})$$

$$G_{25} = i\beta_0 (1 + \frac{\bar{\lambda}}{\bar{\mu}})/(2 + \frac{\bar{\lambda}}{\bar{\mu}}) \qquad G_{32} = 1$$

$$G_{41} = 2(\gamma - 1) {M_e}^2 Pr \frac{\partial \bar{s}}{\partial z} \qquad G_{44} = \frac{2}{\bar{k}} \frac{\partial \bar{k}}{\partial \bar{T}} \frac{\partial \bar{T}}{\partial z}$$

$$G_{45} = 2(\gamma - 1) {M_e}^2 Pr \frac{\partial \bar{c}}{\partial z} \qquad G_{52} = i(1 + \frac{\bar{\lambda}}{\bar{\mu}})\beta_0$$

$$G_{54} = \frac{1}{\bar{\mu}} \frac{\partial \bar{\mu}}{\partial \bar{T}} \frac{\partial \bar{c}}{\partial z} \qquad G_{55} = G_{11}$$

$$H_{11} = -(2 + \frac{\bar{\lambda}}{\bar{\mu}}){\alpha_0}^2 - {\beta_0}^2 - i[\frac{R}{\bar{\mu}\bar{T}}(\alpha_0 \bar{s} + \beta_0 \bar{c} - \omega)] - \frac{R\bar{c}}{\bar{\mu}\bar{T}} m_{12}$$

$$H_{12} = -\frac{R}{\bar{\mu}\bar{T}}(\frac{\partial \bar{s}}{\partial z} + m_{13}\bar{s}) + i(\frac{1}{\bar{\mu}} \frac{\partial \bar{\mu}}{\partial \bar{T}} \frac{\partial \bar{T}}{\partial z} \alpha_0)$$

$$H_{13} = -\gamma {M_e}^2 \frac{R}{\bar{\mu}\bar{T}}(\bar{s}\bar{c} m_{12} - \bar{c}^2 m_{21}) - i\frac{R}{\bar{\mu}}\alpha_0$$

$$H_{14} = \frac{R}{\bar{\mu}\bar{T}^2}(\bar{s}\bar{c} m_{12} - \bar{c}^2 m_{21}) + \frac{1}{\bar{\mu}} \frac{\partial \bar{\mu}}{\partial \bar{T}} \frac{\partial^2 \bar{s}}{\partial z^2} + \frac{1}{\bar{\mu}} \frac{\partial^2 \bar{\mu}}{\partial \bar{T}^2} \frac{\partial \bar{T}}{\partial z} \frac{\partial \bar{s}}{\partial z}$$

$$H_{15} = -(1 + \frac{\bar{\lambda}}{\bar{\mu}})\alpha_0 \beta_0 - \frac{R}{\bar{\mu}\bar{T}}(\bar{s} m_{12} - 2\bar{c} m_{21})$$

$$H_{21} = [\frac{2R}{\bar{\mu}\bar{T}} \bar{s} m_{13} + \frac{1}{\bar{\mu}} \frac{\partial \bar{\mu}}{\partial \bar{T}} \frac{\partial \bar{T}}{\partial z} \frac{\bar{\lambda}}{\bar{\mu}} i\alpha_0]/(2 + \frac{\bar{\lambda}}{\bar{\mu}})$$

$$H_{22} = -\left[{\alpha_0}^2 + {\beta_0}^2 + \frac{iR}{\bar{\mu}\bar{T}}(\alpha_0 \bar{s} + \beta_0 \bar{c} - \omega)\right]/(2 + \frac{\bar{\lambda}}{\bar{\mu}})$$

$$H_{23} = \gamma {M_e}^2 \frac{R}{\bar{\mu}\bar{T}}(\bar{s}^2 m_{13} + \bar{c}^2 m_{23})/(2 + \frac{\bar{\lambda}}{\bar{\mu}})$$

$$H_{24} = [-\frac{R}{\bar{\mu}\bar{T}^2}(\bar{s}^2 m_{13} + \bar{c}^2 m_{23}) + i\frac{1}{\bar{\mu}} \frac{\partial \bar{\mu}}{\partial \bar{T}}(\alpha_0 \frac{\partial \bar{s}}{\partial z} + \beta_0 \frac{\partial \bar{c}}{\partial z})]/(2 + \frac{\bar{\lambda}}{\bar{\mu}})$$

$$H_{25} = [\frac{2R}{\bar{\mu}\bar{T}}\bar{c}m_{23} + \frac{1}{\bar{\mu}}\frac{\partial\bar{\mu}}{\partial\bar{T}}\frac{\partial\bar{T}}{\partial z}\frac{\bar{\lambda}}{\bar{\mu}}i\beta_0]/(2+\frac{\bar{\lambda}}{\bar{\mu}})$$

$$H_{31} = m_{21} + i\alpha_0$$

$$H_{32} = m_{13} + m_{23} - \frac{1}{\bar{T}}\frac{\partial\bar{T}}{\partial z}$$

$$H_{33} = \gamma {M_e}^2[m_{21}\bar{s} + m_{12}\bar{c} + i(\alpha_0\bar{s} + \beta_0\bar{c} - \omega)]$$

$$H_{34} = -\frac{1}{\bar{T}}[m_{21}\bar{s} + m_{12}\bar{c} + i(\alpha_0\bar{s} + \beta_0\bar{c} - \omega)]$$

$$H_{35} = m_{12} + i\beta_0$$

$$H_{42} = \frac{-PrR}{\bar{\mu}\bar{T}}\frac{\partial\bar{T}}{\partial z} + i[2(\gamma-1){M_e}^2 Pr(\alpha_0\frac{\partial\bar{s}}{\partial z} + \beta_0\frac{\partial\bar{c}}{\partial z})]$$

$$H_{43} = i[(\gamma-1){M_e}^2 Pr\frac{R}{\bar{\mu}}(\alpha_0\bar{s} + \beta_0\bar{c} - \omega)]$$

$$H_{44} = -{\alpha_0}^2 - {\beta_0}^2 + \frac{1}{\bar{k}}\frac{\partial\bar{k}}{\partial\bar{T}}\frac{\partial^2\bar{T}}{\partial z^2} + \frac{1}{\bar{k}}(\frac{\partial\bar{T}}{\partial z})^2\frac{\partial^2\bar{k}}{\partial T^2} + (\gamma-1){M_e}^2\frac{Pr}{\bar{\mu}}\frac{\partial\bar{\mu}}{\partial\bar{T}}[(\frac{\partial\bar{s}}{\partial z})^2 + (\frac{\partial\bar{c}}{\partial z})^2]$$

$$-i[\frac{PrR}{\bar{\mu}\bar{T}}(\alpha_0\bar{s} + \beta_0\bar{c} - \omega)]$$

$$H_{51} = -(1+\frac{\bar{\lambda}}{\bar{\mu}})\alpha_0\beta_0 - \frac{R}{\bar{\mu}\bar{T}}(\bar{c}m_{21} - 2\bar{s}m_{12})$$

$$H_{52} = -\frac{R}{\bar{\mu}\bar{T}}(\frac{\partial\bar{c}}{\partial z} + m_{23}\bar{c}) + i(\frac{1}{\bar{\mu}}\frac{\partial\bar{\mu}}{\partial\bar{T}}\frac{\partial\bar{T}}{\partial z}\beta_0)$$

$$H_{53} = -\gamma {M_e}^2\frac{R}{\bar{\mu}\bar{T}}(\bar{s}\bar{c}m_{21} - \bar{s}^2 m_{12}) - i\frac{R}{\bar{\mu}}\beta_0$$

$$H_{54} = \frac{R}{\bar{\mu}\bar{T}^2}(\bar{s}\bar{c}m_{21} - \bar{s}^2 m_{12}) + \frac{1}{\bar{\mu}}\frac{\partial\bar{\mu}}{\partial\bar{T}}\frac{\partial^2\bar{c}}{\partial z^2} + \frac{1}{\bar{\mu}}\frac{\partial^2\bar{\mu}}{\partial\bar{T}^2}\frac{\partial\bar{T}}{\partial z}\frac{\partial\bar{c}}{\partial z}$$

$$H_{55} = -(2+\frac{\bar{\lambda}}{\bar{\mu}}){\beta_0}^2 - {\alpha_0}^2 - i[\frac{R}{\bar{\mu}\bar{T}}(\alpha_0\bar{s} + \beta_0\bar{c} - \omega)] - \frac{R\bar{s}}{\bar{\mu}\bar{T}}m_{21}$$

As described in Refs. 30 and 36, the system of Eqs. (3.1*a*) is discretized on a staggered finite difference grid where the velocity perturbations are defined on the nodes and the pressure perturbations are defined on the midpoints. In this way, no pressure boundary conditions are required. Homogeneous velocity perturbation boundary conditions are imposed at the solid boundary ($z = 0$) and in the freestream (which is assumed to be at $z = 100$). The governing equations, along with the boundary conditions, then result in a block-tridiagonal system of equations with 5×5 blocks that is solved using fully pivoted LU factorization. The eigenvalue ω is obtained by the inverse Rayleigh iteration procedure (Ref. 46). For a fixed physical frequency ω_r, the COSCUR code calculates the maximum temporal growth rate ω_i, which then determines α and β. The condition that the group velocity ratio be real for the propagation of a monochromatic wave in a three-dimensional boundary layer (see Ref. 47) is automatically satisfied when the temporal maximum is computed. The group velocity $\mathbf{V}_g = (\partial\omega/\partial\alpha, \partial\omega/\partial\beta)$, which is needed in this maximization procedure and for converting temporal growth to spatial growth, is also calculated in COSCUR. Some tests were conducted for two-dimensional flow over a concave surface and the computed growth rates (using the group velocity transformation) agreed well with the spatial calculations of Ragab and Nayfeh (Ref. 48). An N factor for transition correlation may be defined as

$$N = \int_{j_0}^{j} \frac{\omega_i}{|\Re(\mathbf{V}_g)|} dj \tag{3.1b}$$

where j is the arclength on the solid body along a curve that is everywhere tangent to $\Re(\mathbf{V}_g)$.

3.2 Description of Computations

In order to solve the stability equations (3.1*a*), curvature coefficients must be specified for the swept wing configuration under study. For simplicity, it is

assumed that the surface of the wing be formed from the intersection of several swept cylinders. The cylinders are used only to obtain the curvature coefficients. The natural choice for the fixed reference axes in this case is then the cylindrical polar coordinate system r, θ, ς. For the body fixed system of Figure 5, note that on the windward face

$$x = \int a d\theta, \quad y = \varsigma, \quad \text{and} \quad z = r - a$$

where a is the local radius of curvature of the wing surface. Hence, by considering the length of a small element, it follows that

$$g_1 = 1 + (z/a) \quad \text{and} \quad g_2 = 1$$

The mean boundary layer flow was computed, in this coordinate system, by using a laminar compressible boundary layer code by Kaups and Cebeci (Ref. 49). The pressure distribution used as input to the boundary layer code for the parametric study on the supercritical airfoil was computed utilizing a transonic potential code by Bauer, Garabedian, Korn and Jameson (Ref. 50). Experimental pressure distributions were used for the study of the concave-convex airfoil of Kohama and the swept wing N-factor correlations. The general form of the curvature coefficients in equations 3.1a are given by;

$$m_{12} = \frac{\delta^*}{h_1 h_2}\frac{\partial h_1}{\partial \eta} = b\cos\epsilon\frac{d\epsilon}{dx}$$

$$m_{21} = \frac{\delta^*}{h_1 h_2}\frac{\partial h_2}{\partial \xi} = -b\sin\epsilon\frac{d\epsilon}{dx}$$

$$m_{13} = \frac{\delta^*}{h_1}\frac{\partial h_1}{dz} = \frac{b\cos^2\epsilon}{(1+bz)}$$

$$m_{23} = \frac{\delta^*}{h_2}\frac{\partial h_2}{dz} = \frac{b\sin^2\epsilon}{(1+bz)}$$

where $b = \delta^*/a$. Note that x has been nondimensionalized with respect to a, and z with respect to δ^*.

Previous experience has shown that crossflow vortices align themselves such that the wavenumber vector is nearly normal to that of the flow at the edge of the boundary layer. This is exactly true for Görtler vortices in two-dimensional flows. With this in mind, the initial ξ, η, z coordinate direction was chosen so that the η direction is aligned with that of the local streamline. Therefore, the initial orientation is obtained by setting $\epsilon = \pi/2 - \psi$; i.e.,

$$m_{12} = b \tan \Lambda \sin \psi \cos^2 \psi \frac{f'(x)}{f^2(x)} \qquad \text{(streamline divergence)}$$

$$m_{21} = -b \tan \Lambda \cos^3 \psi \frac{f'(x)}{f^2(x)} \qquad \text{(streamline curvature)}$$

$$m_{13} = \frac{b \sin^2 \psi}{(1 + bz)} \qquad \text{(surface curvature in the } \xi \text{ direction)}$$

$$m_{23} = \frac{b \cos^2 \psi}{(1 + bz)} \qquad \text{(surface curvature in the } \eta \text{ direction)}$$

where $f(x) = u_e/U_\infty$ and ψ is the angle between the external streamline and the x direction,

$$\tan \psi = \frac{v_e}{u_e} = \frac{v_\infty}{U_\infty f(x)} = \frac{\tan \Lambda}{f(x)}$$

This system of coordinates (ξ, η, z) worked very well as a starting point for this problem with convergence being complete after three iterations.

Chapter 4

RESULTS AND DISCUSSION

The linear stability equations including the parallel flow assumption have been derived for the compressible flow past curved three-dimensional bodies. The equations are solved utilizing the same numerical method as that in the well known compressible linear stability code, COSAL. In order to check the analysis derived above, the compressible equations including curvature are coded in the program COSCUR. Comparisons are made in section 4.1 between the new COSCUR code with the curvature terms set to zero and the COSAL code. Also, a check is to be made against an incompressible stability code including the curvature terms, SALCUR. In section 4.2, a parametric study is done to examine the effects of sweep on the Görtler instability and to examine the magnitude of the de-stabilizing effects of concave curvature on the crossflow instability. This parametric study is done with the SALCUR code including the curvature terms. Finally, in section 4.3, the new COSCUR code is utilized to determine the magnitude of the stabilizing effects of concave curvature on the crossflow instability for compressible flows past swept wings. N-factor correlations are made utilizing COSCUR and compared with N-factor correlations from the COSAL and the SALCUR codes.

4.1 Verification of the Extended Compressible Stability Analysis

Shown in Table 3 are the results of the verification of the extended compressible stability analysis derived above. The tests are performed at a location where the local surface curvature is convex; therefore, when the curvature terms are "on" the temporal amplification decreases. The first entry in the table are the results

of a simple eigenvalue computation from the COSAL computer code. For this test, the eigenvalue ω and the components of the group velocity, V_a and V_b are calculated at a single X/C location for a given profile. The imaginary part of ω is the temporal amplification rate. The second entry is the new COSCUR code with the curvature terms set to zero. As can be seen, the results are nearly identical indicating that the compressible terms in the COSCUR code are correct. Entries 3 and 4 compare the incompressible stability analysis with curvature (SALCUR) and the compressible code derived above (COSCUR), respectively. In this case, the compressible code has $M_e = 0$ and $\bar{T}(z)/T_e = 1.0$ in an attempt to turn the compressible terms off. Again there is very good agreement indicating that the curvature terms in the analysis derived above are correct. The fifth entry in Table 3 shows the results from the new COSCUR code with the curvature terms from the viscous part of the equations set to zero. As can be seen from entry 6, including these curvature terms in the calculation results in very slight decrease (about .014%) in the temporal amplification rate. This series of tests lends credibility to the accuracy of the extended analysis derived above.

4.2 The Effects of Sweep on the Görtler Instability

It is known that Görtler vortices are present in two-dimensional flow over a concave surface and that, if the crossflow Reynolds number is large enough, crossflow disturbances are to be expected in a three dimensional boundary layer regardless of the sign of the surface curvature. It is the goal here to examine the effects of increasing sweep (or crossflow Reynolds number) on the Görtler vortex structure. Also, the effect of concave curvature on the crossflow instability will be examined. The 'parallel flow' stability equations given above are valid for both the crossflow and Görtler vortices, since the main interest here are the most amplified disturbances which correspond to high wavenumbers. In general, the Görtler vortex structure is represented by parabolic partial differential equations not amenable

to normal mode analysis (see Ref. 34). Malik and Poll (Ref. 30) showed that unsteady ($\omega_r \neq 0$) crossflow disturbances may be more unstable than the steady disturbances. The same may be true for Görtler vortices in three-dimensional boundary layers. For this part of the study, however, the computations are restricted to steady ($\omega_r = 0$) disturbances only, though the analysis given above applies to the unsteady disturbances.

Linear stability calculations have been made for the concave region of a supercritical airfoil utilizing the SALCUR code. Various combinations of sweep angle Λ and freestream chord Reynolds number R_C used to compute the mean flow are given in Table 4 for the surface geometry shown in Figure 6. The region of interest for this study is the concave zone of the airfoil which extends from about 7% chord to 16.5% chord on the lower surface as shown in Figures 6 and 7. Here, negative values of $\bar{\kappa} = C_n/a$ represent concave curvature.

Cases 1-5 from Table 4 were analyzed utilizing the pressure distribution shown in Figure 8 at $M_n = 0.75$. The suction distribution given in Figure 9 was applied to the boundary layer calculation to prevent laminar separation in the adverse pressure gradient region of the concave zone. For each case, the normal Mach number (and hence the normal pressure distribution) was held constant, $M_n = 0.75$, as sweep was increased. The normal chord C_n was 6.51 feet. Since results from Cases 1-5 showed similar trends, detailed stability analysis results will be presented for cases 1 and 5 only. These results are shown in Figures 10-26.

Shown in Figure 10 is the crossflow Reynolds number as a function of position for the conditions of Cases 2-5. As expected, the magnitude of R_{cf} at a given X/C increases as sweep increases. For this study, the Görtler number, G_L, is defined as $R_L(|\bar{\kappa}|)^{1/2}$, where $\bar{\kappa}$ is the local surface curvature along the inviscid streamline path normalized with L. The G_L distribution is presented in Figure 11 and is shown to be nearly constant as sweep is increased for the conditions of Cases 1-5.

The Görtler number is positive at all X/C, however, it is meaningful only in the concave region.

First, the results for the zero sweep case (Case 1) are presented for reference purposes. The velocity vector plot in the ξ, z plane at the streamwise location which gave the greatest local amplification rate, $X/C = 0.1047$, is shown in Figure 12. The associated normalized eigenfunction plots are presented in Figures 13-15. The counter-rotating vortex structure shown in Figure 12 is for the most amplified wavelength. The value of $\lambda_w / \delta_{0.995}$=1.083 is typical of the most amplified Görtler vortices. The ratio $\lambda_w / \delta_{0.995}$ increases from unity as the crossflow Reynolds number increases and approaches a value of about 3 which is typical of crossflow vortices. The eigenfunction plots are also typical of the Görtler vortex structure in that the components in the axial and normal directions (η, z directions) have zero imaginary parts and the component across the vortex (ξ direction) has zero real part. In addition, the value of $\hat{c}_{max}$ is almost two orders of magnitude larger than $\hat{s}_{max}$ and $\hat{w}_{max}$ (see Figures 13-15). In conventional two-dimensional Görtler vortex studies, this information about the relative magnitude of various eigenfunction components and their phase relations is used explicitly to derive simplified governing equations.

Presented in Figures 16-19 are the results of Case 5, $\Lambda = 30$ degrees, at the streamwise location where the amplification rate is the greatest. This occurs at $X/C = 0.1059$, where $R_{cf} = 246$ is a maximum in the concave region. As can be seen from the velocity vector plot, Figure 16, the vortex structure at this location is of the crossflow type, i.e., of a co-rotating nature. In fact, this was the case for the conditions of Cases 2, 3, and 4, also. Figure 16 is essentially a plot of velocity components s and w, where;

$$s = \bar{s} + \bar{\epsilon}\tilde{s} \quad \text{and} \quad w = \bar{\epsilon}\tilde{w}$$

in which $\bar{\epsilon}$ was assigned a value of 0.2. Other values of this parameter were also tried in order to study the sensitivity of the vortex structure and qualitatively similar results were obtained. It should be pointed out that the vortex structure was of the crossflow type from the point where instability was first detected, about 9% chord, for Cases 2-5. In this region, the Görtler number is low, i.e., less than 10, and the crossflow Reynolds number is increasing. For Case 5, the parameter $\lambda_w/\delta_{0.995} = 2.794$ which is typical for crossflow-type disturbances. The shape of the eigenfunctions presented in Figures 17-19 is also typical for crossflow type disturbances.

The results from Case 5 at $X/C = 0.1330$, a location where R_{cf} is near 35 and the Görtler number is about 21, are shown in Figures 20-23. As can be seen from the velocity vector plot, Figure 20, the vortex structure is of the Görtler counter-rotating type; however, the structure is highly skewed. This result indicates that the vortex structure would develop from the crossflow type, present where crossflow Reynolds number is higher, to the Görtler type as the crossflow Reynolds number approaches zero. The wavelength to boundary layer thickness ratio was calculated to be 1.480 which is near the expected value for Görtler type disturbances. Even at this low R_{cf}, the eigenfunctions (Figures 18-20) for this case do not resemble typical results for the counter-rotating type disturbances in 2-D flows; but, look more like those for a co-rotating type disturbance. There is a definite trend of departure from Görtler to crossflow type eigenfunctions with increasing sweep as can be seen in Figure 23.

Presented in Figure 24 is the disturbance orientation with respect to the streamline direction for the conditions of Cases 2-5. As the sweep angle increases (hence, also the maximum crossflow Reynolds number), the orientation angle of the wave with respect to the external streamline at the point of maximum amplification increases. For Case 5, where the crossflow Reynolds number is higher, the axis of the crossflow vortex makes an angle of about 4 degrees with the streamline

direction. This result is consistent with previous observations and calculations involving flows with crossflow type disturbances (Ref. 51) . As the disturbance develops in the streamwise direction and transforms to the Görtler structure, the angle with the streamline direction decreases to almost zero.

The spatial disturbance amplification rate at the fractional chord location where it is a maximum is shown in Figure 25 as a function of sweep angle for the conditions of Cases 1-5. The results seem to indicate that the centrifugal effects due to the concave curvature result in a higher amplification rate for the Görtler structure at zero degrees of sweep than the crossflow structure at non-zero sweep angles. In addition, as the sweep angle increases, the centrifugal effects decrease with regard to the amplification of the crossflow disturbances for the conditions of Cases 2-5. The amplification rate drops by almost 50% when the sweep is increased from 0 to 30 degrees. However, since the streamlines are curved in a three-dimensional boundary layer, the distance for vortex amplification (see Eq. 3.1b) *increases* with increasing sweep. As a consequence, the total vortex amplification will not be smaller by 50% when $\Lambda = 30$ degrees. In fact, the N-factor is 4.3 when the sweep is zero and 3.0 when the sweep is 30 degrees, a decrease of about 30% in the N factor.

The effects of the curvature terms in the governing equations have been shown to be stabilizing in flowfields over convex walls (Ref. 30). For flows over concave walls, the curvature terms are destabilizing. The amplification rate versus position for the case of 30 degrees sweep is presented in Figure 26 with and without the curvature terms included in the analysis. The peak amplification rate, as well as the N factor, is almost 33% higher for the case where streamline and surface curvature terms are included in the analysis when compared with the calculation where the terms are neglected.

The stability of the boundary layer on the surface shown in Figure 27 was studied experimentally by Kohama (Ref. 35). For that study, flow visualization

and hot-wire anemometer techniques were used to study the flowfield through the concave zone in detail for sweep angles of 0 degrees and 47 degrees for unit Reynolds numbers up to about 200,000/ft. The concave region extends from about 16% chord to about 33.5% chord. The measured streamwise pressure distribution from the study is shown in Figure 28. The nearly constant pressure distribution through the concave region, utilized to avoid laminar separation, was achieved in the experiment by tailoring the walls of the test section. Little variation in the pressure distribution was reported for the speed range of about 20 ft./sec. to 32 ft./sec. . Cases 6-8 were studied so that comparisons can be made with the experimental observations of Kohama for the case of 47 degrees sweep. Detailed results of the calculations are presented in Figures 29-40 for Case 7 only.

The effect of the nearly constant pressure distribution shown in Figure 27 on the mean flow calculations is to keep the crossflow Reynolds number under 50 in the concave region to about 30% chord on the airfoil for the speed range considered (see Fig. 29) . However, beyond 30% chord, the crossflow Reynolds number increases very rapidly. As can be seen in Figure 30, the Görtler number in the concave region is between 15 and 29 for the given test conditions. Kohama observed the existence of the Görtler vortex structure in this concave region . Presented in Figures 31-40 are the velocity vector plots at incremental chord locations through the concave region. The careful examination of Figures 31-34 shows the development of the Görtler vortex; from a weak counter-rotating vortex structure (Figure 31) to a stronger vortex pair as the Görtler number increases and R_{c_f} decreases (see Figure 34). Here, at $X/C = 0.23$ the crossflow Reynolds number is about 28, a minimum, and the amplification is the greatest. Also, $\lambda_w / \delta_{0.995} = 1.20$, which is consistent with previous observations for the Görtler vortex structure. Kohama also observed that the Görtler vortex developed into a crossflow type disturbance before the end of the concave region. This can be explained by the fact that the favorable pressure gradient starts before the end of the concave region causing a rapid increase in the

crossflow Reynolds number, thereby resulting in a disturbance of the crossflow type. This result is presented in Figures 35-40 which shows the velocity vectors plotted for $X/C = 0.2470$ to $X/C = 0.3342$. The crossflow Reynolds number increases from 29 to at $X/C = 0.2470$ to 94 at $X/C = 0.3342$ resulting in the development of a co-rotating crossflow vortex (see Figure 40) from the Görtler vortex pair. Similar results were predicted for Cases 6 and 8. In a given physical situation, the transformation from counter-rotating to co-rotating structures will depend upon various factors, including the strength of the vortex, the Görtler number, and the crossflow Reynolds number. For the cases studied in this paper, it appears that only the co-rotating structure exists when R_{cf} is in excess of 45. It should be noted that at this value of R_{cf}, crossflow instability will be absent on a convex or flat surface. This emphasizes the role that concave curvature plays in the instability of three-dimensional boundary layers.

4.3 Calibration of the Extended Compressible Stability Analysis (COSCUR)

The stability of the laminar boundary layer at several flight conditions on two recent flight tests was calculated using various types of linear stability theory. The calculations were made for test points where crossflow type disturbances were strongly amplified and Tollmien-Schlichting disturbances were negligible. The six cases studied are shown in Table 5. The experimental flight data presented are sensitive; therefore, specific details of the pressure distribution cannot be presented here. The calculations were made utilizing the maximum amplification option in three codes compared in section 4.1. Simply stated, this option searches for the combination of wavelength and wave orientation at a given fixed frequency which yields the highest amplification rate. Several calculations must be performed to identify the frequency which is most amplified. However, it is still not clear which are more important in the transition process in flows of this type: stationary (zero frequency) crossflow vortices or travelling "crossflow like" disturbances. The

calculations compare the compressible, linear stability theory (COSAL) with the new compressible, linear theory including the streamline and surface curvature terms in the governing equations (COSCUR). Included in the comparison, are the results from the incompressible stability theory with curvature (SALCUR). The N-factor has been correlated with the measured transition location. The detailed results from Cases 9 and 10 are shown in Figures 41-46. The transition data and N-factor correlations for all six cases are summarized in Table 6.

The pressure coefficient and crossflow Reynolds number distributions versus X/C for Case 9 are presented in Figures 41 and 42. The sweep angle is 20 degrees. The transition location was estimated to be near 25% chord based on the output of the hot film instrumentation on the wing. The shape of the pressure distribution indicates that the flow is accelerating over the upper surface of the wing to about 50 % chord. One would expect highly amplified crossflow vortices to exist in this flow. It has been shown from previous low speed investigations that R_{cf} at transition varies in the range of 175-300. As can be seen from Figure 42, R_{cf} is about 425 at transition in this case.

The compressible stability theory (COSAL) compared with the new compressible stability theory with curvature included in the analysis (COSCUR) is presented in Figure 43. Also shown is the incompressible theory including the curvature terms (SALCUR). The frequency range considered is between 0 and 4000 Hertz; but, only the results for the most amplified frequency (2000 Hz.) at the transition location and the results for stationary vortices are shown. As mentioned earlier, the travelling crossflow disturbances have been shown to be amplified more than the stationary disturbances for highly three-dimensional flows (see Ref. 30). The results from COSAL show that the N-factor at transition is 17 and 14.5 at 2000 Hz. and 0 Hz., respectively. On the other hand, with the curvature terms included, the results from COSCUR show that the N-factor at transition is about 9 at the most amplified frequency of 2000 Hz. and about 5 for the stationary crossflow

disturbances. The results reveal the powerful stabilizing effect of convex surface curvature and streamline curvature on the stability of the laminar boundary layer. The incompressible analysis (SALCUR) resulted in a N-factor at transition of about 10. This result is not surprising, since it is known that compressibility effects in this speed range are not large. These results compare well with the calculations of Malik on the rotating disk and the swept cylinder (Refs. 29 and 30). In the case of the rotating disk experiment, the N-factor at transition decreased from about 20 to about 11 when streamline curvature and Coriolis effects were included in the analysis. The swept cylinder results revealed that the N-factor at transition decreased from 17 to 11 due to curvature of the surface and streamlines.

The pressure coefficient and the crossflow Reynolds number distributions for Case 10 are presented in Figures 44 and 45. In this case, the transition front was near 45% chord. Because of the fact that the pressure distribution is nearly the same as the previous case, the movement of the transition front is believed to be due to a lower chord Reynolds number. As can be seen in Figure 45, R_{c_f} at transition is about 470. The same trends in the N-factor correlation exist for this flight condition. Referring to Figure 46, one sees that including the curvature terms in the compressible stability analysis results in a decrease in N-factor at transition of about 53% ; from about 19 to about 9 at the most amplified frequency. The incompressible results of SALCUR gave an N-factor of about 11. The results from the four other cases considered in this study are summarized in Table 6. The average value of the N-factor at transition for these six cases at the most amplified frequency was 8.9 when curvature was considered. Conversely, the COSAL code without curvature predicted on the average an N-factor of 16.8.

The motivation for this work was to develop a more accurate transition prediction tool for swept wing flows which is useful across the entire speed range as well as to gain insight into the physics of laminar boundary layer stability. Referring to Figure 43, the use of the COSAL code which does not include curvature based

on an e^9 criteria for the conditions of Case 9 predicts the location of transition at 5% chord. In reality, transition occurred at about 25% chord. Utilization of the new COSCUR code which does include curvature predicts that transition is at 26% chord based on the e^9 criteria. This is typical of the other five cases considered also. These results make it clear that curvature plays an important role in the transition prediction process for flows past swept wings.

Chapter 5

CONCLUSIONS

Based on the results discussed in the previous chapter, the following major conclusions can be drawn:

1. As the crossflow Reynolds number increases beyond 45 in the flow past a swept concave surface, the Görtler vortex structure evolves to the crossflow vortex structure.
2. Centrifugal effects due to concave curvature were shown to destabilize the crossflow instability resulting in amplification rates 33% higher than those computed without curvature included in the analysis.
3. It was shown that by comparing prediction with experimental observation, the linear stability analysis correctly predicts the structures existing in the boundary layer, including the orientation and wavelength.
4. It was shown that for flow past a swept convex surface the crossflow instability is damped dramatically when the surface and streamline curvature terms are included in the analysis.
5. For the six cases studied here, the average N-factor at transition was 8.9 when computed including the curvature terms as opposed to 16.8 when computed without the curvature terms.
6. It was shown that the linear stability analysis without curvature included in the analysis can be ultra-conservative when utilized to predict the onset of transition based on the e^9 criteria.

Chapter 6

SUMMARY

The linear stability equations which govern the growth of small periodic disturbances for compressible, three-dimensional laminar boundary layer flow were derived in an orthogonal curvilinear coordinate system. The streamline and surface curvature terms were retained. The parallel flow assumption was utilized in the derivation. The system of equations was solved using a finite difference scheme similar to that in a current state-of-the-art stability analysis code, COSAL. The LR method and the inverse Rayleigh iteration procedure was used to calculate the eigenvalues.

A parametric study was performed varying Reynolds number and sweep angle on an airfoil with a concave cutout in the leading edge region of the lower surface utilizing the SALCUR code. It is known that convex curvature has a stabilizing effect on the stability of the laminar boundary layer. Conversely, concave curvature has a destabilizing effect. It was shown that as the crossflow Reynolds number increased beyond 45 in the flow past the concave cutout, the Görtler vortices transformed to the crossflow vortex structure. Also, the centrifugal effects due to concave curvature were shown destabilize the crossflow instability resulting in an increase of the amplification rates of about 33% .

The stability of the three-dimensional compressible laminar boundary layer including the effects of streamline and surface curvature for flows past swept wings where crossflow type disturbances dominate was calculated utilizing the code derived above (COSCUR). N-factor correlations at the measured location of transition are made utilizing flight test data. Results indicate that amplification rates

and hence, N-factors, for swept wing flows over convex surfaces are reduced by about 30 to 50 percent when curvature effects are included in the linear stability analysis. For the six cases studied, the average N-factor at transition was 8.9 when the analysis included the curvature terms derived above. An average value of 16.8 was calculated utilizing the COSAL code which does not include curvature in the analysis.

LITERATURE CITED

1. Wagner, R. D., Maddalon, D. V.,and Fischer, M. C., "Technology Developments for Laminar Boundary Layer Control on Subsonic Transport Aircraft," *Improvement of Aerodynamic Performance Through Boundary Layer Control and High Lift Systems, AGARD Report No. 365,* pp. 16-1 to 16-13.

2. Hefner, J. N. and Bushnell, D. M., "Status of Linear Boundary Layer Stability Theory and the e^N Method, with Emphasis on Swept-Wing Applications," *NASA TP 1645,* April, 1980.

3. Bushnell, D. M. and Tuttle, M. H., "Survey and Bibliography on Attainment of Laminar Flow Control in Air Using Pressure Gradient and Suction," *NASA RP 1035, Vol. 1,* September 1979.

4. Tuttle, M.H. and Maddalon, D.V., "Laminar Flow Control (1976-1982), A Selected Annotated Bibliography," *NASA TM 84496,* August 1982.

5. Wagner, R. D., Maddalon, D. V., Bartlett, D. W., Collier, Jr., F. S., and Braslow, A. L., "Laminar Flow Flight Investigations," *presented at the NASA Langley Transonic Aerodynamics Symposium,* April 19-21, 1988 (to be published as a NASA CP).

6. Reynolds, O., "On the Experimental Investigation of the Circumstances Which Determine Whether the Motion of Water Shall be Direct on Sinuous, and the Law of Resistance in Parallel Channels," *Phil, Trans. Roy. Soc., Vol. 174,* 1883, pp. 935-982.

7. Reynolds, O., "On the Dynamical Theory of Incompressible Viscous Fluids and the Determination of the Criterion," *Phil. Trans. Roy. Soc. A186,* 1885, pp. 123-164.

8. Rayleigh, Lord, "On the Stability of Certain Fluid Motions," *Proc. Math. Soc. London 11,* 1880, p.57 and *19,* 1887, p.67; *Scientific Papers 1,* pp. 474-478 and *3,* p. 17.

9. Tollmien, W., "Uber die Entstehung der Turbulenz," *Nachr. Ges. Wiss. Göttingen, Math.-phys. Klasse,* 1929, pp. 21-44.

10. Tollmien, H., "Ein allgemeines Kriterium der Instabiltät laminarer Geschwindigkeitsverteilungen," *Nachr. Ges. Wiss. Göttingen, Math.-phys. Klasse, Vol. 50,* 1935, pp. 79-114.

11. Schlichting, H., "Zur Entstehung der Turbulenz bei der Plattenströmung," *Nachr. Ges. Wiss. Göttingen, Math.-phys. Klasse,* 1933a, pp. 181-208.

12. Schlichting, H., "Berechnung der Anfachung kleiner Störungen bei der Plattenströmung," *ZAMM, Vol. 13,* 1933b, pp. 171-174.

13. Schubauer, G. B. and Skramstead, H. K., "Laminar Boundary Layer Oscillations and Transitions on a Flat Plate," *J. Aero. Sci., Vol.14,* 1947, pp. 69-76.

14. Mack, L. M., "Boundary-Layer Linear Stability Theory," *Special course on Stability and Transition of Laminar Flows, AGARD Report No. 709,* VKI, Brussels, 1984.

15. Schlichting, H., "Boundary Layer Theory", *7th Ed., McGraw-Hill,* NY, 1979.

16. Gray, W.E., "The Effect of Wing Sweep on Laminar Flow," *RAE TM Aero. 255,* 1952.

17. Anscombe, A., and Illingworth, L. N., "Wind Tunnel Observations of Boundary Layer Transition on a Wing at Various Angles of Sweepback," *R.and M. No. 2968,* British A.R.C. 1956.

18. Gregory, N., "Transition and the Spread of Turbulence on a 60 degree Swept Back Wing," *J.R. Aeronautical Society, Vol. 64, No. 597,* September 1960, pp. 562-564.

19. Pfenninger, W., "Some Results from the X-21 Program, Part 1, Flow Phenomena at the leading Edge of Swept Wings," *Agardograph 97, Part IV,* May 1965.

20. Landeryou, R. R., and Trayford, R. S., "Flight Tests at a Laminar Flow Swept Wing with Boundary Layer Control by Suction," *Report 174,* College of Aeronautics, June 1964.

21. Gregory, N., and Love, E. M., "Laminar Flow on a Swept Leading Edge: Final Progress Report," *NPL AERO MEMO. No. 26,* British A.R.C., October 1965.

22. Gaster, M., "On The Flow Along Swept Leading Edges," *CoA-AERO-167,* College of Aeronautics, Cranfield, England, October 1965.

23. Bacon, J. W., Jr., and Pfenninger, W., "Transition Experiments at the Front Attachment Line of a 45 degree Swept Wing With a Blunt Leading Edge," *AFFDL-TR-67-33,* U.S. Air Force, June 1967.

24. Pfenninger, W. and Bacon, J. W., Jr., "Amplified Laminar Boundary Layer Oscillations and Transition at the Front Attachment Line of a 45 degree Swept Flat-Nosed Wing With and Without Boundary Layer Suction," *Viscous Drag Reduction, C. Sinclair Wells, ed., Plenum Press,* 1969, pp. 85-105.

25. Pfenninger, W., "Laminar Flow Control - Laminarisation," *Special course on Concepts for Drag Reduction, AGARD Report 654,* March 1977.

26. Poll, D. I. A., "Transition Description and Prediction in Three-Dimensional Flows," *Special course on Stability and Transition of Laminar Flows, AGARD Report No. 709,* VKI, Brussels, 1984.

27. Owen, P. R. and Randall, D. J., "Boundary Layer Transition on the Swept Back Wing," *RAE TM Aero 257,* 1952.

28. Gregory, N., Stuart, J. T., and Walker, J. S., "On The Stability of Three Dimensional Boundary Layers with Application to the Flow Due to a Rotating Disk," *Phil. Trans. Roy. Soc., Ser. A, Vol. 248,* 1955, pp. 155-199.

29. Malik, M. R., Wilkinson, S. P.,and Orszag, S. A., "Instability and Transition in Rotating Disk Flow," *AIAA J., Vol. 19,* 1981, p. 1131.

30. Malik, M. R. and Poll, D. I. A., "Effect of Curvature on Three-Dimensional Boundary Layer Stability," *AIAA Journal, Vol. 23, No. 9,* September 1985, pp. 1362-1369.

31. Taylor, G. I., "Stability of a Viscous Liquid Contained Between Two Rotating Cylinders," *Phil. Trans. A. Vol. 223,* 1923, pp. 289-343.

32. Görtler, H., "Über eine dreidimensionale Instabilität laminarer Grenzschichten an konkaven Wänden," *Nachr. Wiss. Ges. Gottingen, Math. Phys. Klasse, Neue Folge 2, No. 1,* 1940.

33. Görtler, H., "On The Three Dimensional Instability of Laminar Boundary Layers on Concave Walls," *NACA TM 1375,* 1954.

34. Hall, P., "The Görtler Vortex Instability Mechanism in Three-Dimensional Boundary Layers," *NASA CR-172370,* 1984.

35. Kohama, Y., "Three Dimensional Boundary Layer Transition on a Curved Wall," presented at *IUTAM Symposium on Turbulence Management and Relaminarization,* Bangalore, India, January 19-23, 1987.

36. Collier, Jr., F. S. and Malik, M. R., "Stationary Disturbances In Three Dimensional Boundary Layers," *AIAA Paper 87-1412, presented at AIAA 19th Fluid Dynamics, Plasma Dynamics and Lasers Conference,* Honolulu, Hawaii, June 8-10, 1987.

37. Smith, A. M. O. and Gamberoni, N., "Transition, Pressure Gradient and Stability Theory," *Report No. ES 26388,* Douglas Aircraft Co., Inc., El Segundo, CA, 1956.

38. Van Ingen, J. L., "A Suggested Semi-Empirical Method for the Calculation of the Boundary Layer Transition Region," *Report VTH-74 Delft,* Univ. of Tech., Dept. of Aero. Engr., Holland, 1977.

39. Boeing Commercial Airplane Company, "Flight Survey of the 757 Wing Noise Field and Its Effect on Laminar Boundary Layer Transition," *NASA CR 178419, Vol. 3-Extended Data Analysis,* May, 1988.

40. Srokowski, A. and Orzag, S. A., "Mass Flow Requirements for LFC Wing Design," *AIAA Paper No. 77-1222,* 1977.

41. Dagenhart, J. R., "Amplified Crossflow Disturbances in the Laminar Boundary Layer on Swept Wings with Suction," *NASA TP 1902,* November, 1981.

42. Malik, M. R., "COSAL-A Black Box Compressible Stability Analysis Code for Transition Prediction in Three-Dimensional Boundary Layers," *NASA CR-165925,* 1982.

43. Mack, L. M., "Compressible Boundary Layer Stability Calculations for Swept Back Wings with Suction," *AIAA Journal Vol. 20,* 1981, pp. 363-369.

44. Lekoudis, S., "Stability of the Boundary Layer on a Swept Wing with Wall Cooling," *AIAA J. Vol. 18,* 1980, pp. 1029-1035.

45. Cebeci, T. and Stewartson, K., "Stability and Transition in Swept Wing Flows," *AIAA J. Vol. 18,* 1980, pp. 398-405.

46. Wilkinson, J. H., *The Algebraic Eigenvalue Problem,* Oxford University Press, London, 1965.

47. Nayfeh, A. H.,"Stability of Three-Dimensional Boundary Layers," *AIAA Journal, Vol. 18,* April, 1980, pp. 406-416.

48. Ragab, S. A. and Nayfeh, A. H., "Effect of Pressure Gradient on Görtler Instability," *AIAA Paper 80-1377,* July 1980.

49. Kaups, K. and Cebeci, T., "Compressible Laminar Boundary Layers on Swept and Tapered Wings," *Journal of Aircraft, Vol. 14,* July 1977, pp. 661-667.

50. Bauer, F., Garabedian, P., Korn, D., and Jameson, A., "Supercritical Wing Sections II," *Lecture Notes in Economics and Mathematical Systems, Springer-Verlag, Vol. 108,* 1975.

51. Poll, D. I. A., "Some Observations of the Transition Process on the Windward Face of a Long Yawed Cylinder," *J. Fluid Mech., Vol. 150,* 1985, p. 329.

TABLES

Table 1

Comparison of a LFC transport design with an advanced turbulent design (from Ref. 1)

Mission: 400 passengers and 6500 nm.	Adv. Turbulent	LFC
Take off gross weight (lb.)	645,073	590,496
Fuel burn (lb.)	274,073	214,711
Aquisition cost ($M)	79.2	81.1
Incremental fuel cost ($M/yr.)	3.9	0

Table 2

Some environmental disturbances of concern in LFC design (from Ref. 2)

I. Roughness
    - Insect remains
    - Discrete
    - Continuous
    - Two dimensional
    - Three dimensional
    - Steps
    - Gaps
    - Particle impact/erosion
    - Corrosion
    - Leakage

II. Wall Waviness
    - Two dimensional
    - Three dimensional
    - Single wave
    - Multiple wave
    - Distortion under load
        - Aerodynamic
        - Hydrodynamic
        - Sun/heat

III. Surface and Duct Vibration

IV. Acoustic Environment
    - Attached flow
    - Separated flow
    - Propulsion system
    - Vortex shedding

Table 2-Continued

Some environmental disturbances of concern in LFC design (from Ref. 2)

V. Stream Fluctuations and Vorticity
- Propeller wakes
- Ocean Surface
- Body wakes
  - Fish
  - Aircraft
- High shear areas
  - Weather fronts
  - Jet stream edges
  - Ocean currents

VI. Particles
- Ice clouds
- Rain
- Algae
- Suspensions

VII. LFC-Systems Generated Disturbances
- Vortex shedding (blocked slots, holes, pores)
- Acoustic or chugging
- Pore disturbances
- Nonuniformities

Table 3

Verification of the compressible linear stability analysis including curvature

	ω	V_a	V_b
COSAL	(0.000539726005, 0.00370853869)	(0.721742488, 0.034732889)	(-0.022079681, -0.001069481)
COSCUR $m_{ij} = 0$	(0.000539726005, 0.00370853869)	(0.721742487, 0.034732889)	(-0.022079728, -0.001069483)
SALCUR	(0.00104819624, 0.00177177198)	(0.683824222, 0.056484365)	(-0.019884173, -0.002054571)
COSCUR $M_e = 0$	(0.00104818169, 0.00177158782)	(0.683821257, 0.056487610)	(-0.019188300, -0.002055321)
COSCUR $O(\frac{1}{R^2}) = 0$	(0.001564640155, 0.00150025353)	(0.700080899, 0.056312050)	(-0.018783411, -0.002010248)
COSCUR $O(\frac{1}{R^2}) \neq 0$	(0.001564075020, 0.00150004941)	(0.700076359, 0.056313139)	(-0.018783033, -0.002010923)

Table 4

Case study of sweep effects on the Görtler instability

Case	M_n	Λ (degrees)	$R_G \times 10^{-6}$
1.	0.75	0.0	3.56
2.	0.75	5.0	3.59
3.	0.75	10.0	3.67
4.	0.75	15.0	3.82
5.	0.75	30.0	4.74
6.	≈0.0	47.0	0.56
7.	≈0.0	47.0	0.90
8.	≈0.0	47.0	1.13

Table 5

Flight conditions utilized for the calibration
of the compressible stability analysis including curvature

Case	M_∞	Λ (degrees)	$R_C \times 10^{-6}$
9.	0.80	20.0	24
10.	0.80	20.0	21
11.	0.80	20.0	18
12.	0.80	20.0	15
13.	0.80	21.0	30
14.	0.70	21.0	23

Table 6

Summary of calibration results

Case	Code	Frequency (Hz.)	X/C_{tr}	N_{tr}
9.	COSAL	2000	25.0% C	17
9.	COSCUR	2000	25.0% C	9
10.	COSAL	1500	45.0% C	19
10.	COSCUR	1500	45.0% C	9
11.	COSAL	2000	35.0% C	15
11.	COSCUR	2000	35.0% C	8
12.	COSAL	2000	35.0% C	16.5
12.	COSCUR	2000	35.0% C	9
13.	COSAL	1000	20.0% C	19
13.	COSCUR	1000	20.0% C	10.5
14.	COSAL	1000	12.5% C	14
14.	COSCUR	1000	12.5% C	8

FIGURES

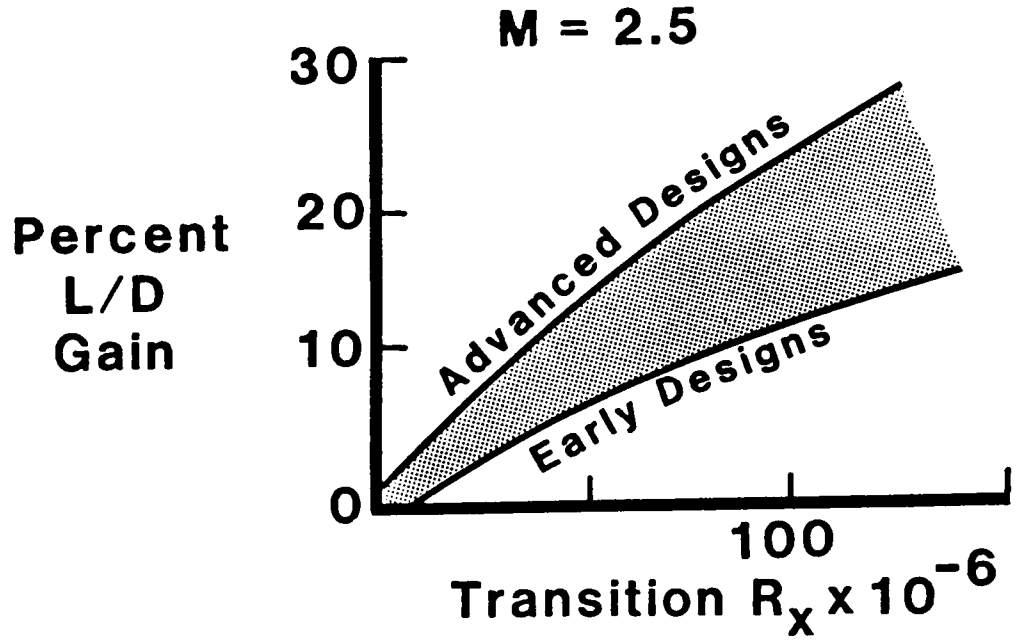

Figure 1: Potential improvement in L/D as function of transition Reynolds number for advanced laminar flow control (LFC) designs.

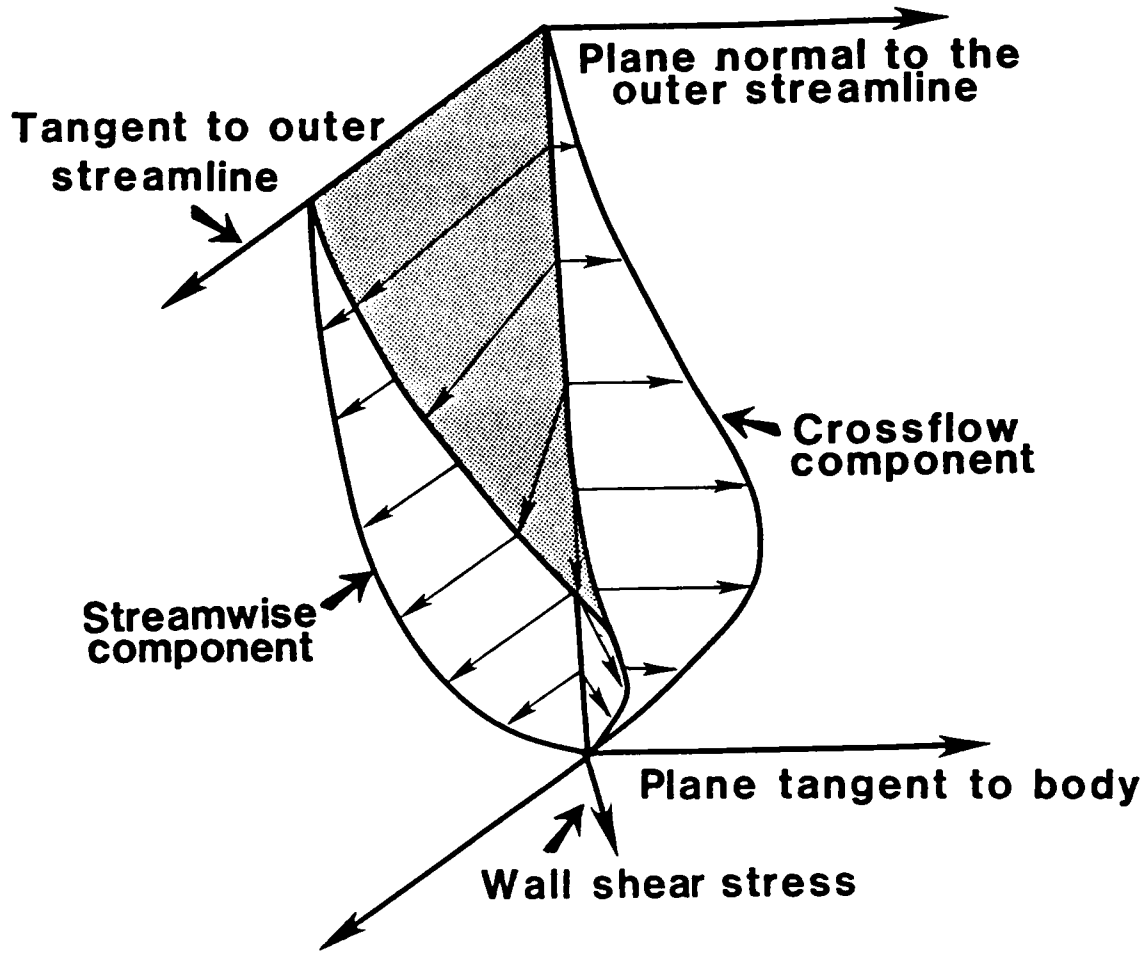

Figure 2: Schematic of the crossflow and streamwise velocity profiles.

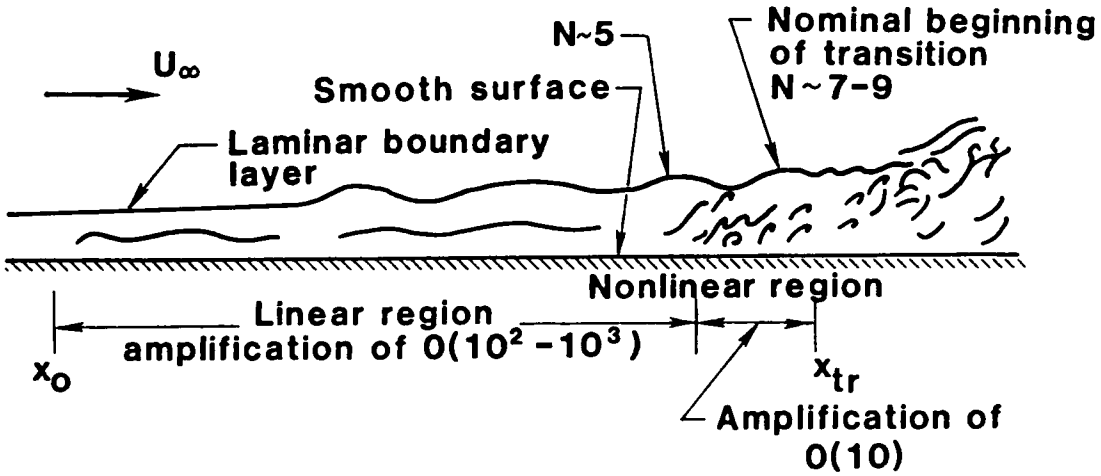

Figure 3: Boundary layer disturbance growth for low background disturbance levels (Reference 2).

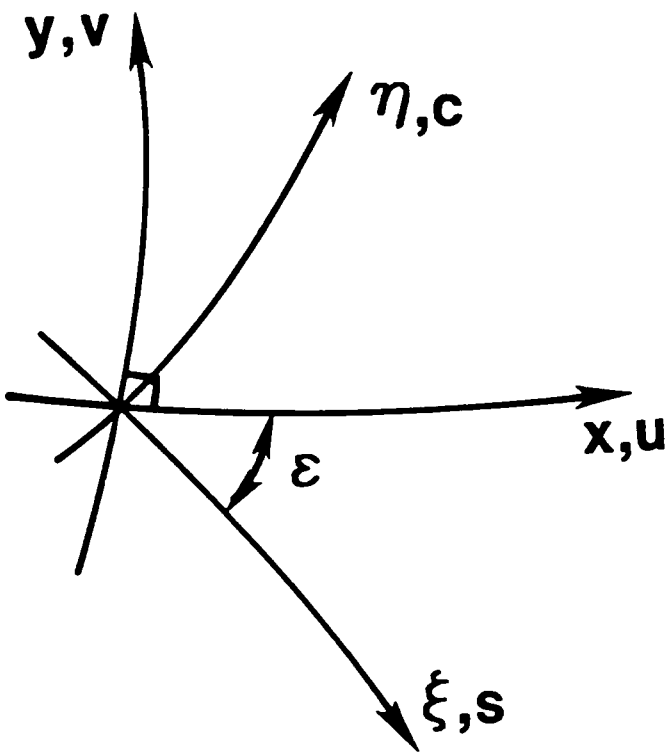

Figure 4: Notation for the fixed reference (x, y) and wave aligned (ξ, η) systems of orthogonal curvilinear coordinates.

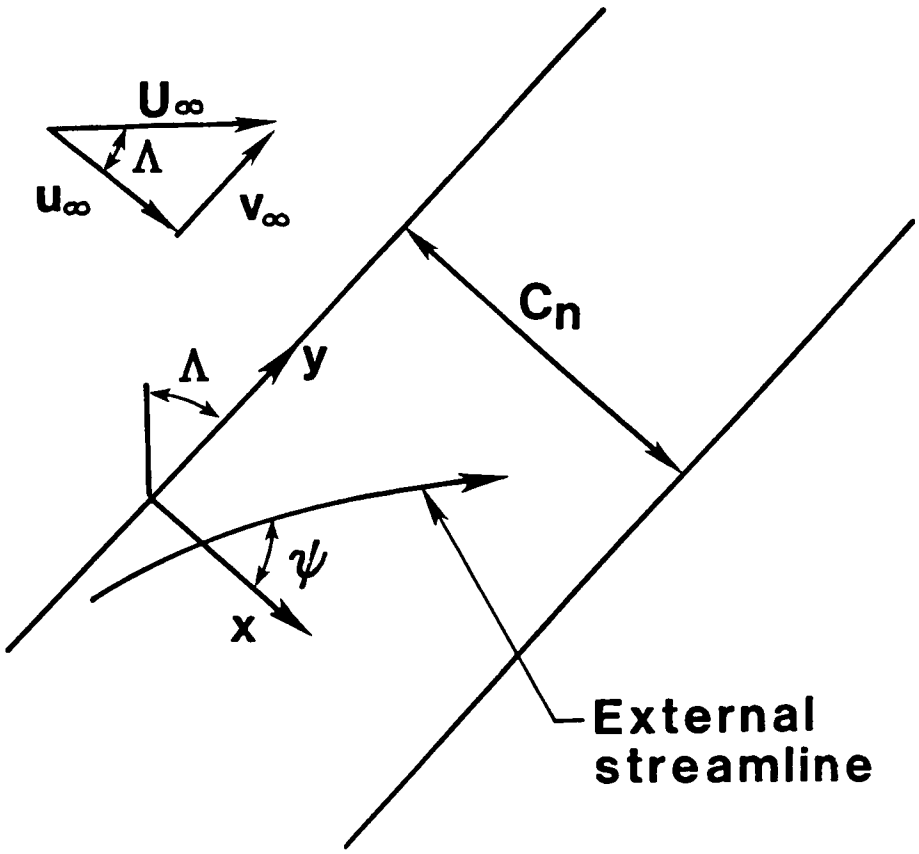

Figure 5: Notation for the infinite swept wing; Cases 1-8.

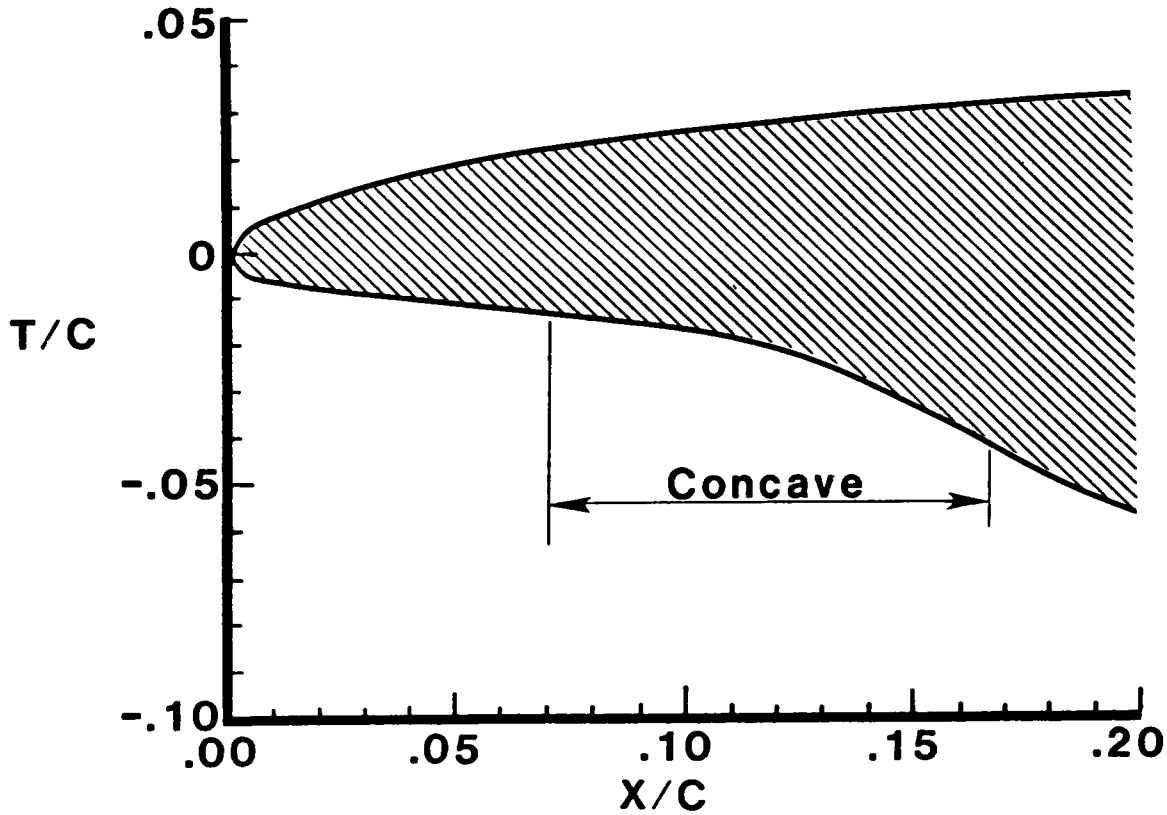

Figure 6: Airfoil surface geometry as a function of position; Cases 1-5.

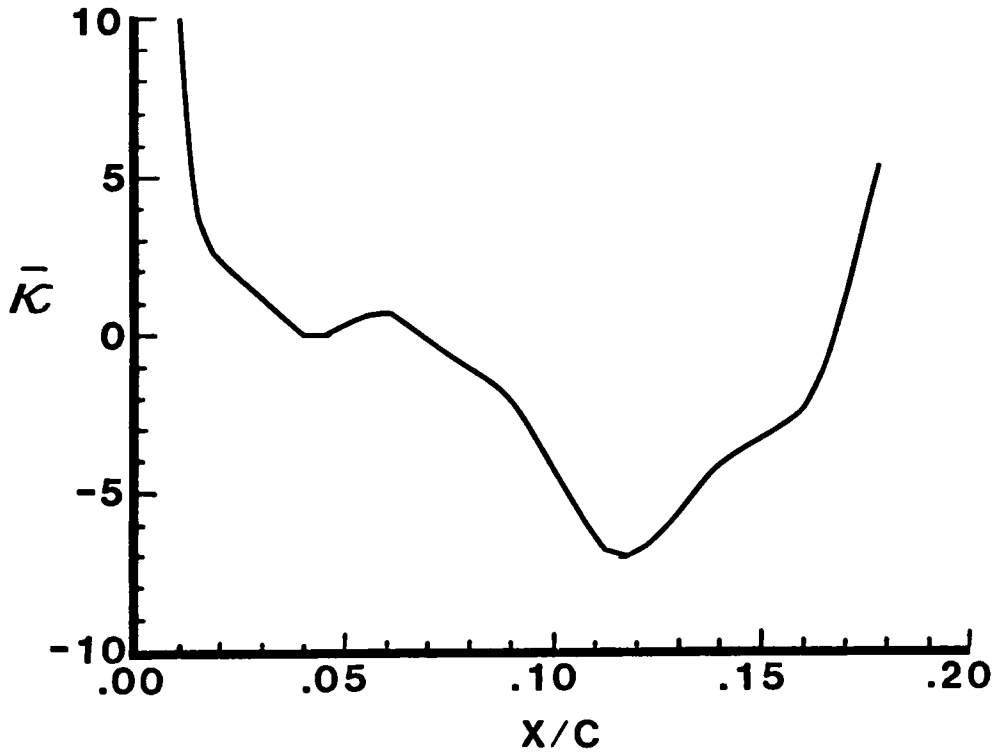

Figure 7: Nondimensional surface curvature as a function of position; Cases 1-5.

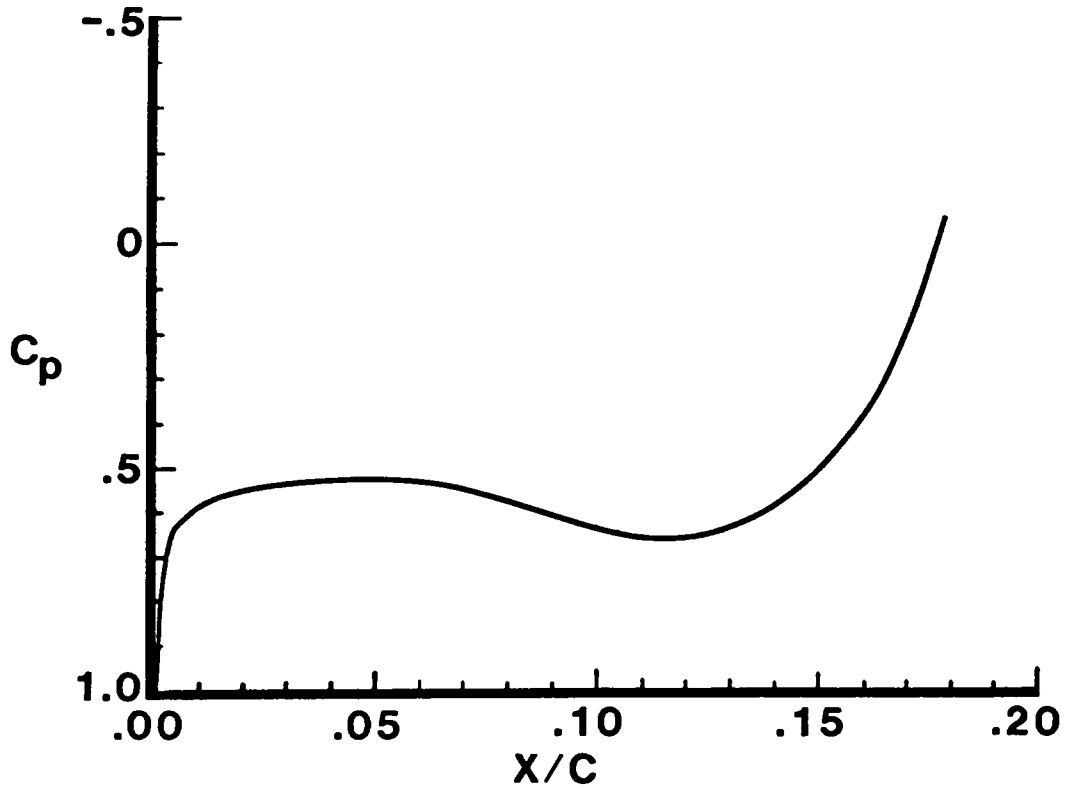

Figure 8: Pressure coefficient distribution as a function of position; Cases 1-5.

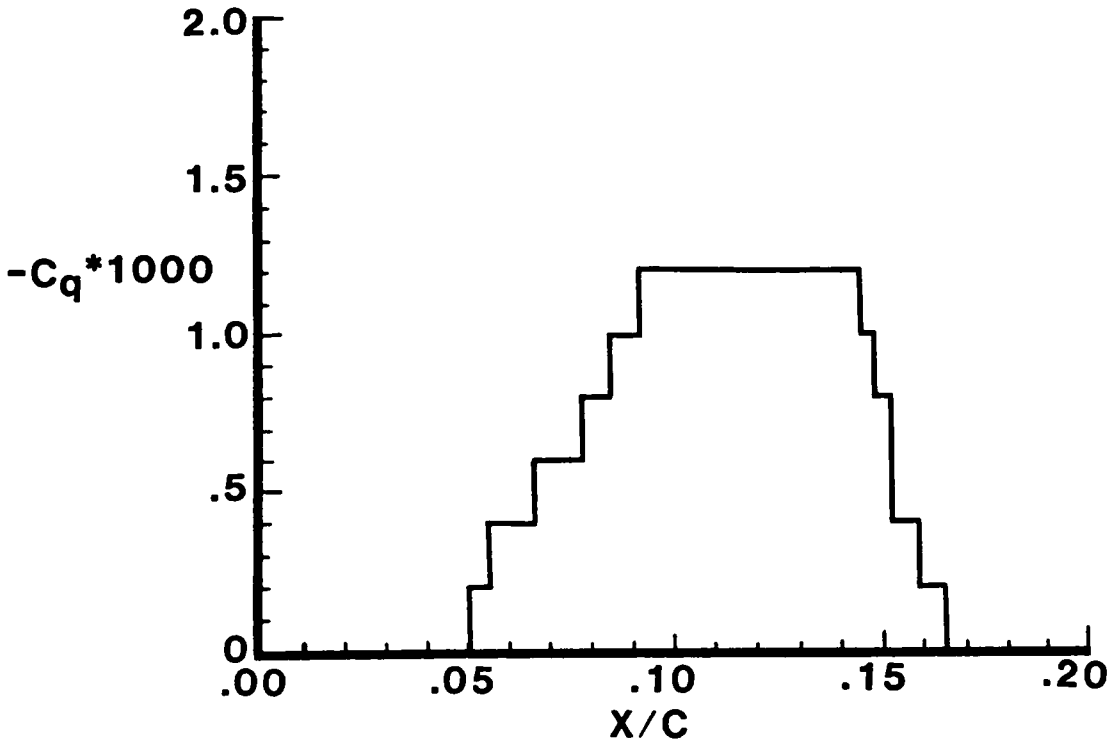

Figure 9: Suction coefficient as a function of position; Cases 1-5.

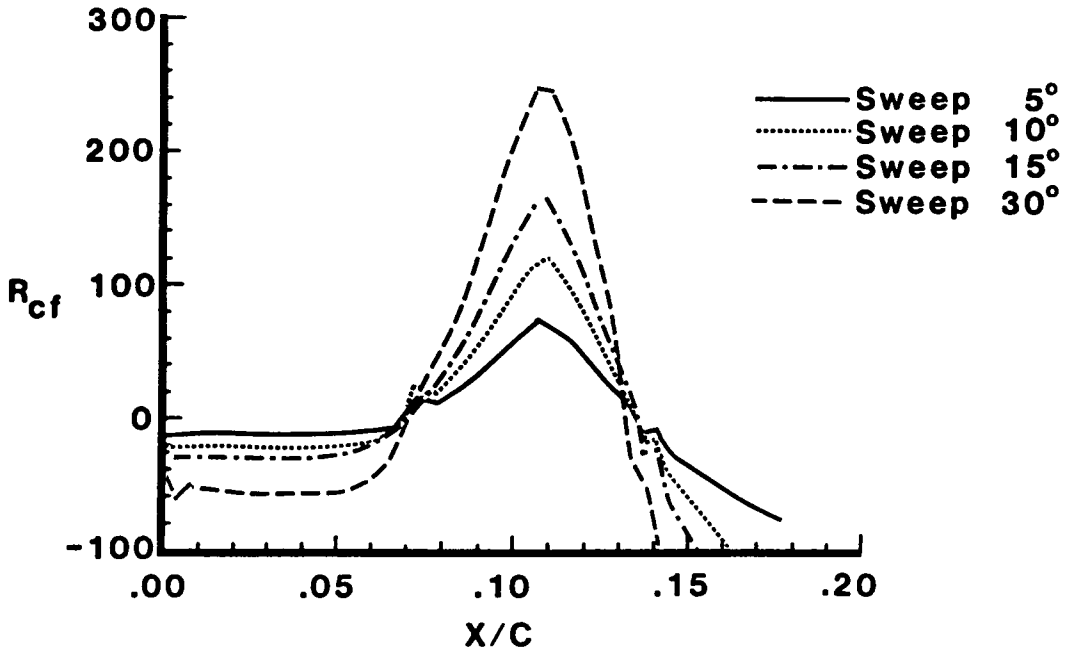

Figure 10: Crossflow Reynolds number as a function of position for Cases 2-5.

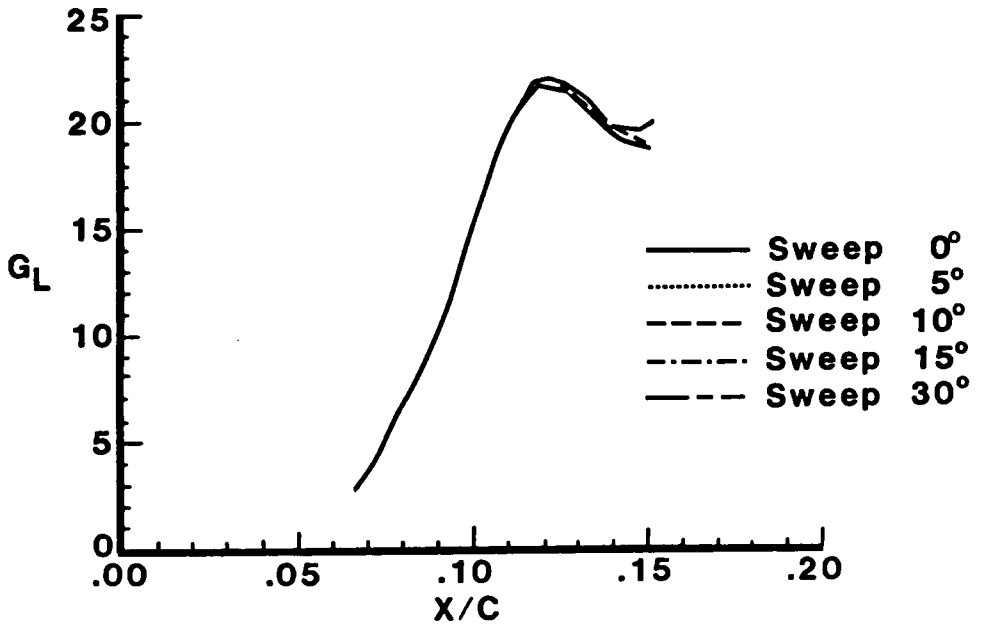

Figure 11: Görtler number distribution as a function of position for Cases 1-5.

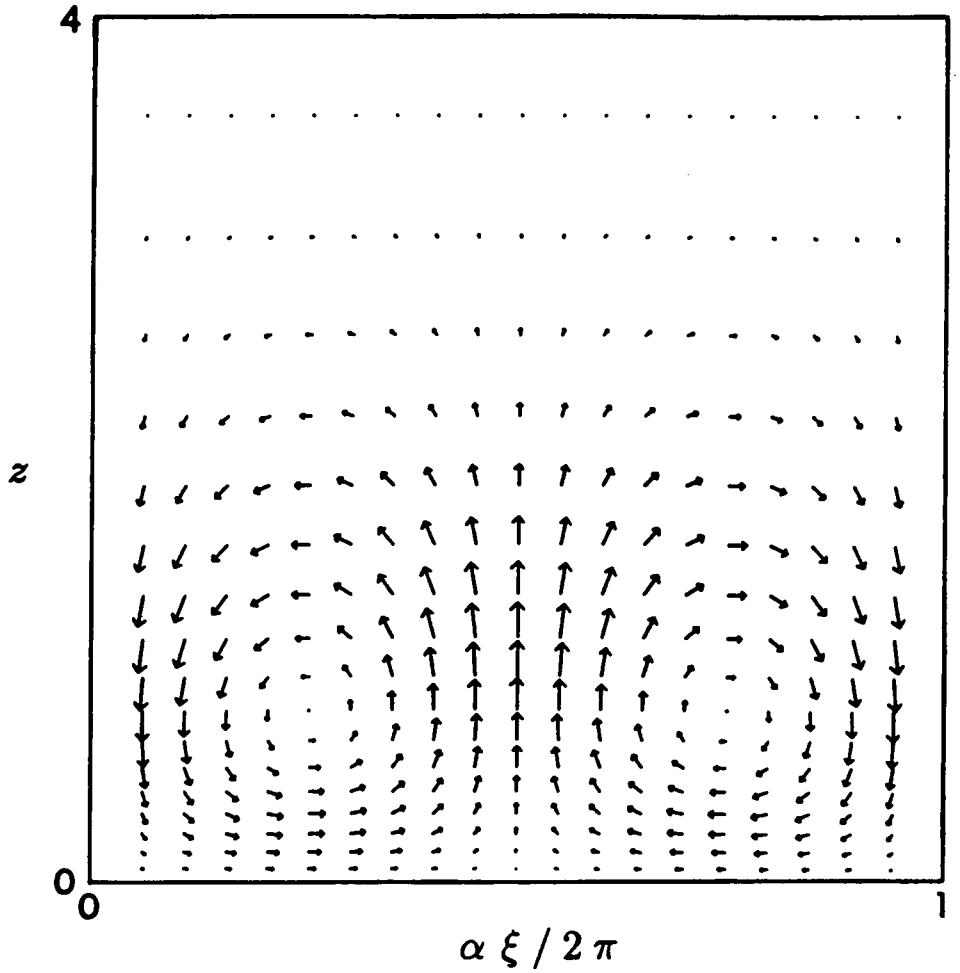

Figure 12: Velocity vector plot in the ξ, z plane for the conditions of Case 1; $X/C = 0.1047$, $\lambda_w / \delta_{0.995} = 1.083$, $R_{cf} = 0$.

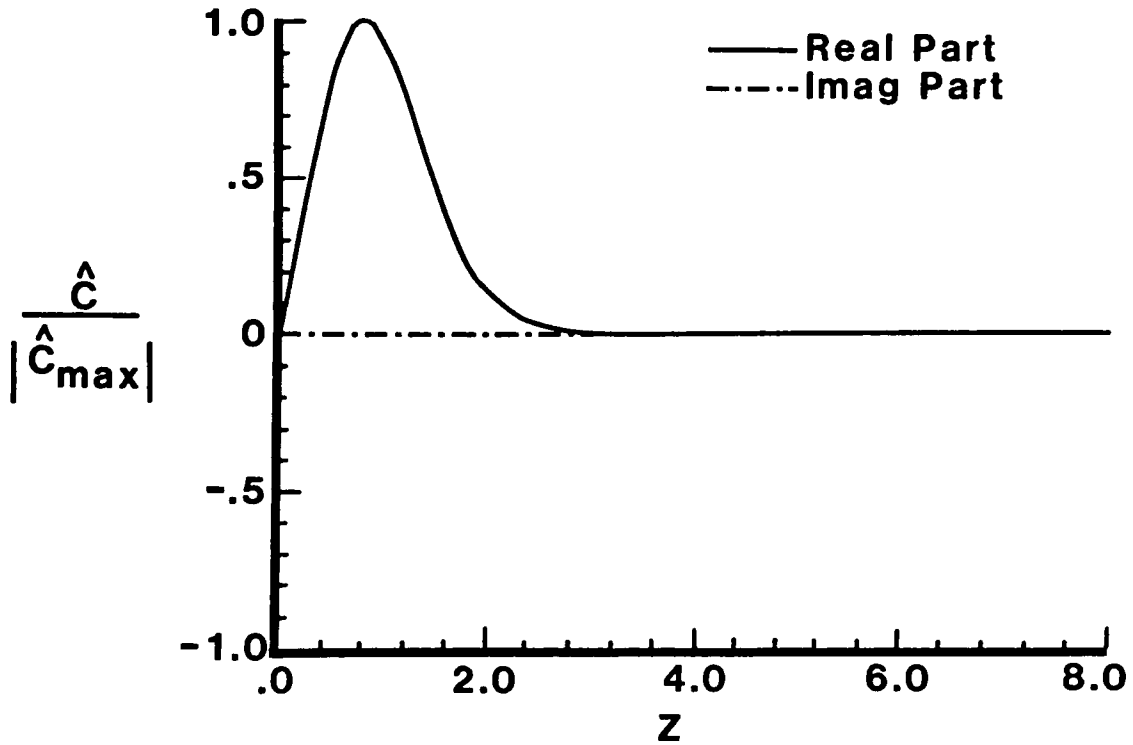

Figure 13: Normalized eigenfunction in the η direction for conditions of Case 1; $X/C = 0.1047$, $\hat{c}_{max} = (1.0, 0.0)$.

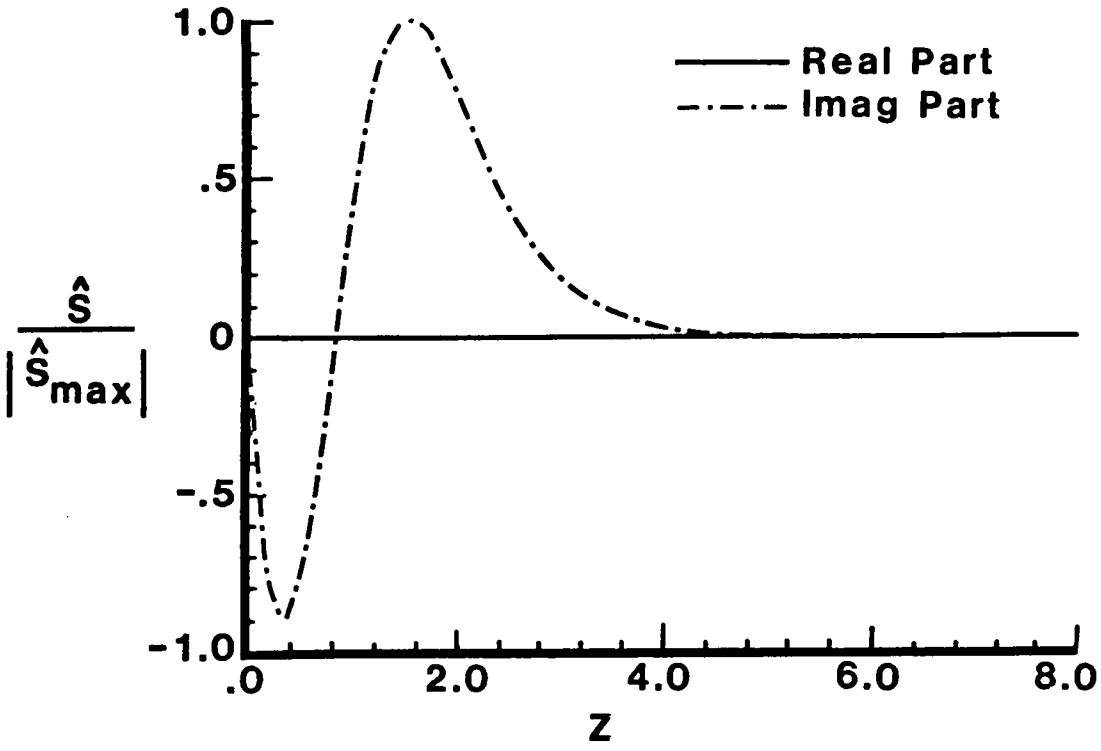

Figure 14: Normalized eigenfunction in the ξ direction for conditions of Case 1; $X/C = 0.1047$, $\hat{s}_{max} = (0.0, 0.025)$.

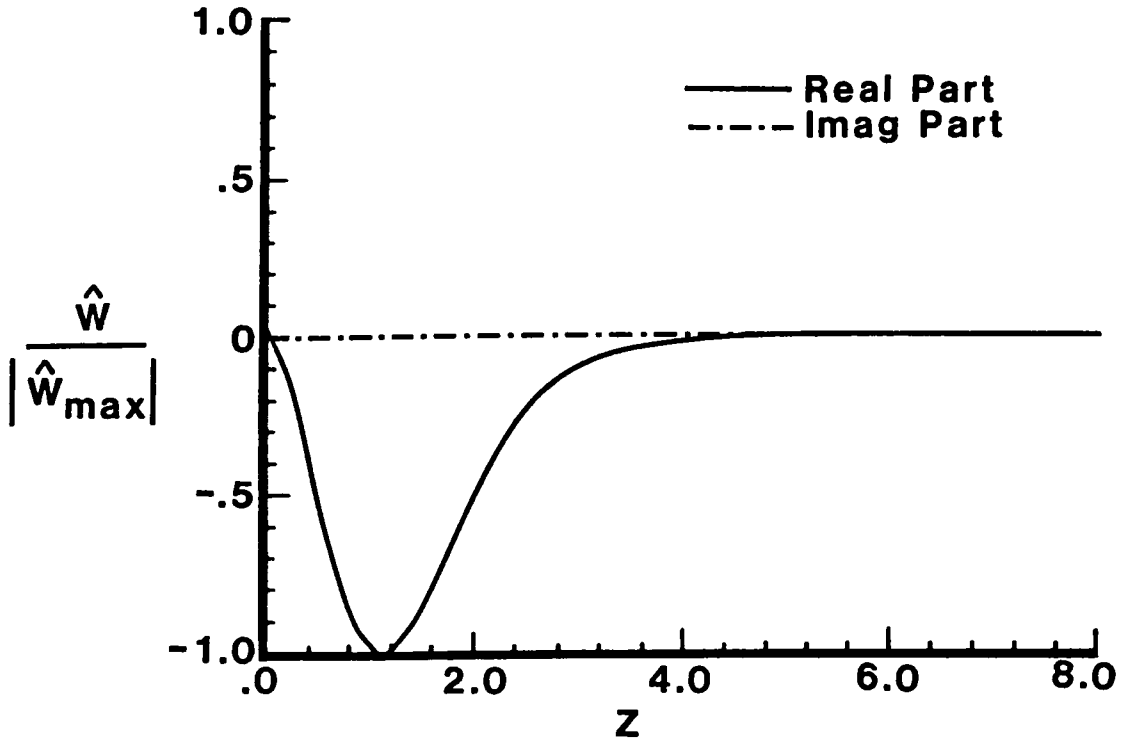

Figure 15: Normalized eigenfunction in the z direction for conditions of Case 1; $X/C = 0.1047$, $\hat{w}_{max} = (-0.047, 0.0)$.

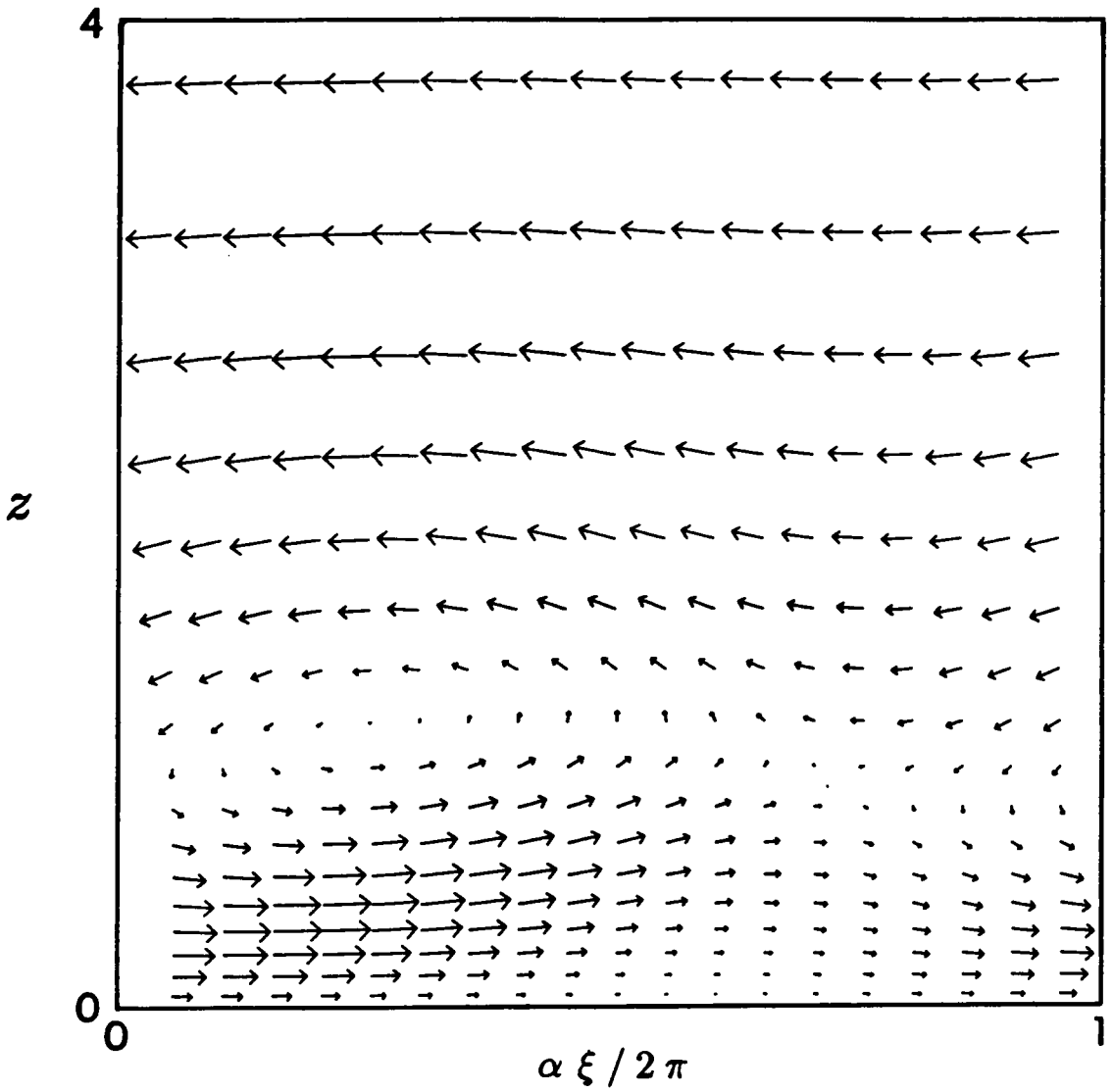

Figure 16: Velocity vector plot in the ξ, z plane for the conditions of Case 5; $X/C = 0.1059$, $\lambda_w / \delta_{0.995} = 2.794$, $R_{cf} = 246$.

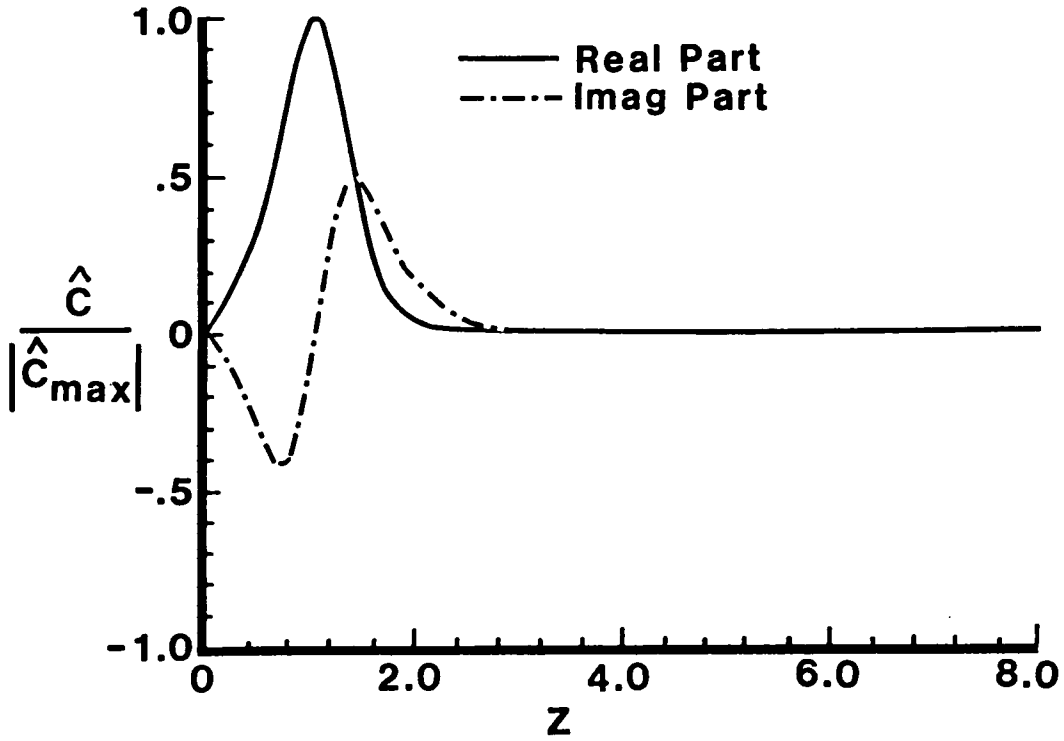

Figure 17: Normalized eigenfunction in the η direction for conditions of Case 5; $X/C = 0.1059$, $\hat{c}_{max} = (1.0, 0.0)$.

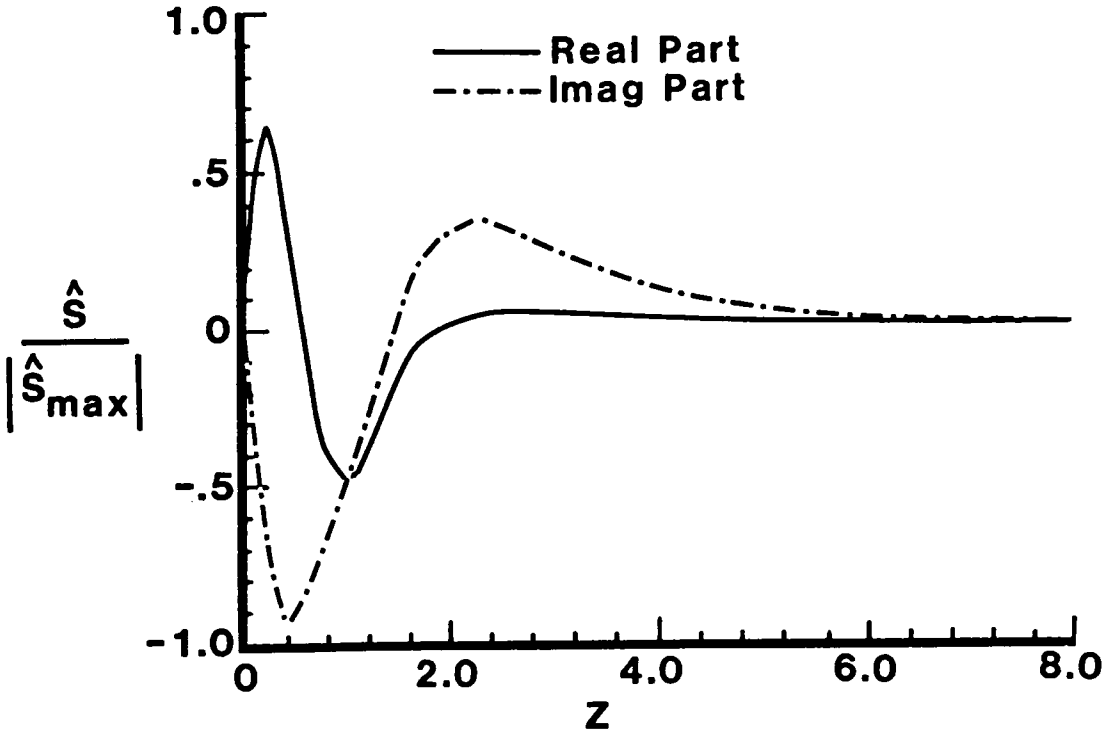

Figure 18: Normalized eigenfunction in the ξ direction for conditions of Case 5; $X/C = 0.1059$, $\hat{s}_{max} = (.045, -.073)$.

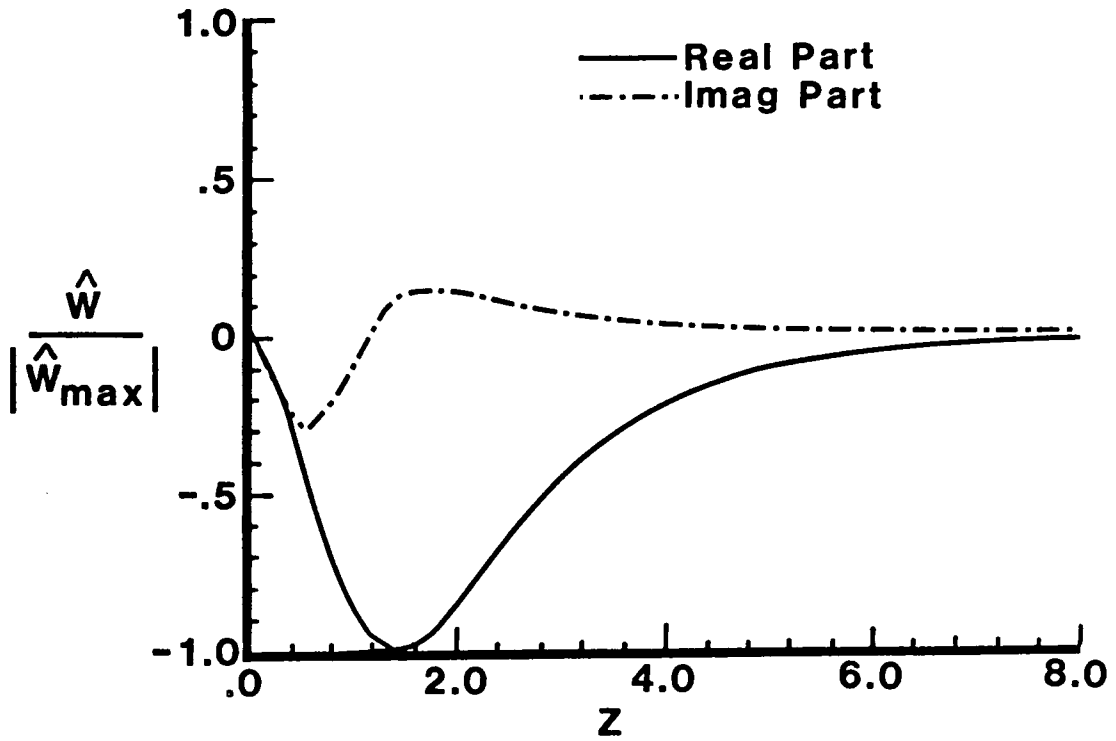

Figure 19: Normalized eigenfunction in the z direction for conditions of Case 5; $X/C = 0.1059$, $\hat{w}_{max} = (-0.049, 0.006)$.

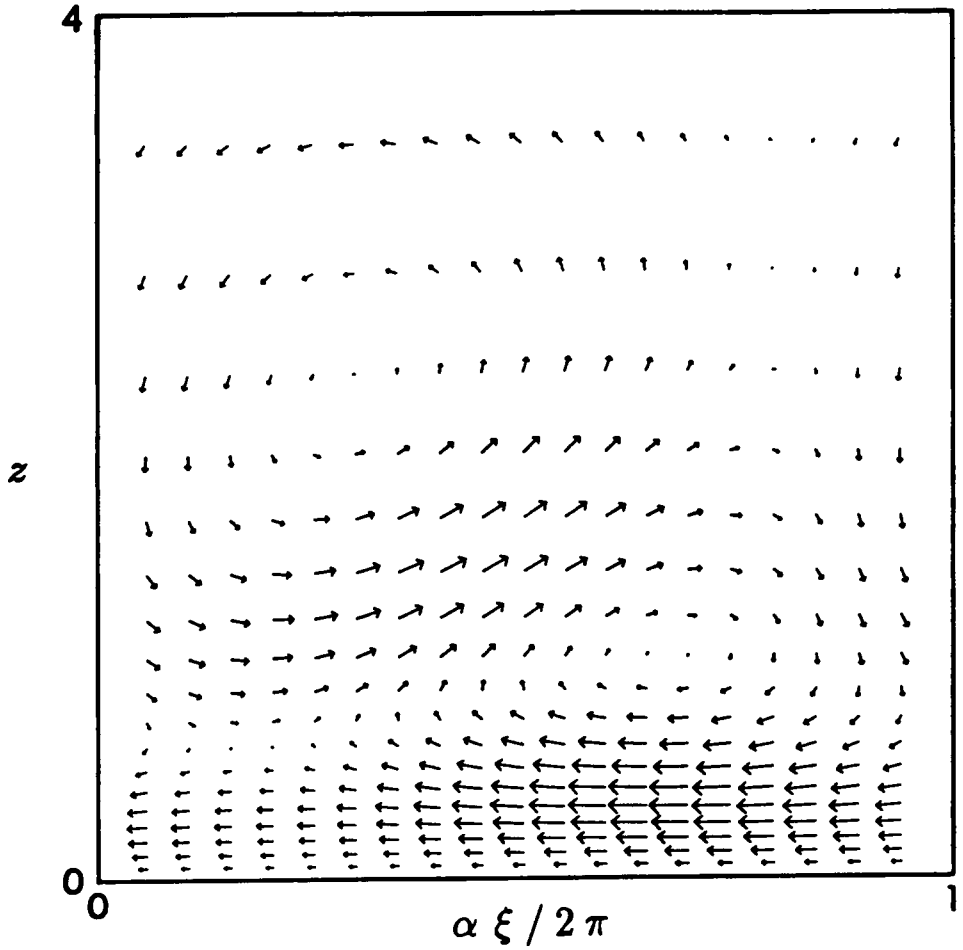

Figure 20: Velocity vector plot in the ξ, z plane for the conditions of Case 5; $X/C = 0.1330$, $\lambda_w / \delta_{0.995} = 1.480$, $R_{cf} = 35$.

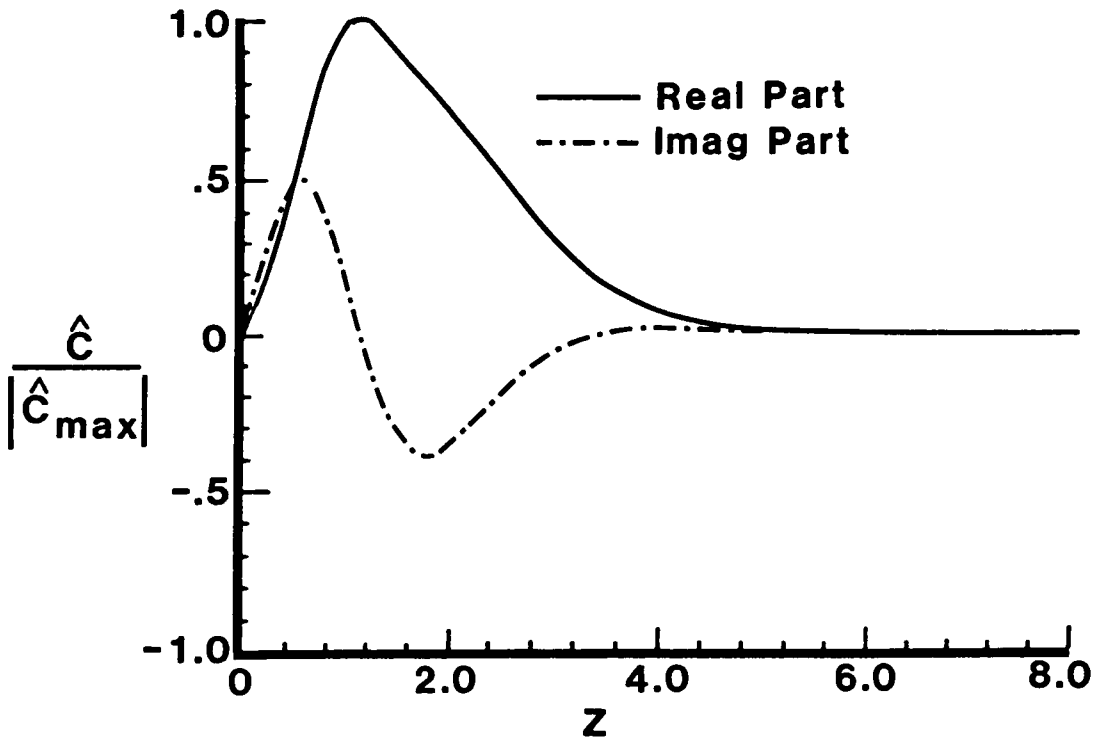

Figure 21: Normalized eigenfunction in the η direction for conditions of Case 5; $X/C = 0.1330$, $\hat{c}_{max} = (1.0, 0.0)$.

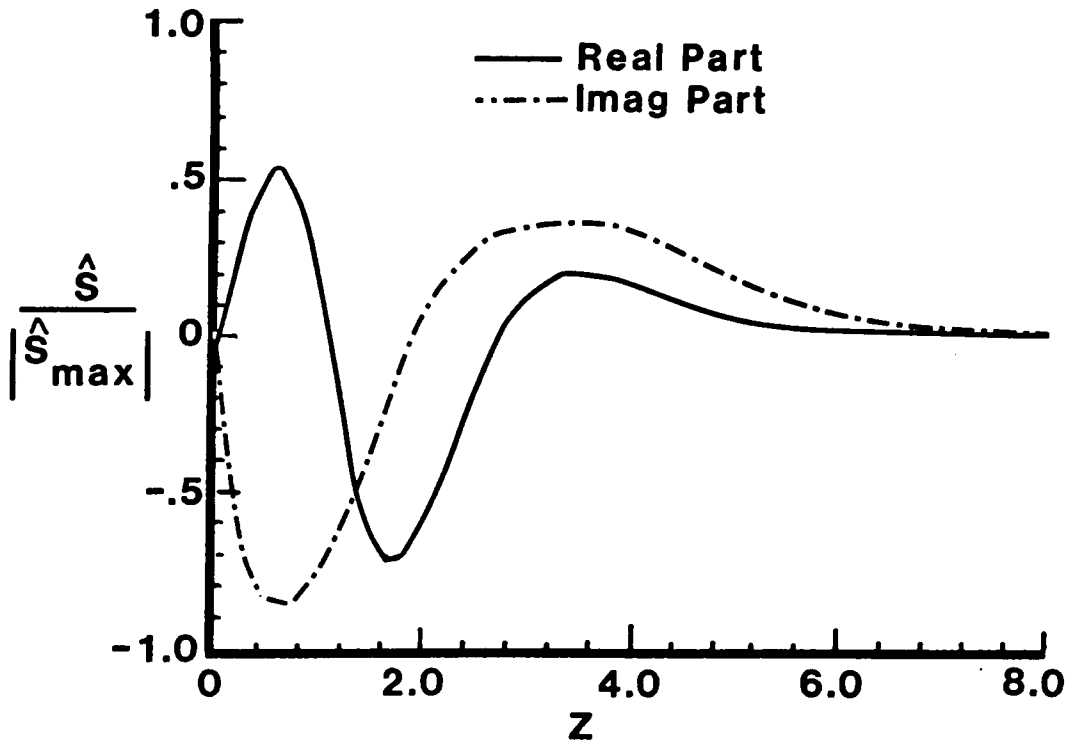

Figure 22: Normalized eigenfunction in the ξ direction for conditions of Case 5; $X/C = 0.1330$, $\hat{s}_{max} = (0.025, -.040)$.

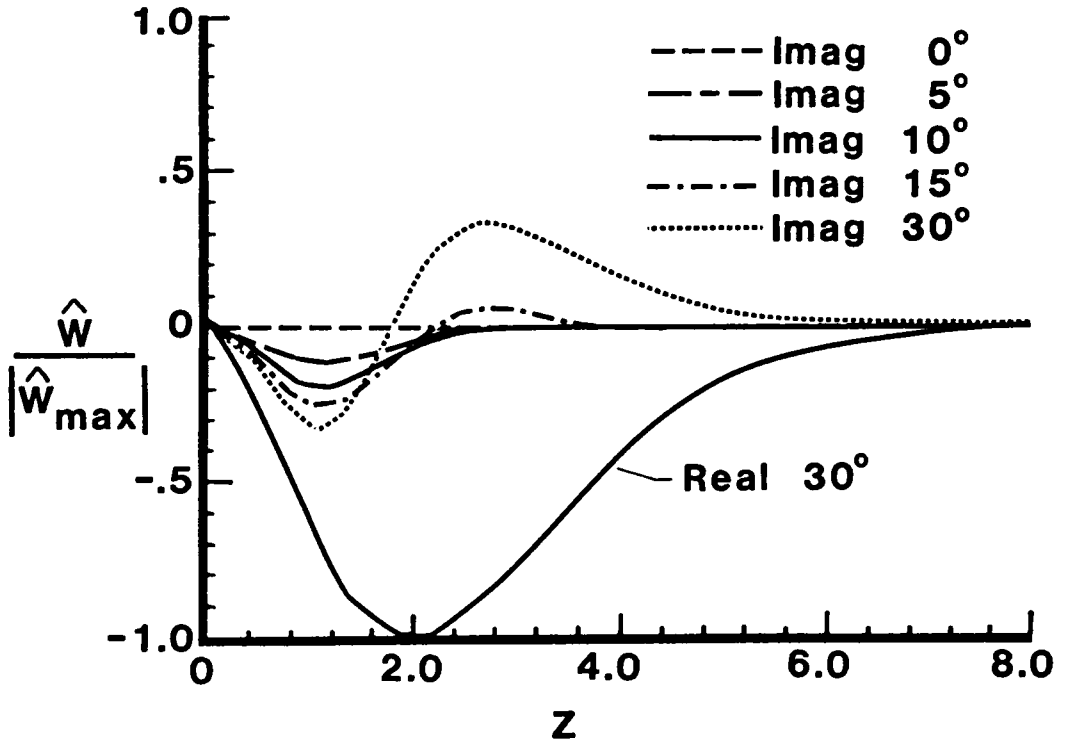

Figure 23: Normalized eigenfunction in the z direction for conditions of Case 5; $X/C = 0.1330$, $\hat{w}_{max} = (-0.049, 0.010)$: compared with Cases 1-4.

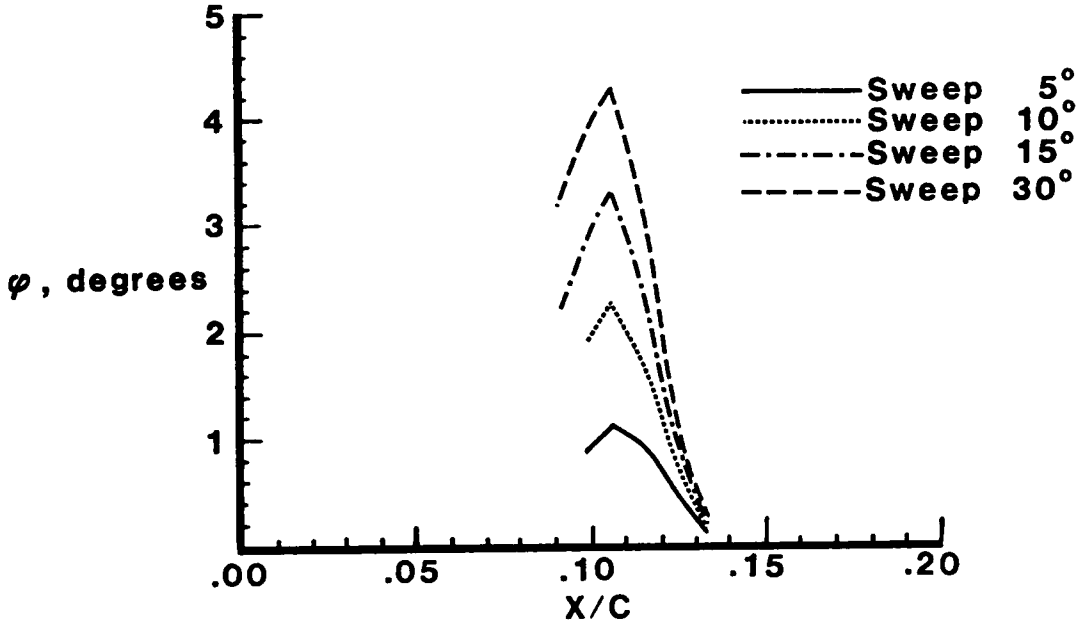

Figure 24: Wave orientation with respect to the streamline direction as a function of position for cases 2-5.

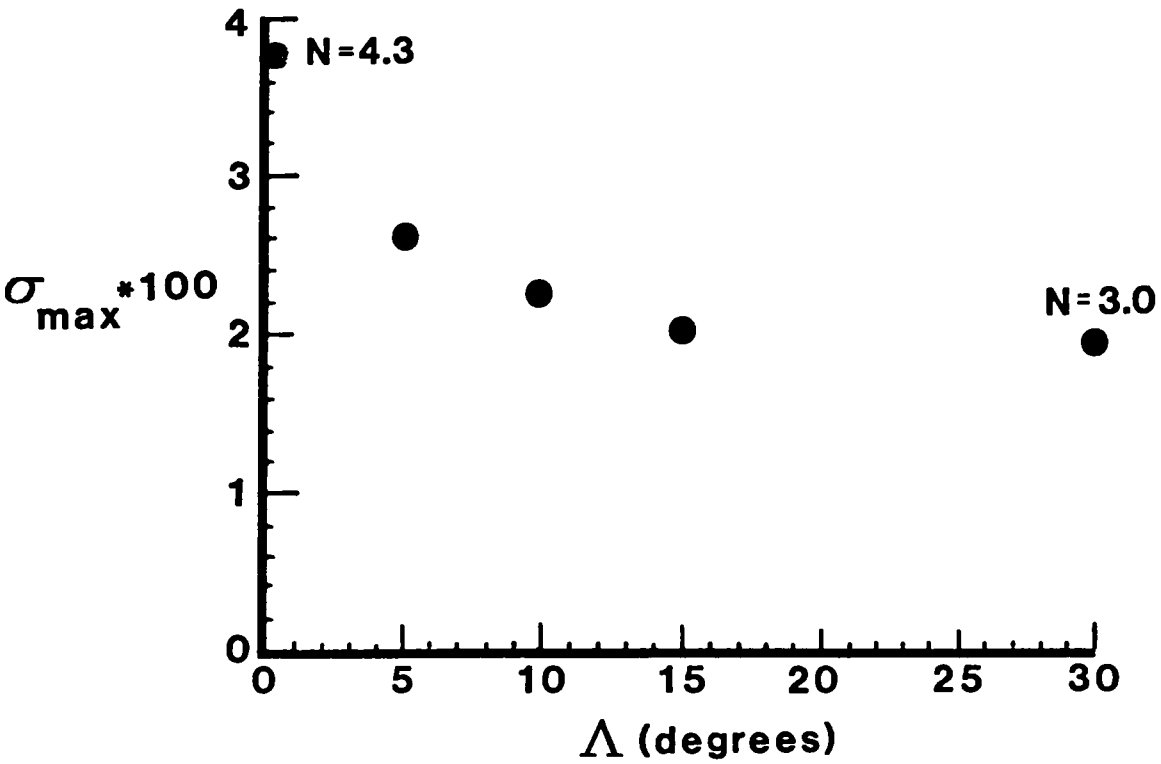

Figure 25: Maximum amplification rate as function of sweep angle for cases 1-5.

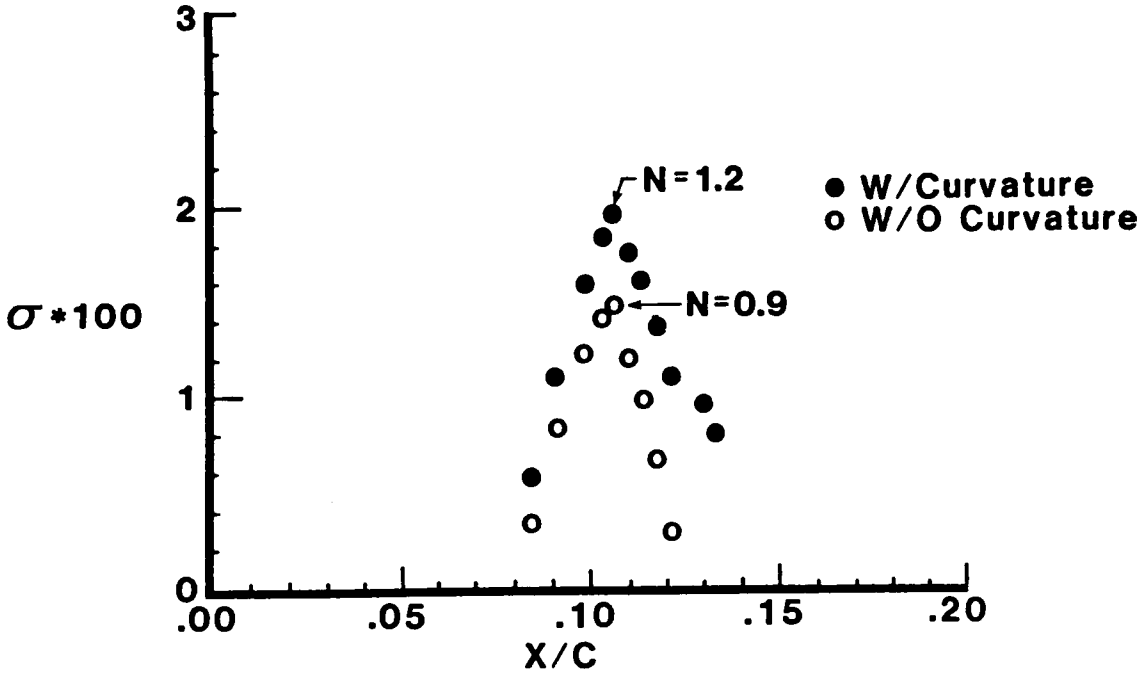

Figure 26: Amplification rate as a function of position for conditions of case 5.

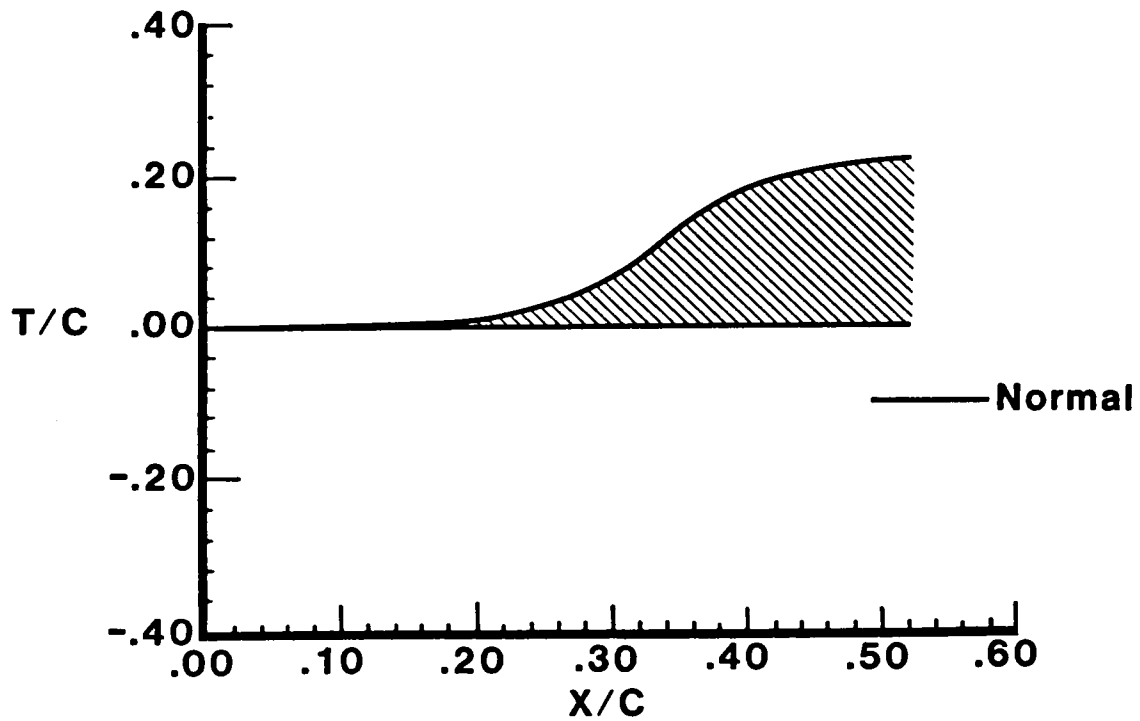

Figure 27: Surface geometry of the model of Cases 6-8 as a function of chord fraction.

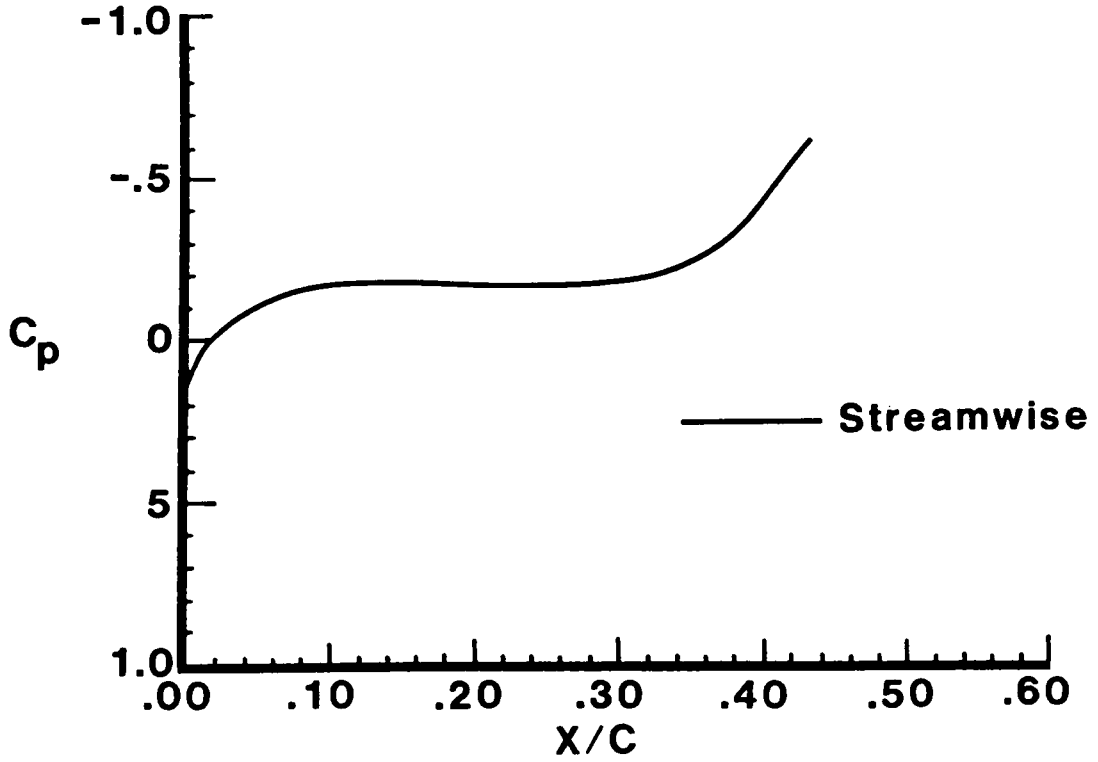

Figure 28: Experimental pressure distribution on the model of Cases 6-8.

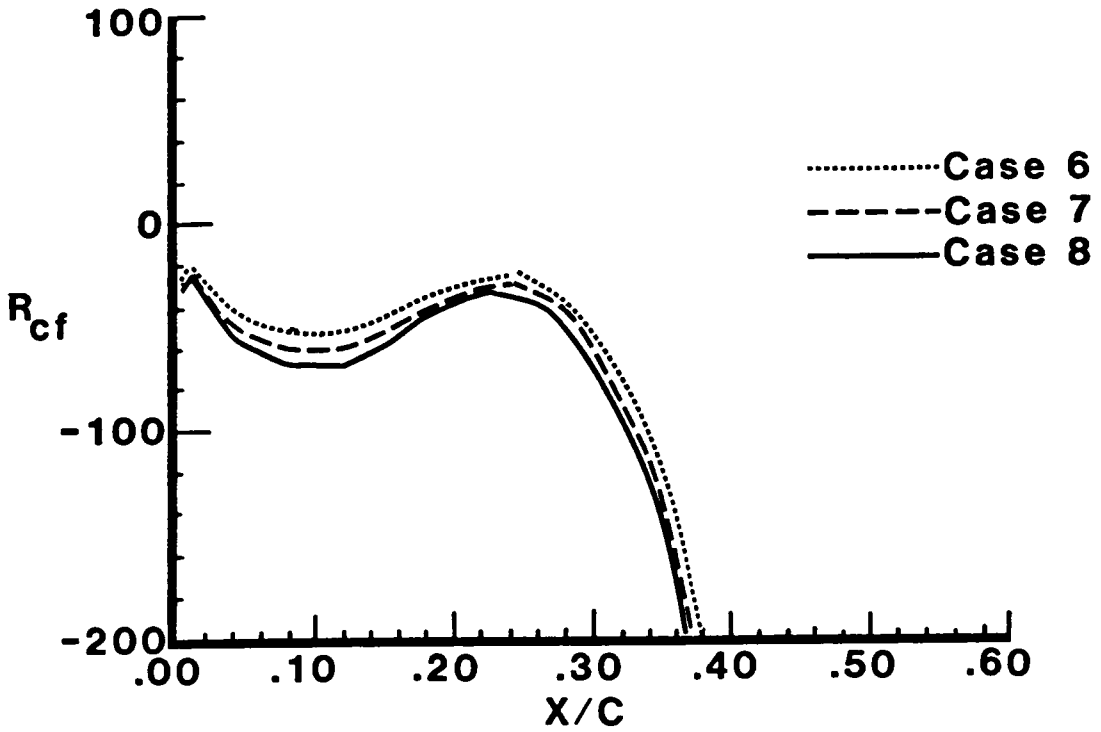

Figure 29: Crossflow Reynolds number distribution on the model of Cases 6-8.

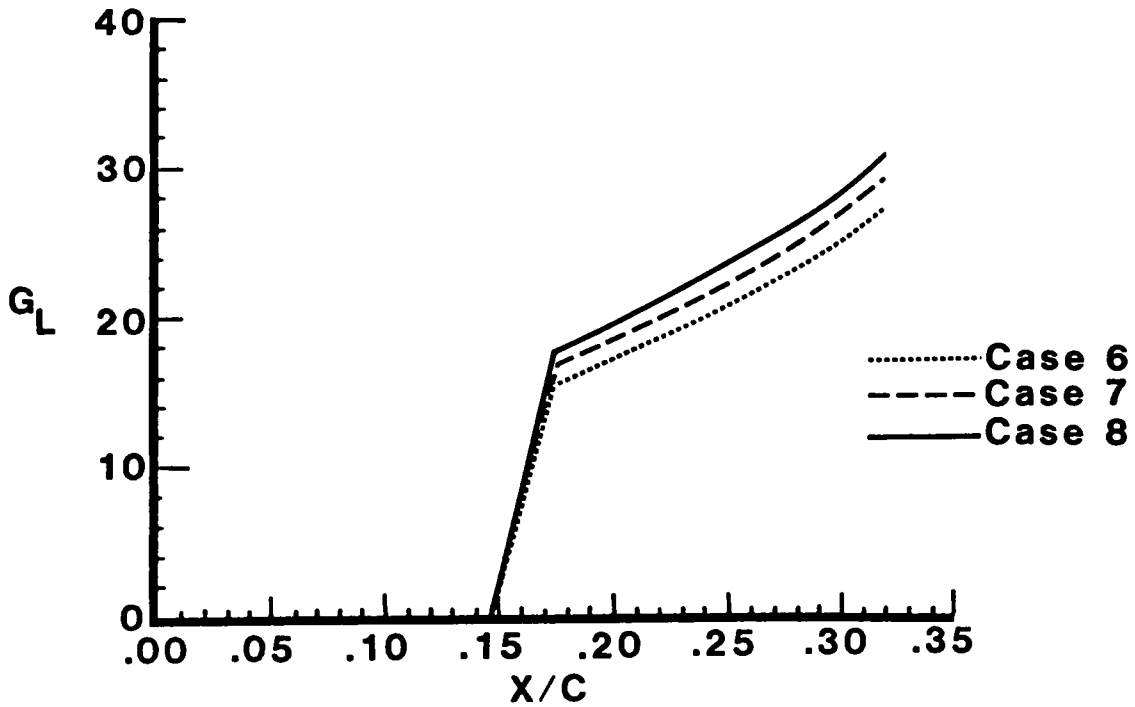

Figure 30: Görtler number distribution in the concave region for the model of Cases 6-8.

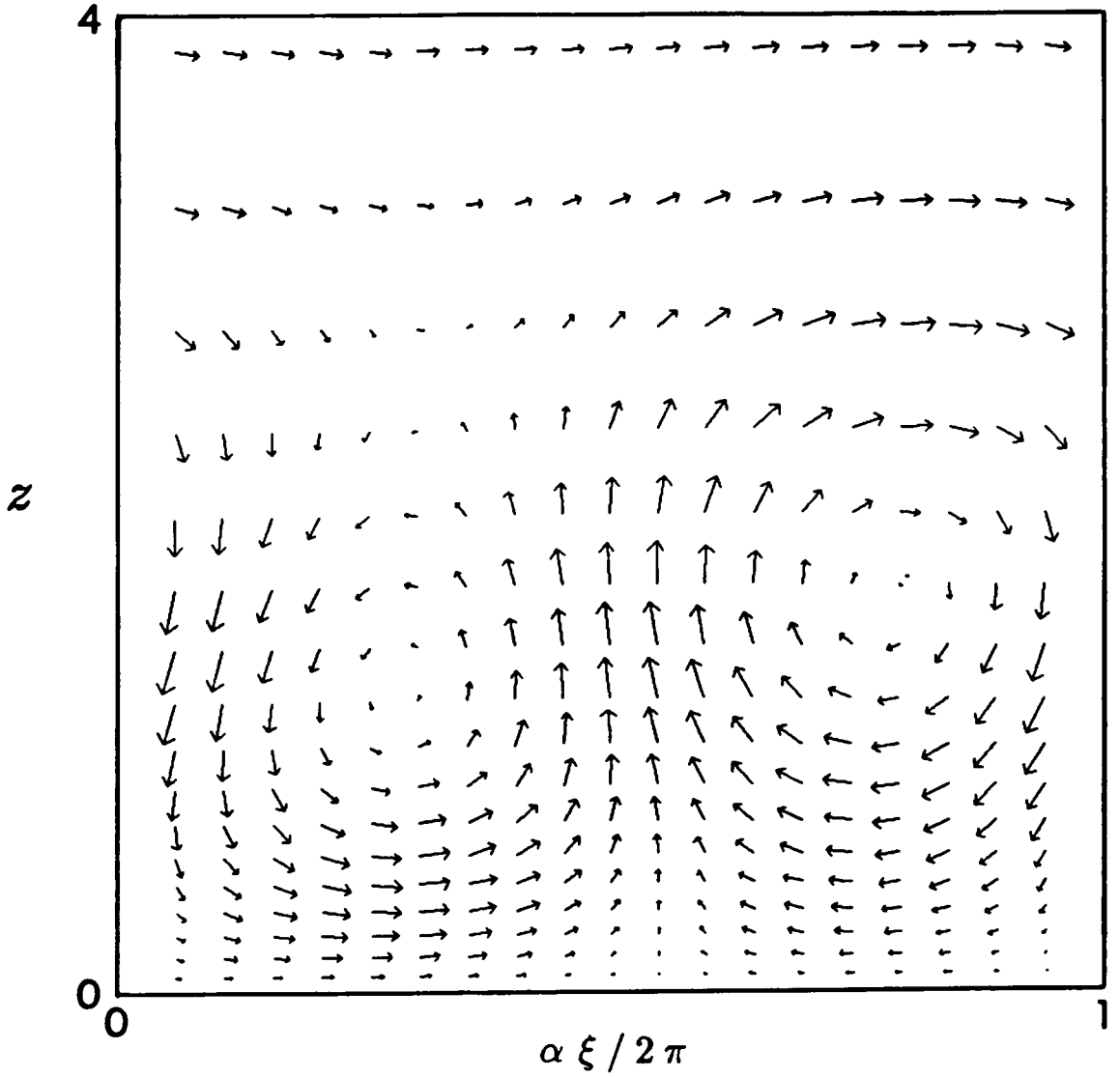

Figure 31: Velocity vector plot in the ξ, z plane for for the conditions of Case 7; $X/C = 0.1889$, $\lambda_w / \delta_{0.995} = 1.300$, $R_{cf} = 35$.

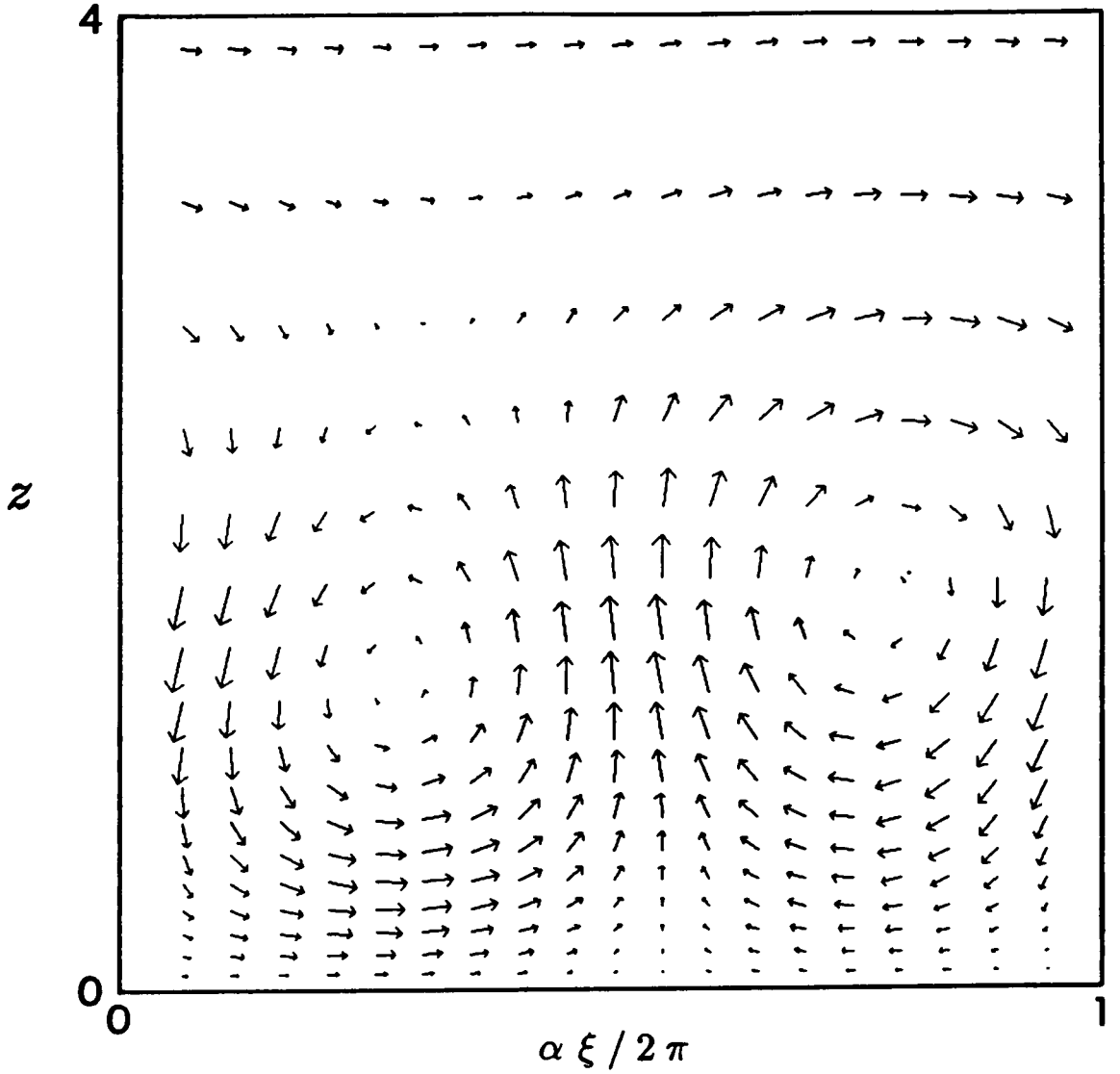

Figure 32: Velocity vector plot in the ξ, z plane for the conditions of Case 7; $X/C = 0.2034$, $\lambda_w / \delta_{0.995} = 1.234$, $R_{cf} = 32$.

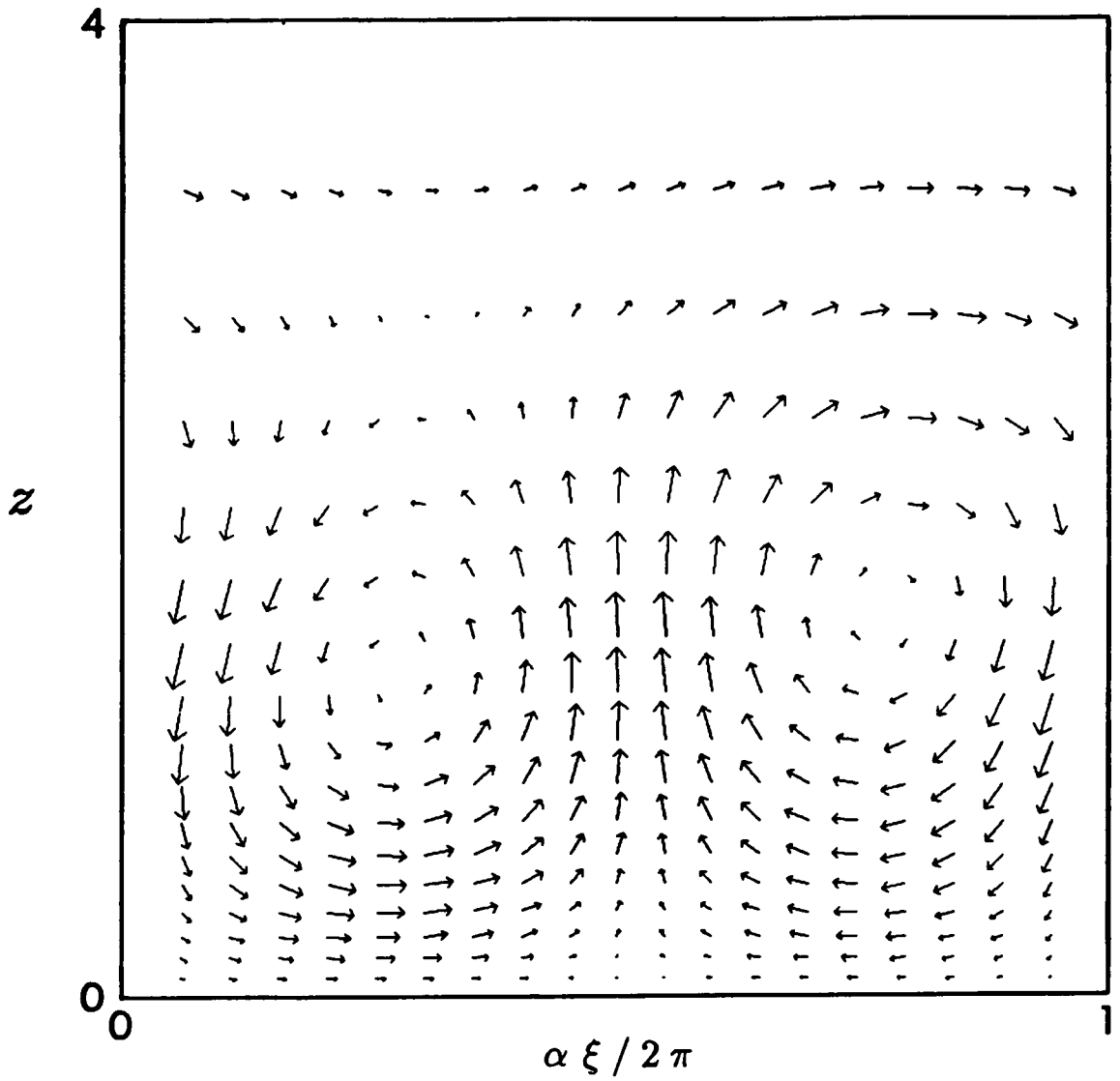

Figure 33: Velocity vector plot in the ξ, z plane for the conditions of Case 7; $X/C = 0.2180$, $\lambda_w/\delta_{0.995} = 1.198$, $R_{cf} = 28$.

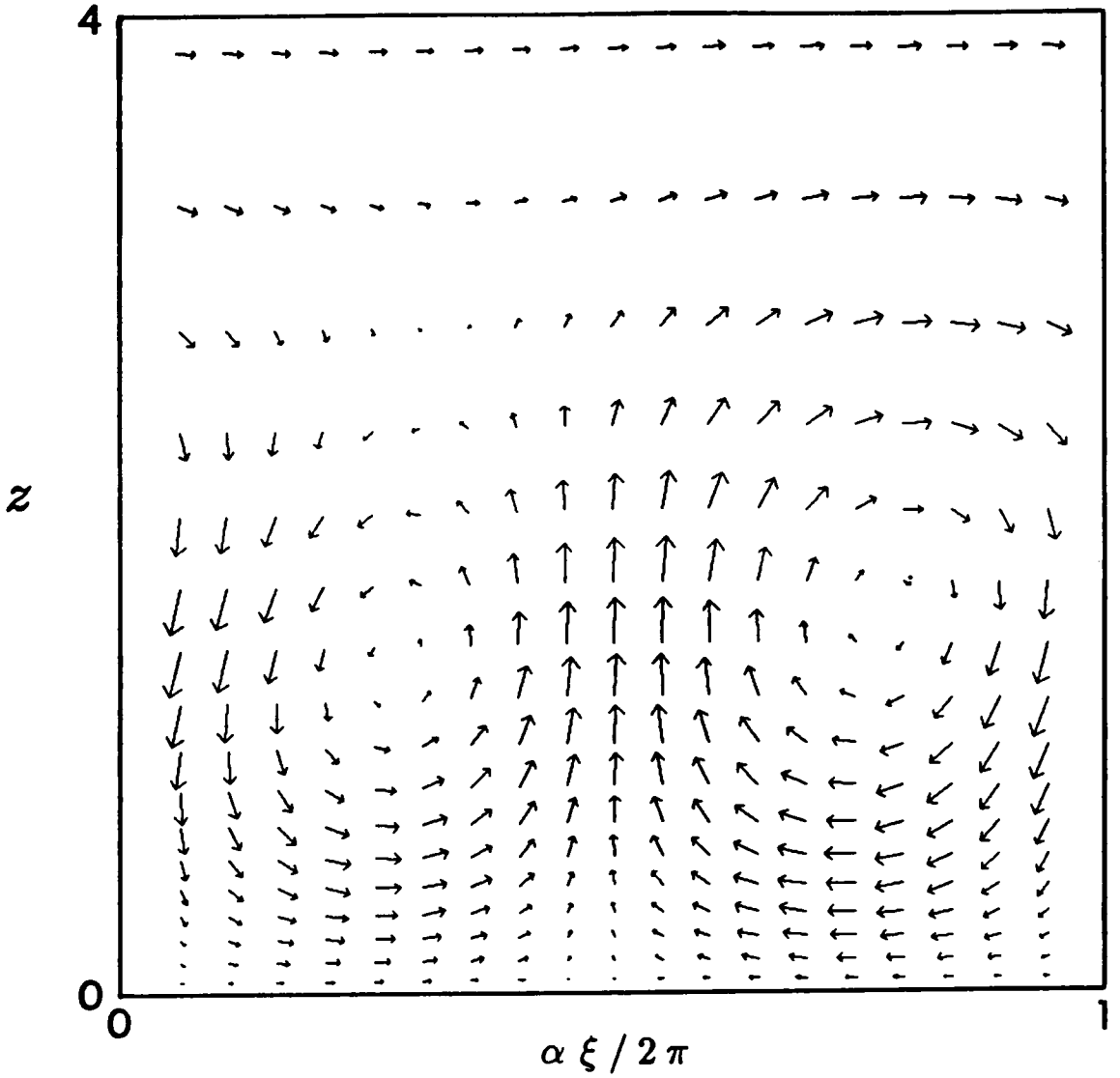

Figure 34: Velocity vector plot in the ξ, z plane for the conditions of Case 7; $X/C = 0.2325$, $\lambda_w / \delta_{0.995} = 1.202$, $R_{cf} = 28$.

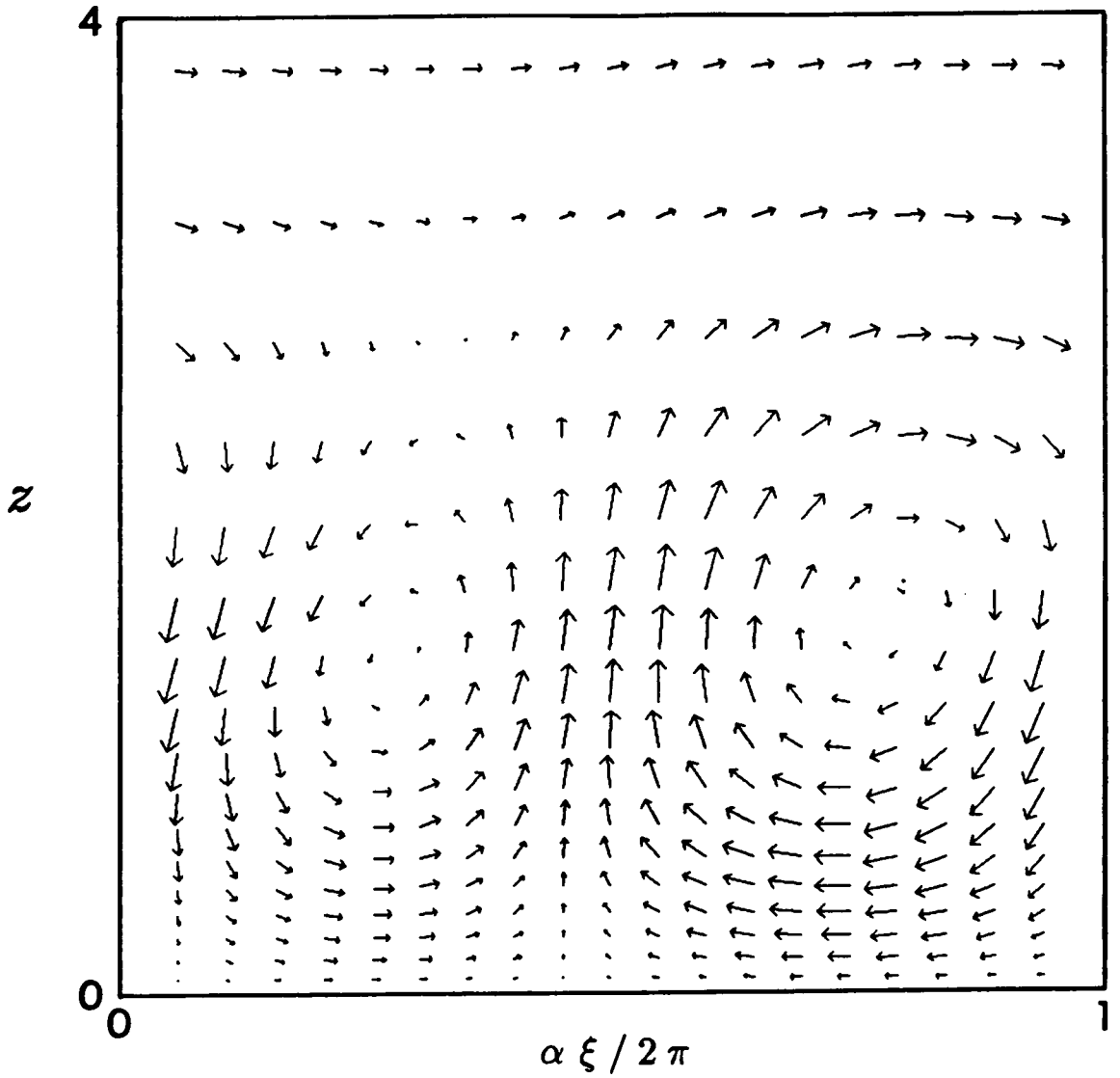

Figure 35: Velocity vector plot in the ξ, z plane for the conditons of Case 7; $X/C = 0.2470$, $\lambda_w / \delta_{0.995} = 1.232$, $R_{cf} = 29$.

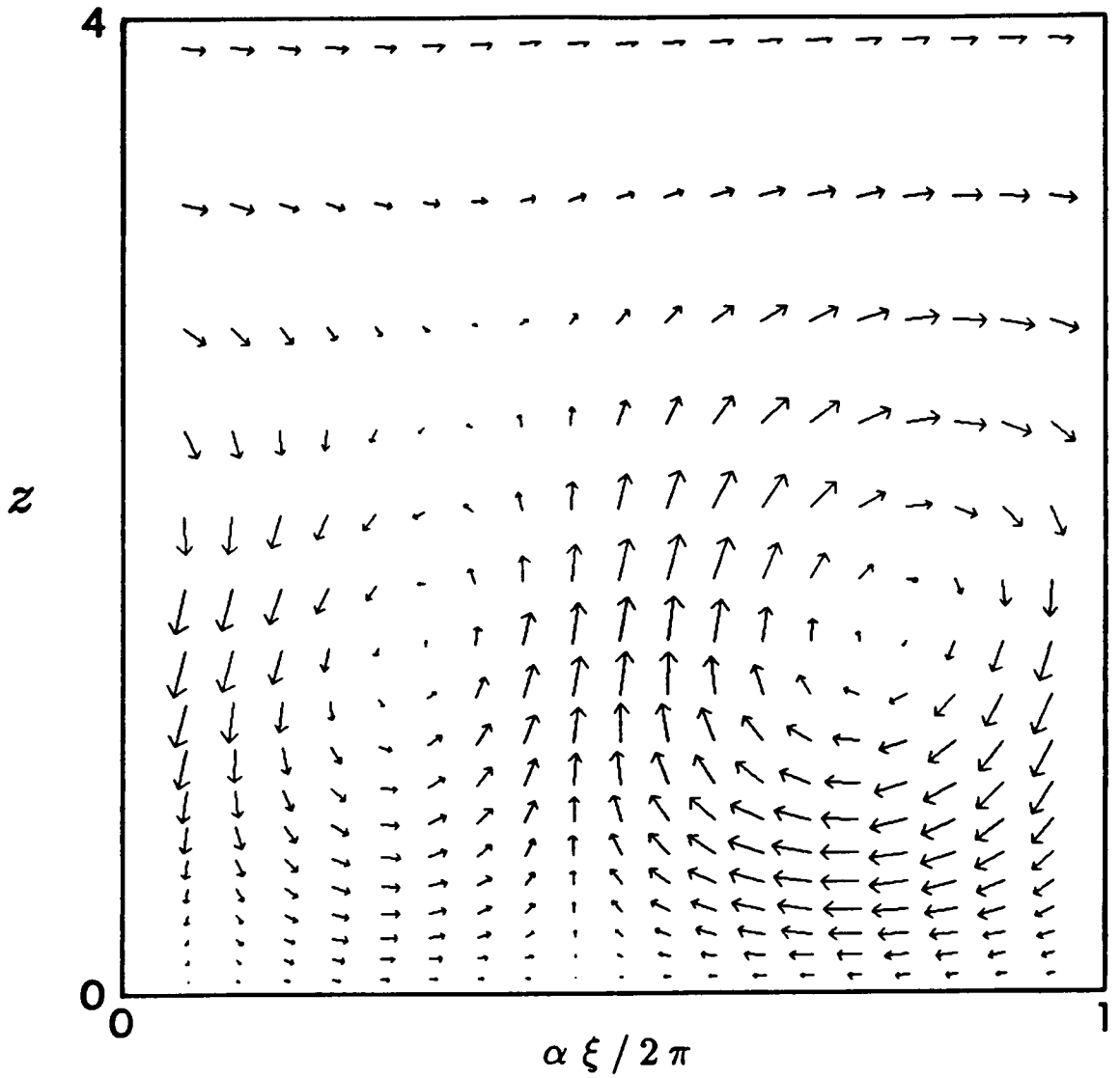

Figure 36: Velocity vector plot in the ξ, z plane for the conditions of Case 7; $X/C = 0.2615$, $\lambda_w / \delta_{0.995} = 1.275$, $R_{cf} = 31$.

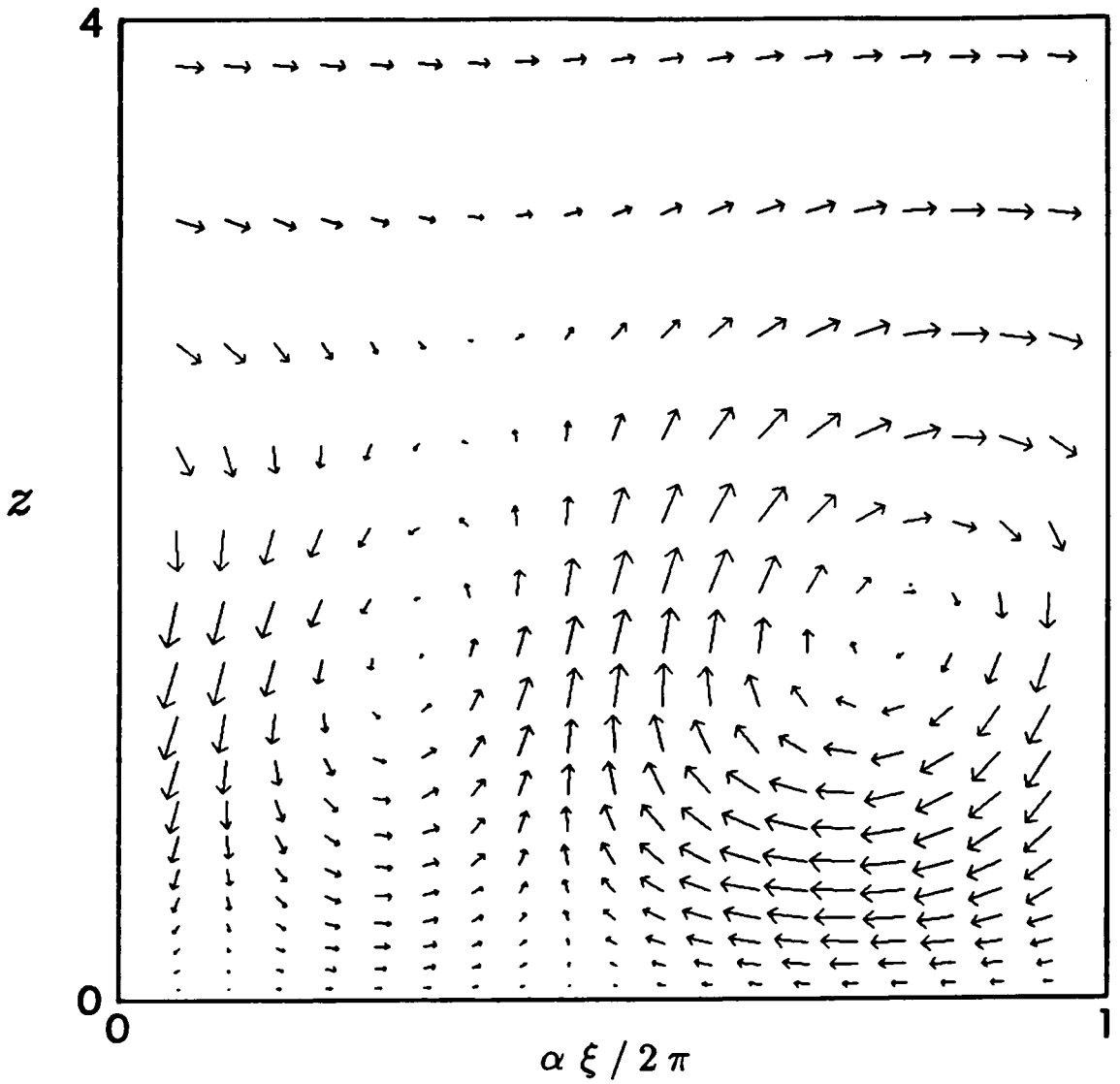

Figure 37: Velocity vector plot in the ξ, z plane for the conditons of Case 7; $X/C = 0.2761$, $\lambda_w / \delta_{0.995} = 1.345$, $R_{cf} = 37$.

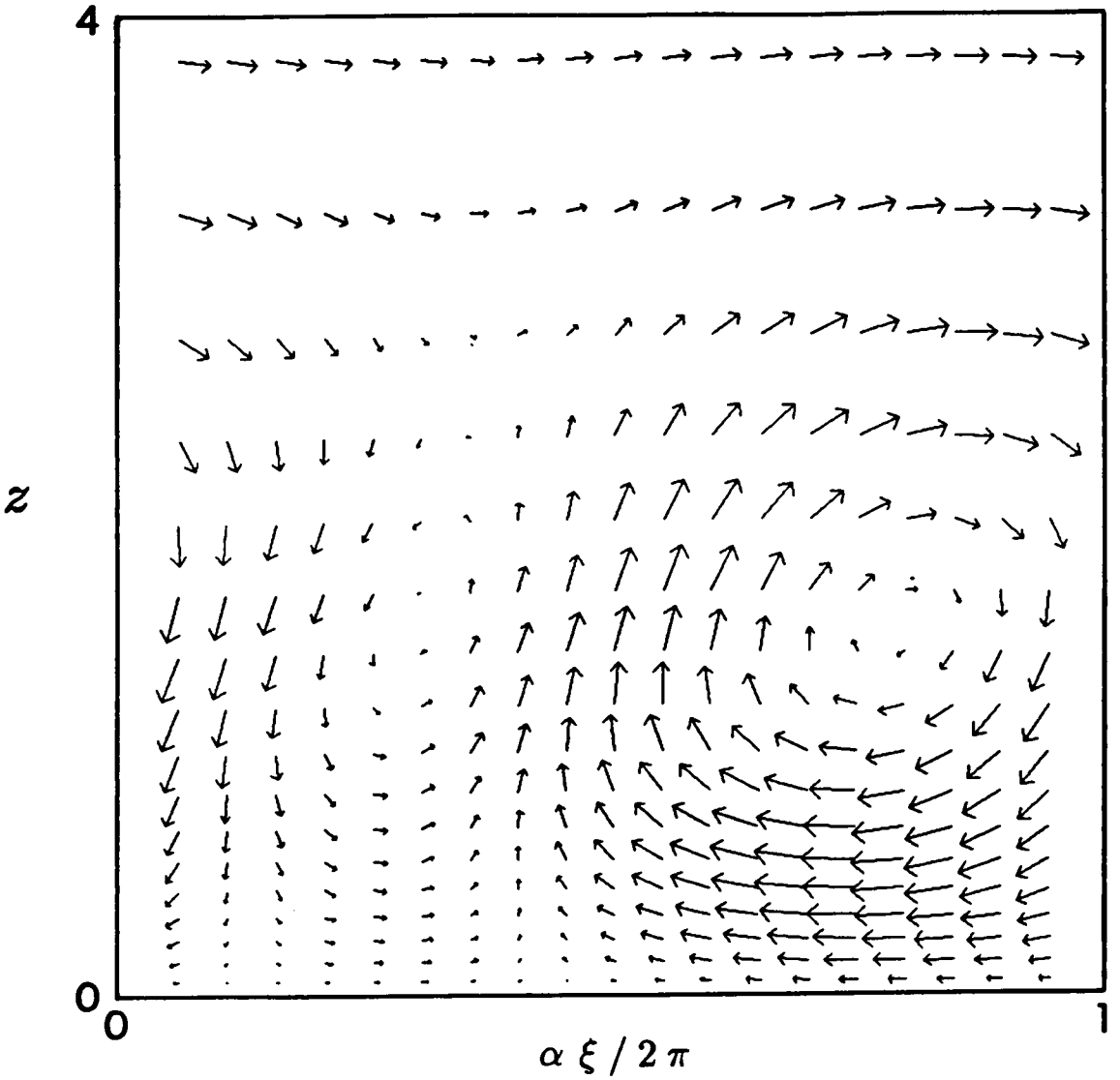

Figure 38: Velocity vector plot in the ξ, z plane for the conditions of Case 7; $X/C = 0.2906$, $\lambda_w / \delta_{0.995} = 1.484$, $R_{cf} = 48$.

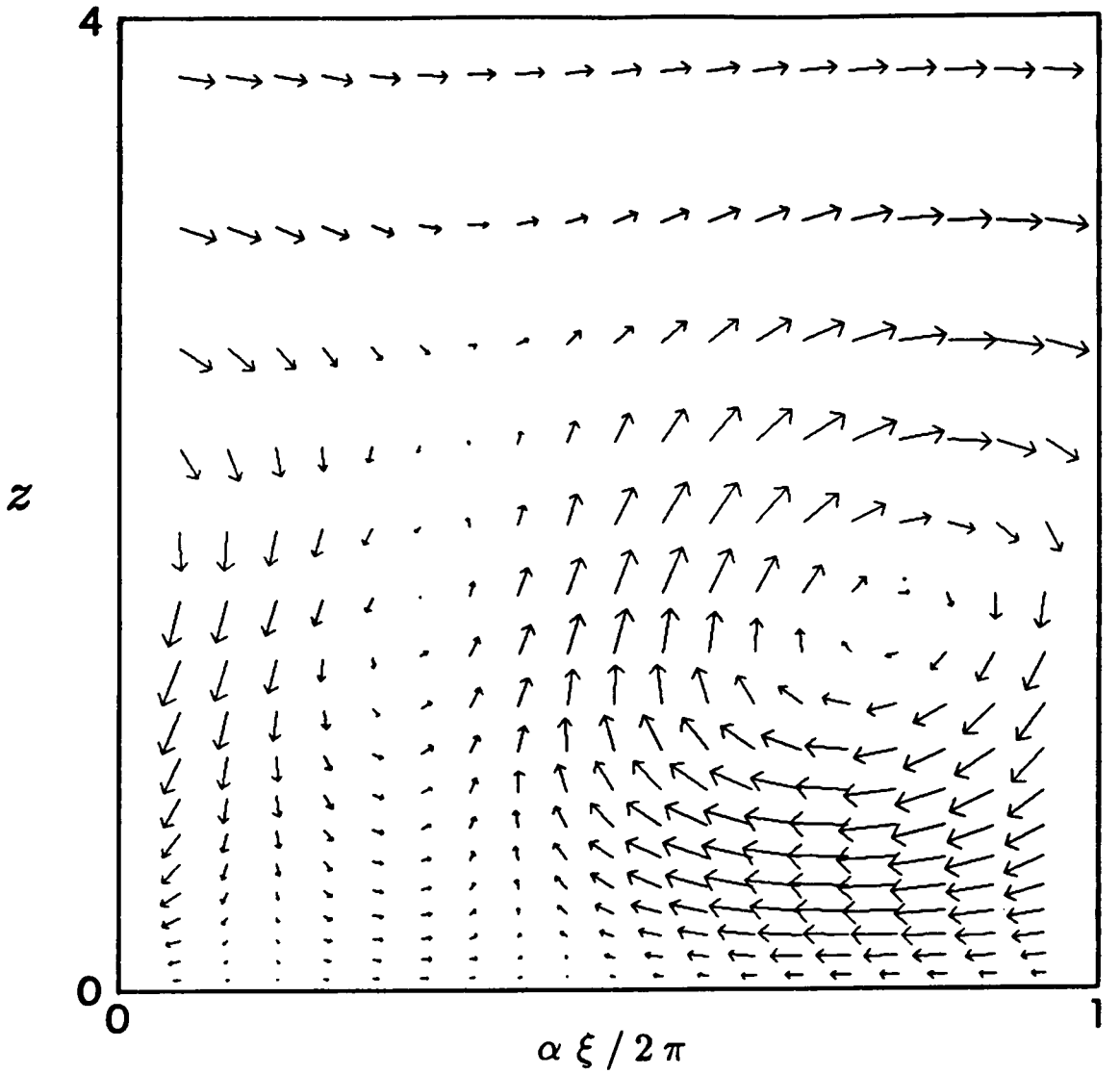

Figure 39: Velocity vector plot in the ξ, z plane for the conditions of Case 7; $X/C = 0.3051$, $\lambda_w / \delta_{0.995} = 1.598$, $R_{cf} = 62$.

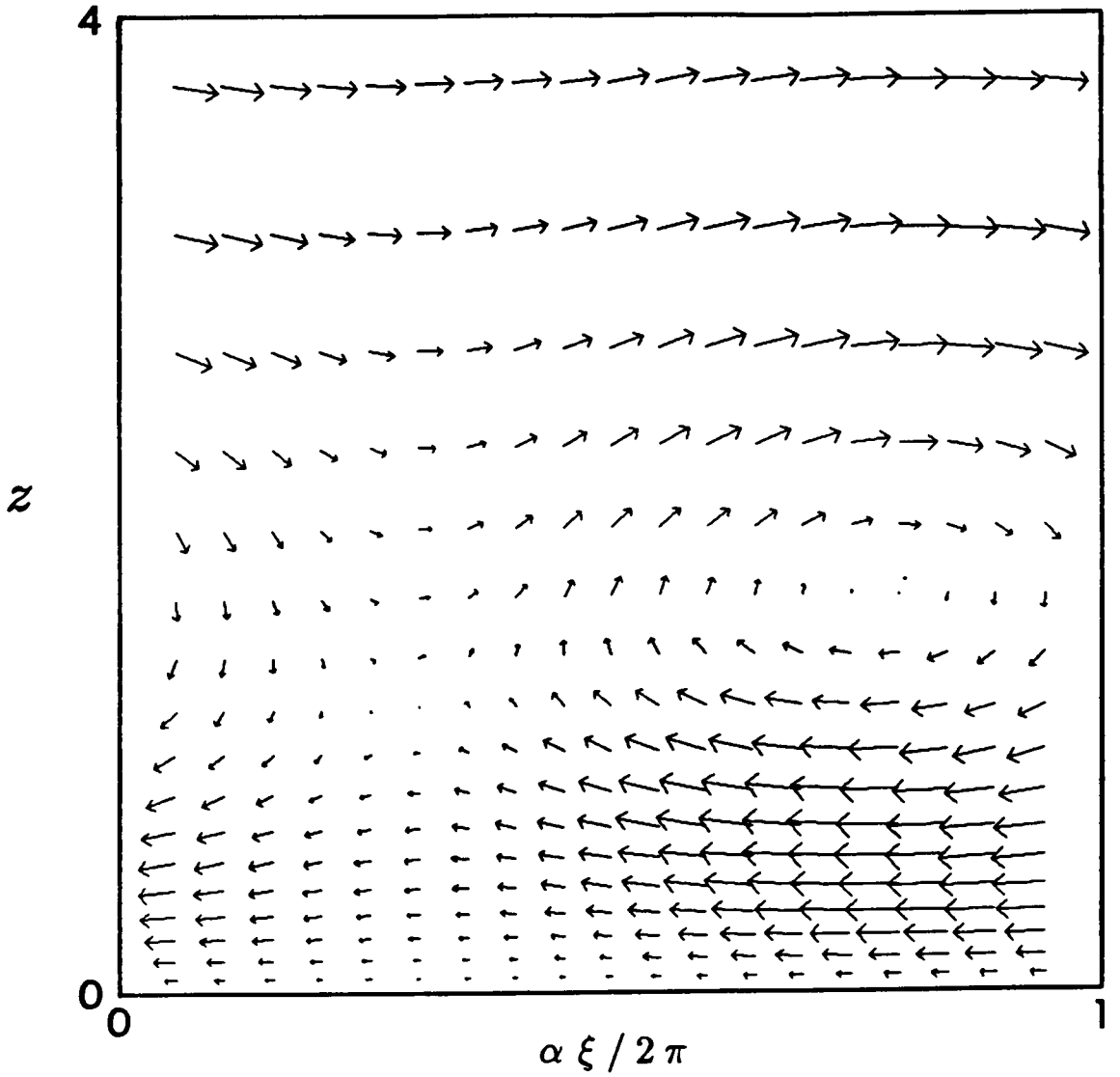

Figure 40: Velocity vector plot in the ξ, z plane for the conditions of Case 7; $X/C = 0.3342$, $\lambda_w / \delta_{0.995} = 2.830$, $R_{cf} = 94$.

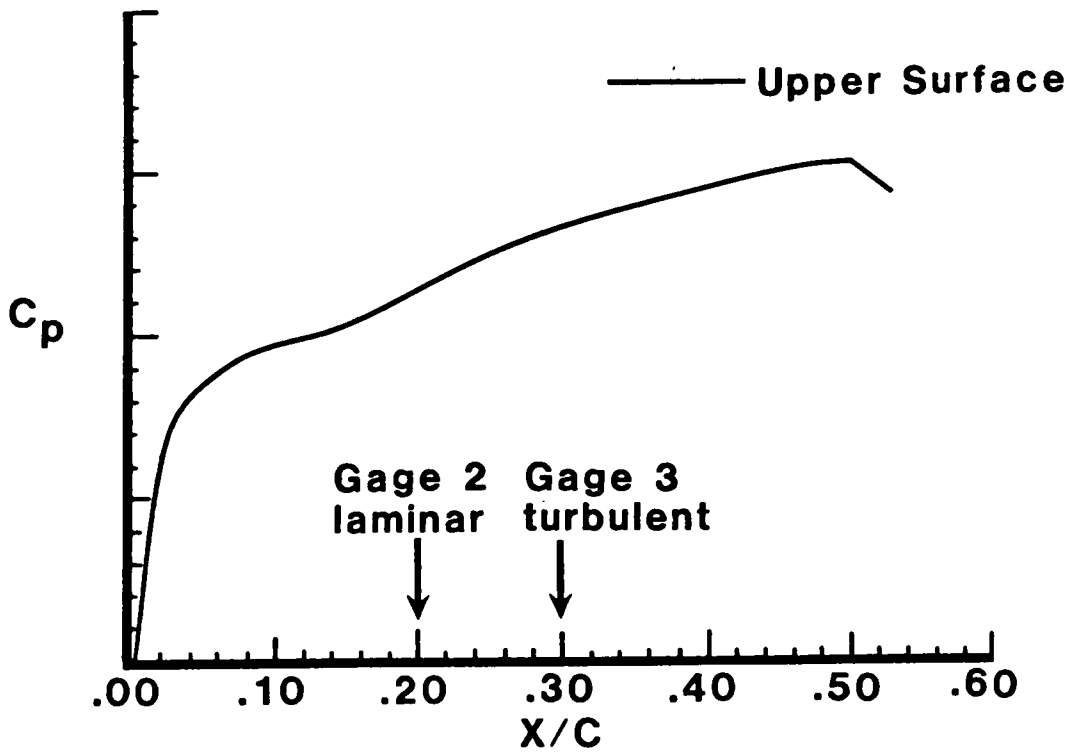

Figure 41: Pressure coefficient distribution for Case 9.

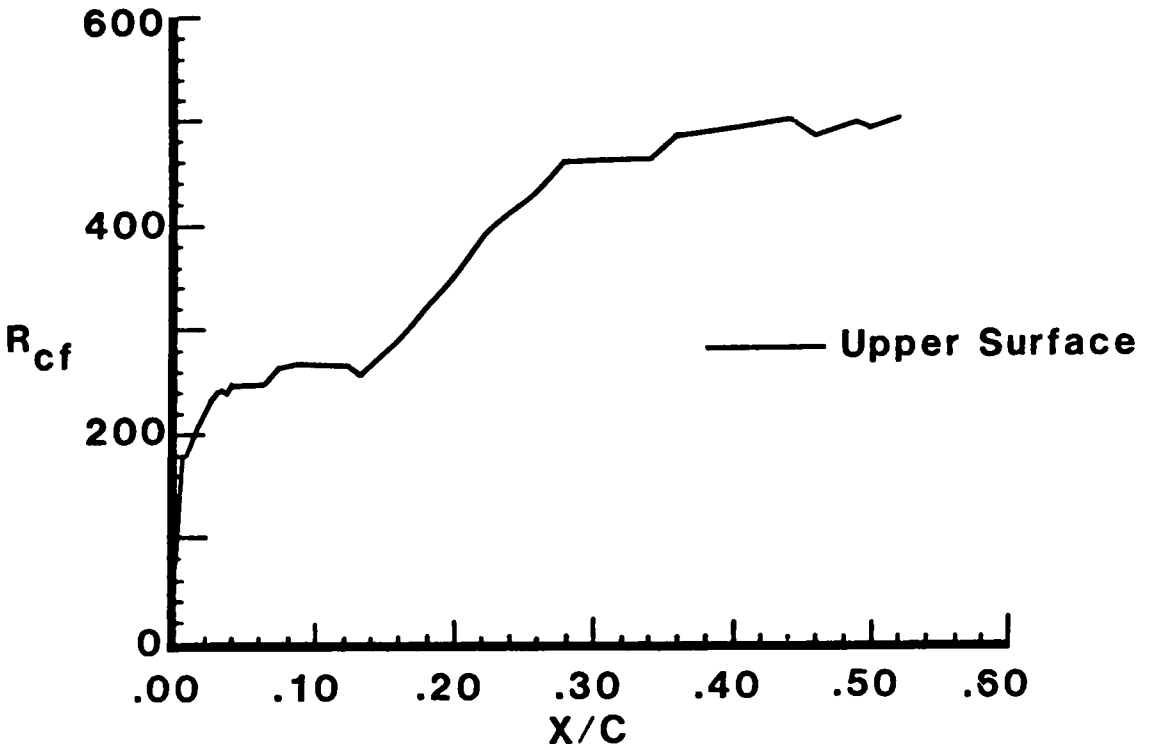

Figure 42: Crossflow Reynolds number distribution for Case 9.

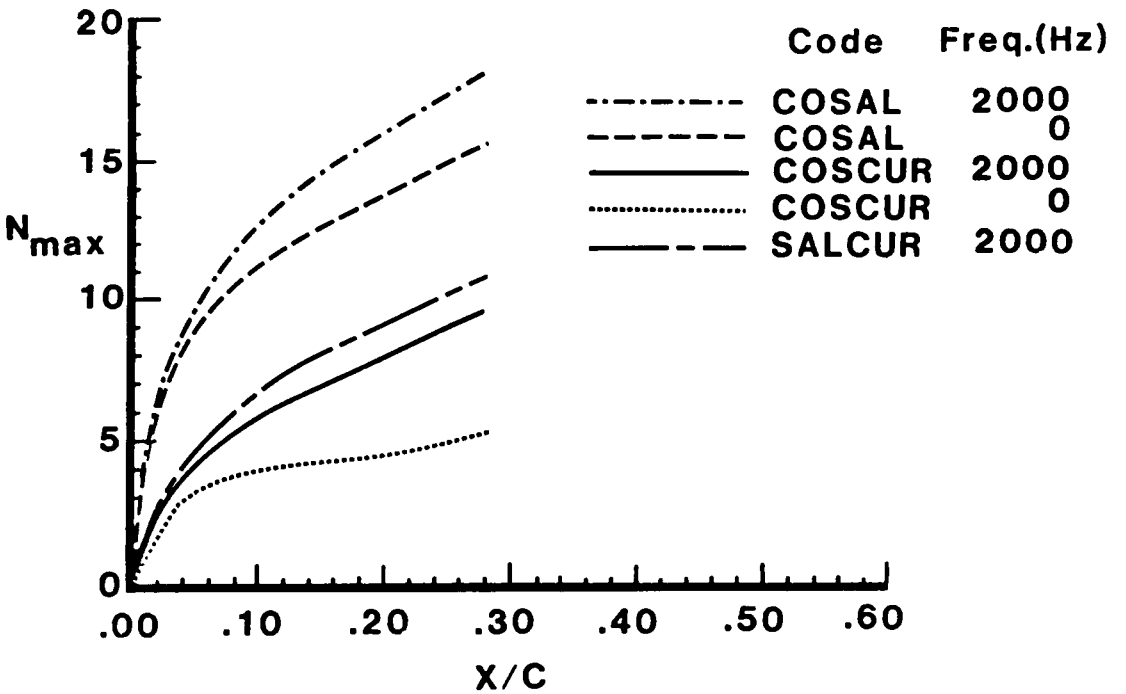

Figure 43: N-factor calculations for Case 9.

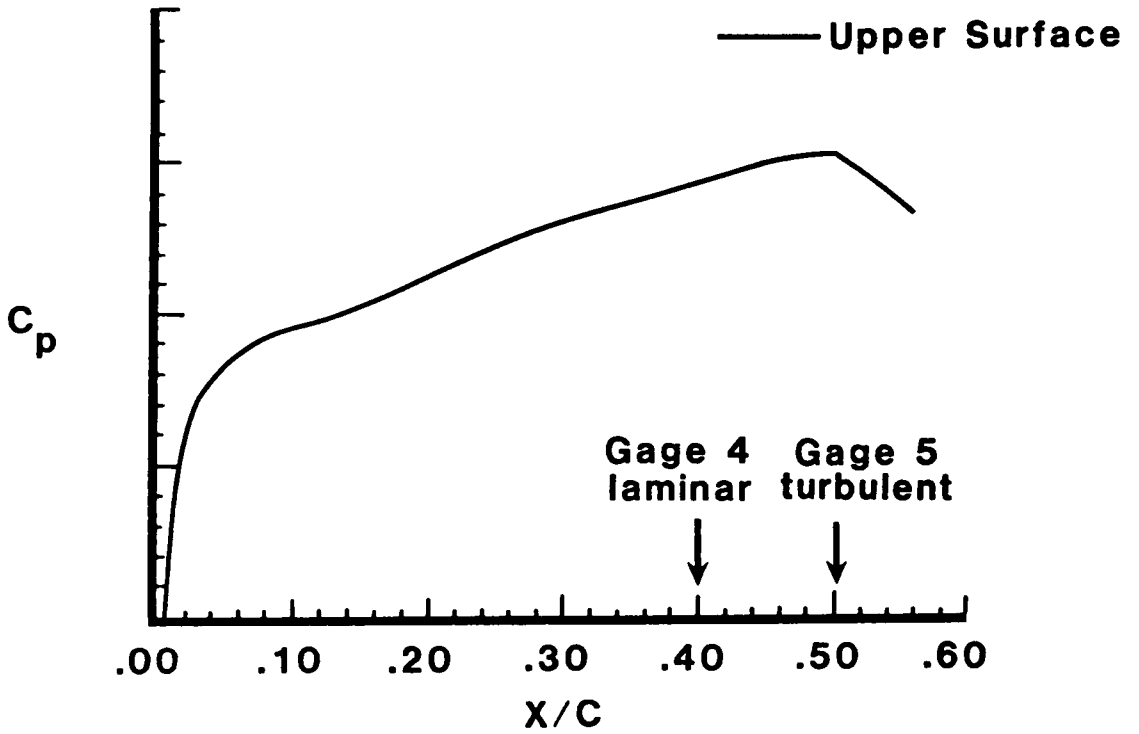

Figure 44: Pressure coefficient distribution for Case 10.

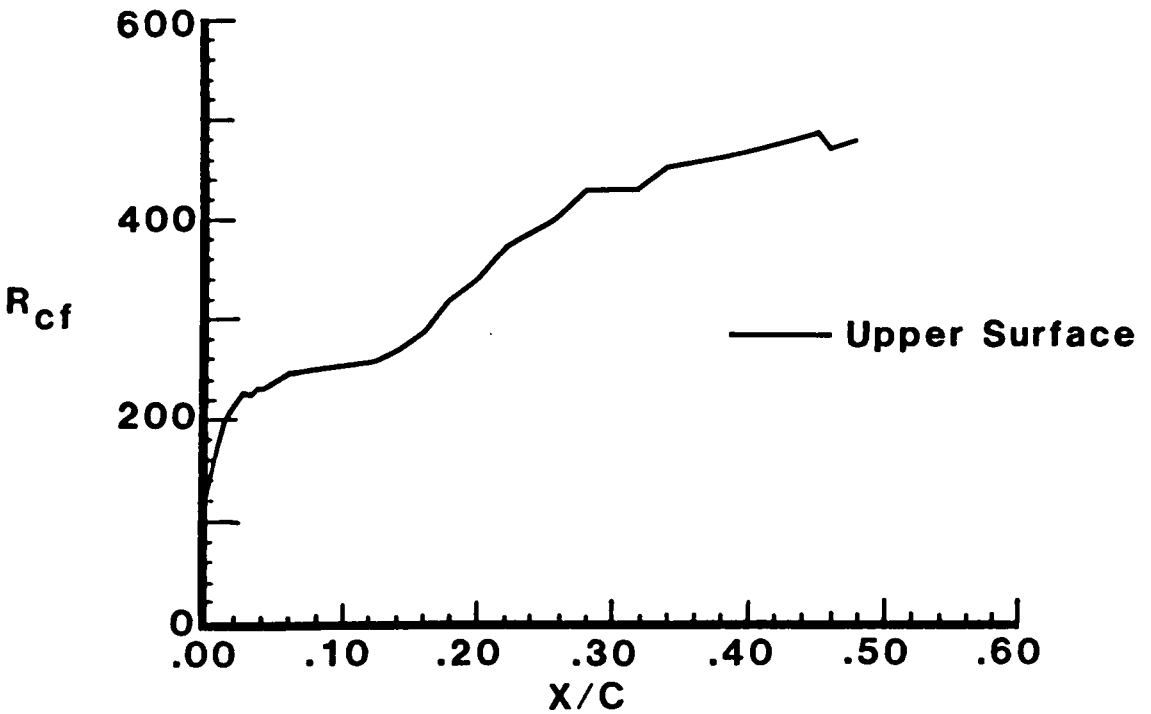

Figure 45: Crossflow Reynolds number distribution for Case 10.

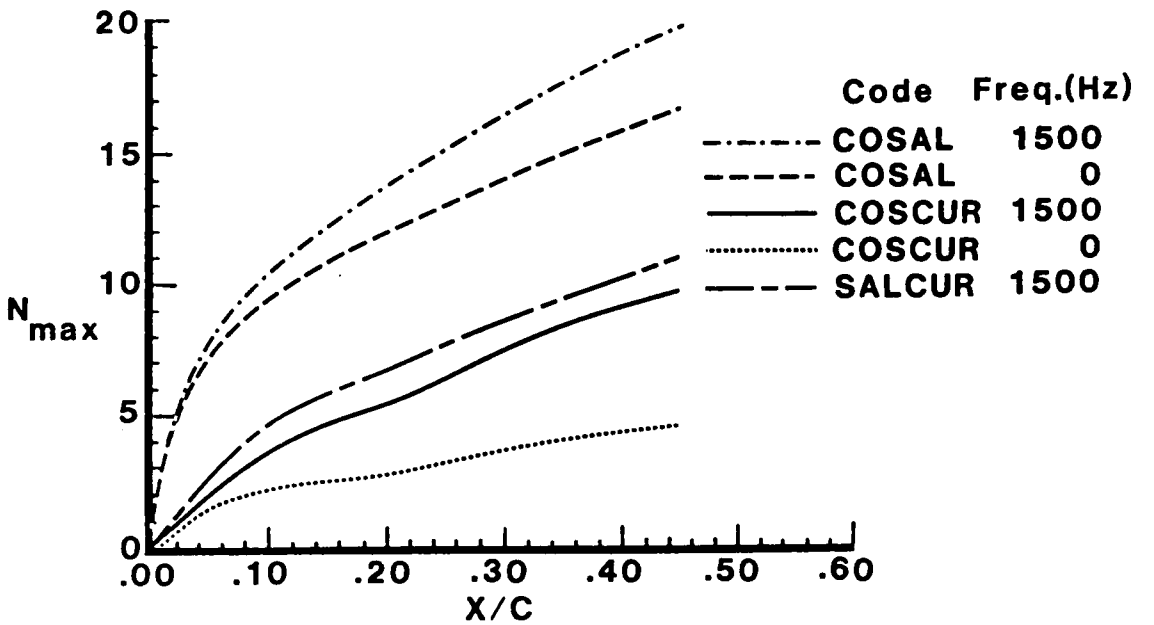

Figure 46: N-factor calculations for Case 10.

The vita has been removed from the scanned document